UNIVERSITÀ DEGLI STUDI DI PADOVA

Dipartimento di Ingegneria Industriale DII

Laurea Magistrale in Ingegneria Energetica

MELTING OF PARAFFIN: EXPERIMENTAL TESTS AND NUMERICAL ANALYSIS

Relatore: Prof. Luisa Rossetto

Correlatore: Prof. Andrea Diani

Laureando: Andrea Mameli 2018740

Anno Accademico 2021/2022

To my grandma Luigina

Summary

The materials considered in this analysis are the PCMs (Phase Change Materials). Their great advantage is the possibility to store thermal energy, thank to their high latent heat, related to the phase change itself, in particular the passage from solid to liquid phase. In particular, the selected PCMs are different paraffin, having distinct melting temperatures. The advantages of using them are first of all economical since they are cheap materials, secondly, they are not harmful to the human health. Furthermore, other advantages are related to their availability at different melting temperatures, their very poor aggressiveness when in contact with other materials, and finally, their low volume variation during the phase change, which allows them to use, as in the case study, a reduced dimensions apparatus (convenient also from the economical point of view). The possibility to store energy presents applications in the renewable energy sources field, thinking about their discontinuity and the unpredictability. However, it is important to know how the applications are many and not limited just to this field. The main problem of PCMs is related to the low thermal conductivity, as it will be reported later during the analysis, around 0.2 W m^{-1} K^{-1}. For this reason, the principle applied is to support the enhanced heat transfer with a metallic matrix, with specifications shown later, in order to improve the overall process (the geometry taken into account is the elementary cell 10 mm, porosity 93%, repeated to form the component). The used paraffin have melting temperatures of 42, 55, and 64 °C. The experiments conducted in the laboratory guarantee the fairness of the simulations, using the software Ansys, in particular the Fluent component, reproducing the original geometry (simplified in one cell). In addition, starting from the work of Diani and Campanale [1], an improved empirical model was developed, including all the geometries analyzed in past studies, in order to have an overall formulation being able to describe the complex behaviour of the systems.

The first chapter presents the description of the PCMs (types, characteristics, and applications), including also the actions taken in order to improve the thermal conductivity.
The second chapter shows the description of the system for the experiments, including the part related to the thermocouples used.

The third chapter develops the results of the analysis, with different comparisons between different properties.

The fourth chapter is related to the ANSYS Fluent simulations.

The fifth and final chapters present the explanation of the starting empirical model, the improved one, and finally the updated results from the last one, and the conclusions on the PCMs.

Riassunto esteso

I materiali considerati in questa analisi sono i PCMs (Phase Change Materials). Il loro grande vantaggio è la possibilità di immagazzinare energia termica, grazie al loro elevato calore latente, legato al cambiamento di fase stesso, in particolare al passaggio dalla fase solida a quella liquida. In particolare, i PCMs selezionati sono paraffina diverse, con temperature di fusione distinte. I vantaggi nel loro utilizzo sono prima di tutto economici poiché sono materiali poco costosi, in secondo luogo, non sono dannosi per la salute umana. Inoltre, altri vantaggi sono legati alla loro disponibilità a diverse temperature di fusione, alla loro scarsa aggressività a contatto con altri materiali ed, infine, alla loro contenuta variazione di volume durante il cambio di fase, che consente loro di utilizzare, come nel caso studiato, attrezzatura di dimensioni ridotte (conveniente anche dal punto di vista economico). La possibilità di immagazzinare energia ha visto applicazioni nel campo delle fonti energetiche rinnovabili, legate alla loro discontinuità ed imprevedibilità.
Tuttavia, è importante far presente come questa tecnologia non sia limitata solo a questo campo. Il problema principale dei PCM è legato alla bassa conducibilità termica, come verrà riportato in seguito, intorno ai 0.2 W m^{-1} K^{-1}. Per questo motivo, il principio applicato è quello di supportare il trasferimento di calore con una matrice metallica al fine di migliorare il processo complessivo (la geometria presa in considerazione è la cella elementare 10 mm, porosità 93%, ripetuta per formare il componente). Le paraffine utilizzate presentano una temperatura di fusione di 42, 55 e 64 °C. La correttezza delle simulazioni svolte grazie al software ANSYS, in particolare il componente Fluent, riproducendo la geometria originale (semplificata in una cella) è stata poi controllata utilizzando gli esperimenti condotti in laboratorio. Inoltre, a partire dal lavoro di Diani e Campanale [1], è stato sviluppato un modello numerico migliorato, comprendente tutte le geometrie analizzate in studi precedenti, al fine di avere una formulazione in grado di descrivere il comportamento complessivo dei sistemi analizzati.

Il primo capitolo presenta la descrizione dei PCMs (tipi, caratteristiche e applicazioni), includendo anche le azioni intraprese al fine di migliorare la conducibilità termica.
Il secondo capitolo mostra la descrizione del sistema per gli esperimenti, compresa la parte relativa alle termocoppie utilizzate.
Il terzo capitolo sviluppa i risultati dell'analisi, con diversi confronti tra diverse proprietà.
Il quarto capitolo è relativo alle simulazioni ANSYS (Fluent).
Il quinto e ultimo capitolo presenta la spiegazione del modello numerico di partenza, quello proposto, e infine i risultati aggiornati dell'ultimo, e le conclusioni sui PCM.

Il caso analizzato vede l'utilizzo dello stesso tipo di PCM, quello organico, con tre paraffine, come già riportato, con diversa temperatura di fusione. Questi sono stati acquistati dalla *Rubitherm Technologies GmbH* ed i vantaggi nell'uso di un tale PCM sono legati alla loro sicurezza in termini di tossicità e corrosività. Le proprietà principali sono elencate nella *Tabella 1*. Le caratteristiche principali, invece, sono quelle elencate precedentemente, vale a dire l'elevato calore latente e la ridotta variazione di volume durante il cambio di fase. Tuttavia, la limitazione più importante rimane ancora la bassa conducibilità termica 0,2 W m^{-1} K^{-1}.

Proprietà	RT42	RT55	RT64HC
Temperatura di fusione, T_{fus} [° C]	42	55	64
Area di congelamento, T_{cong} [° C]	43 ÷ 37	56 ÷ 57	64 ÷ 61
Calore specifico, cp [kJ kg^{-1} K^{-1}]	2	2	2
Calore latente, h [kJ kg^{-1}]	165	170	250
Densità fase solida, ϱ_{sol} [kg m^{-3}]	880	880	880
Densità fase liquida, ϱ_{liq} [kg m^{-3}]	760	770	780
Conducibilità termica, k [W m^{-1} K^{-1}]	0.2	0.2	0.2
Variazione di volume [%]	12.5	14	11

Tabella 1 – Proprietà dei PCMs utilizzati

I parametri geometrici caratterizzanti la geometria reticolare analizzata sono il lato del cubo l e lo spessore della fibra t (lato cubo l = 10 mm, spessore fibra s = 0,8 mm, porosità ε = 93%). Le dimensioni complessive delle celle risultano essere 100 × 20 × 100 mm.
Il modulo di prova è composto da:

- Struttura in alluminio, avente dimensioni 100 × 40 × 100 mm,
  composta da:

  - Struttura in alluminio, dimensioni 100 × 20 × 100 mm
  - Piastre laterali in alluminio, aventi dimensioni 100 × 10 × 100 mm ciascuna

- Base in bachelite (15 × 40 × 120 mm) e sostegno posteriore (100 × 40 × 15 mm)
- Vetro frontale, dimensioni 100 × 40 × 4 mm
- Riscaldatore in rame, con dimensioni 100 × 10 × 100 mm
- Alloggiamento in Teflon isolante

Al fine di fornire l'adeguato apporto di calore al PCM, è stato utilizzato un riscaldatore elettrico alimentato da un generatore di corrente CC, per effetto Joule. Il flusso di calore è stato fissato a 20 kW m^{-2}, in modo da poter, variando la corrente e la tensione del generatore, ottenere valori inferiori di potenza specifica, ovvero 10 e 15 kW m^{-2}. In questo modo, tenendo conto delle caratteristiche geometriche precedentemente riportate del riscaldatore, 100 × 10 × 100 mm, la struttura reticolare selezionata è stata testata per una potenza pari a 100, 150 e 200 W. Per quanto riguarda la fabbricazione della piastra, il riscaldatore è composto da una piastra di rame all'interno della quale è stata fresata una guida. All'interno della guida è stata inserita una resistenza al filo nichel-cromo. La piastra di alluminio sinistra è appoggiata al riscaldatore elettrico, quindi i campioni vengono riscaldati dal lato sinistro, mentre sul lato destro sono praticati tre fori sul lato destro della piastra in alluminio, dove sono inserite tre termocoppie, in aggiunta a quelle inserite nella parte superiore delle piastre di alluminio, lato riscaldato e non riscaldato. La punta delle stesse è inserita a metà strada tra la piastra sinistra (riscaldata) e quella destra. In questo modo, viene misurata la temperatura della paraffina nel mezzo del reticolo. I fori sono stati praticati a 25 mm, 50 mm e 75 mm di distanza dal lato inferiore lungo la linea mediana verticale della piastra, e lo stesso processo viene eseguito per l'alloggiamento isolante in Teflon, completando la struttura, riportata di seguito in *Figura 1*.

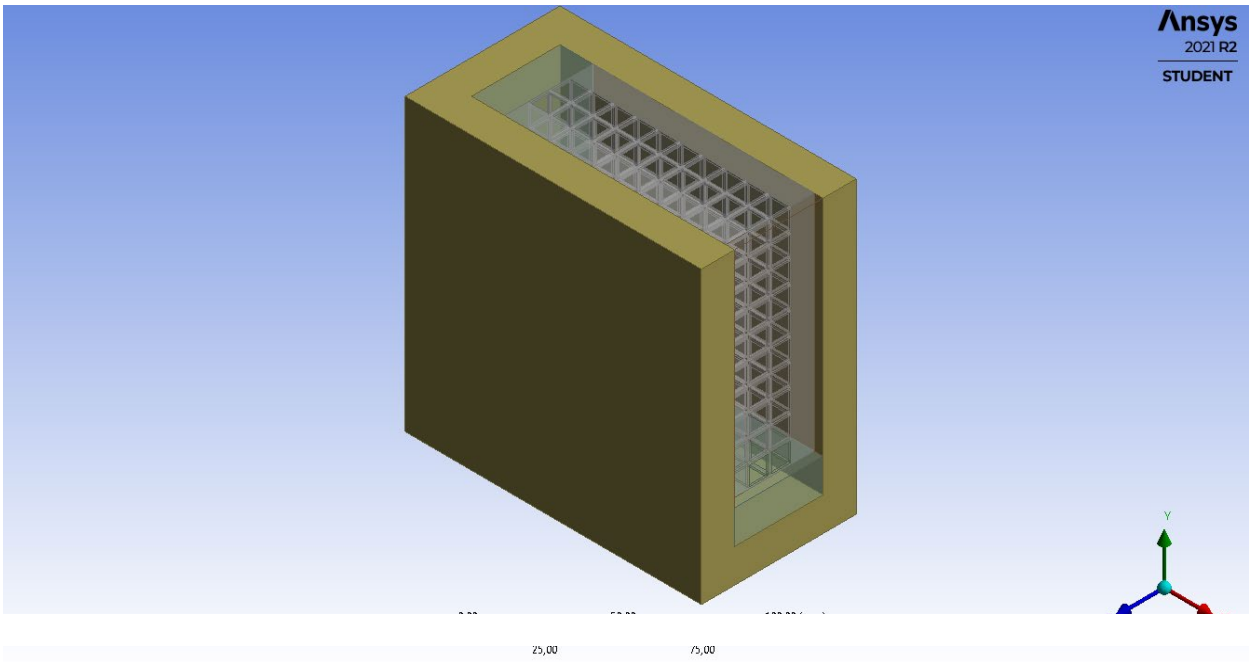

Figura 1 – Struttura complessiva del modulo

La struttura metallica risolve il problema legato alla bassa conducibilità termica ed in particolare la geometria analizzata presenta valori di temperatura finale più elevati rispetto alle altre geometrie, oltre ad un tempo maggiore necessario per completare la fusione. Alcune modifiche possono essere fatte cambiando la porosità della struttura metallica, portando a tempi ancora più elevati per la fusione, ma temperature finali ridotte. La simulazione numerica è stata eseguita utilizzando il software ANSYS (Fluent) 2021. Le diverse prove sperimentali consentono di far notare come il fronte di fusione proceda quasi parallelamente dal lato riscaldato a quello adiabatico. Questo comportamento è dovuto al reticolo dell'alluminio, poiché la possibilità di movimento della fase liquida è limitata e, di conseguenza, la convezione naturale. Va ricordato come la conducibilità termica dell'alluminio sia quasi tre ordini di grandezza maggiore di quella della paraffina considerata. Inoltre, come è possibile notare dalle curve di temperatura fornite dalle tre termocoppie inserite a 25, 50 e 75 mm di altezza nel PCM, il gradiente verticale è trascurabile. Tuttavia, questo fenomeno può essere meglio osservato negli esperimenti condotti da Diani e Campanale [1], in un modulo di prova senza la struttura metallica all'interno. Una volta affrontato e analizzato questo problema, sono state introdotte le seguenti semplificazioni:

- Densità costante della paraffina
- Temperatura di fusione costante
- Scambio termico radiante trascurato
- Analisi di una sezione verticale, con spessore di 10 mm (100×40×10)

L'ultima considerazione porta all'analisi della geometria data come modello simmetrico, anche se il modulo non riflette questa peculiarità. Infatti, in realtà, vi è la presenza del lato frontale in vetro, mentre il lato posteriore della struttura è isolato con 15 mm di Bachelite e Teflon ciascuno. Poiché il calcolo in questo caso è stato fatto tenendo conto solo di una fila di celle sulle dieci che compongono l'insieme, i trasferimenti di calore relativi alle due superfici elencate sono stati trascurati.

Le simulazioni condotte con ANSYS Fluent, nonostante la rappresentazione del caso reale sia stata ricreata adeguatamente, hanno mostrato importanti limiti per quanto riguarda la descrizione del fronte di fusione, portando a risultati complessivi più che corretti, ma con importanti limiti. L'analisi si è concentrata sulle curve di temperatura dell'alluminio e del PCM, ricordando sempre come, ancora una volta per le semplificazioni, il processo di fusione fosse rappresentato nelle simulazioni come una linea isoterma.

In particolare, questo fatto è legato alla scelta di imporre una densità costante, e quindi l'assenza di espansione durante il cambiamento di fase e della convezione naturale, e all'adozione di una temperatura fissa per il processo di fusione, senza un intervallo di temperatura tra la fase solida e quella liquida. In conclusione, la simulazione rappresenta adeguatamente il lato riscaldato, mentre per il contributo dei PCM sono presenti importanti discrepanze dal caso reale.
Per quanto riguarda l'ultima analisi nel corso di questa trattazione, ovvero lo sviluppo del modello numerico a partire dal lavoro di Diani e Campanale [1], è stato possibile rappresentare graficamente la temperatura adimensionale θ in funzione del prodotto tra il numero di Fourier e il numero di Stefan:

$$Fo \cdot Ste = \frac{k_{eff} \cdot t_{fus} \cdot (T_{fus} - T_i)}{\rho_{eff} \cdot h^2 \cdot L_{eff}} \quad (1)$$

Ad elevati valori di questo prodotto e ridotti valori della temperatura adimensionale θ, corrisponde un ridotto flusso di calore.

La correlazione finale mostrata da Diani e Campanale [1] risulta essere:

$$\theta = 1.9073 \cdot \ (Fo \cdot Ste)^{-0.717} \quad (2)$$

È stata introdotta un'ulteriore costante c_3 alla precedente, esponente del prodotto aggiunto tra a_{sv}, rapporto tra la superficie e il volume della struttura [m^{-1}] e la distanza del fronte di fusione dalla piastra riscaldata, cioè l'altezza del PCM perpendicolare al fronte di fusione (0,02 m per le attuali strutture testate).
La nuova formulazione risulterà essere del tipo:

$$\theta = c_1 \cdot \ (Fo \cdot Ste)^{c_2} \cdot (a_{sv} \cdot h)^{c_3} \quad (3)$$

tutta la procedura è stata codificata in Matlab, con l'inserimento dei dati provenienti dai test sperimentali in corso e dei valori ottenuti nelle osservazioni passate. In particolare, è stata sviluppata una formulazione per le geometrie reticolari, quelle BCC e infine e la formulazione generale comprensiva di tutte le strutture. L'equazione (3) viene utilizzata per il calcolo il tempo necessario per fondere la paraffina inserita nella struttura metallica data, nonché la temperatura del lato a contatto con il riscaldatore.

Questa equazione deve essere associata ad un bilancio energetico dell'intero sistema, che dipende dall'applicazione specifica , come [1]:

$$q \cdot A_{risc} \cdot t_{fus} = m_{PCM} \cdot L_{PCM} + m_{PCM} \cdot c_{p,PCM} \cdot \left(\frac{T_f + T_{fus}}{2} - T_i\right) + m_{Al} \cdot c_{p,Al} \cdot \left(\frac{T_f + T_{fus}}{2} - T_i\right) + m_{risc} \cdot c_{p,risc}\left(T_f - T_i\right) + \sum_i Q_i \quad (4)$$

Il termine di sinistra corrisponde all'energia termica totale fornita dal riscaldatore, i termini sul lato destro corrispondono, rispettivamente, al calore latente per fondere completamente il PCM, calore sensibile necessario per portare il PCM alla sua temperatura finale (valore medio tra la temperatura della piastra riscaldata e la temperatura di fusione), calore necessario per portare la struttura alla sua temperatura finale (valore medio tra la temperatura della piastra riscaldata e la temperatura di fusione), calore necessario per portare il riscaldatore dalla temperatura iniziale a quella finale. L'ultimo termine sul lato destro corrisponde al calore necessario per portare tutti i componenti di contorno dalla loro temperatura iniziale alla loro temperatura finale: dipende dal caso specifico, per la geometria analizzata corrisponde alle piastre in alluminio sinistra e destra, alle piastre Bakelite, ed infine all'alloggiamento in Teflon.

Le equazioni (3) e (4) formano un sistema di due incognite, T_f e t_{fus}, la temperatura raggiunta dalla piastra riscaldata alla fine del processo di fusione e il tempo necessario per fondere completamente la paraffina.

Per la geometria con porosità del 93%

$$\theta = 2.0818 \cdot (Fo \cdot Ste)^{-0.776} \cdot (a_{sv} \cdot h)^{-0.017} \quad (5)$$

Ret 10 precedente	errore relativo medio [%]	errore assoluto medio [%]
87%	-30.72	30.72
93%	-32.32	32.32
entrambe	-31.52	31.52

Tabella 2 - Valori degli errori con la precedente correlazione, per la struttura reticolare (10 mm)

Ret 10 nuovo	errore relativo medio [%]	errore assoluto medio [%]
87%	0.92	9.19
93%	0.3	4.66
entrambe	0.02	6.89

Tabella 3 - Valori degli errori con la nuova correlazione, per la struttura reticolare (10 mm)

T_i [°C]	q [W]	T_{fus} [°C]	t_{fus_dati} [s]	$Tf_{\_dati}$ [°C]	t_{fus_calc} [s]	$Tf_{\_calc}$ [°C]	$dev_{ass}(t_{fus})$ [%]	$dev_{ass}(Tf)$ [-]
24.97	100	42	977	74.26	980	78.31	0.31	0.055
23.62	150	42	767	85.65	733	88.55	4.43	0.034
25.04	200	42	621	96.78	571	98.11	8.05	0.014
25.56	100	55	1327	86.15	1400	86.07	5.50	0.001
26.54	150	55	947	98.73	980	96.12	3.48	0.026
24.90	200	55	776	110.3	798	104.05	2.84	0.057
25.56	100	64	1853	98.44	1831	99.97	1.19	0.016
24.15	150	64	1302	112.2	1322	111.07	1.54	0.010
26.61	200	64	985	122.51	1008	121.83	2.34	0.006

Tabella 4 – deviazioni dei valori of T_f e t_{fus} calcolati con la correlazione dai valori sperimentali

Come è possibile notare, i valori complessivi degli errori sono inferiori al 10%, portando ad una rappresentazione dei test condotti più che buona. Inoltre, fatta eccezione per quattro casi su diciotto, le deviazioni calcolate risultano essere addirittura inferiori al 5%. L'ultimo passaggio è stato quello di verificare se le dissipazioni nel sistema fossero al di sotto del valore del 10%.

	potenza [W]	dissipazioni [%]
RT42	100	1.52
	150	2.47
	200	1.88
RT55	100	2.03
	150	2.66
	200	3.72
RT64HC	100	2.01
	150	2.26
	200	2.38

Tabella 4 – Risultati finali sulle dissipazioni del sistema

I contributi complessivi tengono conto della massima dissipazione: sul lato riscaldato, conduzione in alluminio, riscaldatore, Teflon e convezione con aria esterna, sul lato non riscaldato, conduzione in alluminio e Teflon e convezione con aria esterna, lato anteriore, considerando la differenza di temperatura tra PCM e aria, tenendo conto del termine di resistenza termica fornito dal componente in vetro e dall'aria esterna, il lato posteriore, la conduzione in Bachelite e Teflon e la convezione con aria esterna ed infine il lato superiore, tenendo conto della convezione con l'aria, considerando ciascuna differenza di temperatura. Tutti questi termini, analizzati insieme al bilancio energetico, portano alla definizione finale delle dissipazioni presenti nel sistema. Come è possibile vedere, tutti i valori sono al di sotto del limite massimo che è stato presentato in precedenza.

In conclusione, le nuove correlazioni fornite hanno migliorato quella più precedente, utilizzata come base importante per iniziare lo studio, con un'approssimazione migliore dei risultati ottenuti nei test condotti. Tutti i vincoli sui valori di deviazioni e dissipazioni sono stati rispettati e il modello finale complessivo risulta utilizzabile per gli studi futuri.

Index

Introduction

The main advantage of the PCMs in different fields, shown in *Paragraph 1.3*, is related to the possibility of storing great amount of heat with a relatively small variation in the volume. The phase change material is in solid phase at ambient temperature, and the thermal energy is stored thanks to the change to liquid phase. This property is interesting if thought related to the use of the renewable energy sources (RES). It is well known how an important issue related to the RES is their discontinuity and their randomly variation [2]. Adopting storage solutions helps the integration of these technologies and the progressive reduction in the use of the fossil fuels, firstly critical for the environmental impact and secondly for the scarcity of those sources.

However, the main focus of this master thesis is related to the cooling process in electronic components, addressing the heat dissipation issue.

It is important to remember how this case study analyses three paraffin in details, but the applications can be different in a wide range, the melting temperature of the PCMs has to be chosen in relationship with the field of use. Furthermore, other advantages in the use of the paraffin are the non-flammability at usual applications' temperatures and non-toxicity of the material. On the other side, it will be possible to address and see how to solve the problem related to the low thermal conductivity, which affects the overall heat transfer. The conducted studies in the laboratory had the aim to see the best coupling metal matrix – paraffin and compare the different behaviour from one case study to another.

Chapter 1 – Phase Change Materials

1.1 Energy storage

There are different types of energy that can be stored: electrical energy (chemical storage with hydrogen, electrochemical with batteries and purely electrical with supercapacitors), mechanical energy (flywheels, compressed air, or hydroelectric basins) and finally thermal energy. For the last one, subject of the study, the storage can be done thanks to an internal energy variation, related to the sensible or latent, or thermochemical heat exchange [3].

With focus on the sensible heat exchange, the thermal energy is stored increasing the temperature of a solid or of a fluid. The stored heat Q [J] is influenced by the mass m [kg], of the material, by the specific heat capacity c_p [J kg^{-1} K^{-1}] of the material considered, and finally by the temperature difference between the initial T_i one and the final T_f one, ΔT [K]. The following equation shows that:

$$Q = m \cdot c_p \cdot \Delta T \tag{1.1}$$

The water, due to its properties, contextually high specific heat capacity and reduced cost, is the best solution for this type of heat exchange. The main problem is related to the phase change threshold of 100°C: for this reason, above the seen value, the water is substituted with oils, molten salt and liquid metal. There are domestic and industrial applications, or even for district heating networks [4].

The latent heat storage exploits the phase change of a substance, from solid to liquid, liquid-vapour, solid-vapour or solid-solid [4]. The heat exchange occurs in isothermal conditions, where the constant temperature is the melting one [3]. In the case study, the phase change from solid to liquid, allows to achieve a greater energy density, and so lower volume required and lower volume variation, compared to the liquid-vapour phase change. Furthermore, it has a greater latent heat compared to the solid-solid phase change. Generalizing, the high energy density related to the latent heat is directly linked to the efficiency of the exchange itself, which is for this reason greater than the sensible one.

The heat exchanged is expressed by the following equation:

$$Q = m \cdot \Delta H \tag{1.2}$$

where the stored heat is Q [J], m is the mass [kg], and ΔH is the variation of enthalpy related to the phase change [J kg^{-1}]. This is the general formulation, in order to show the storage capacity of these systems:

$$Q = \int_{T_i}^{T_m} m \cdot c_p \cdot dT + m \cdot \Delta H + \int_{Tm}^{T_f} m \cdot c_p \cdot dT \tag{1.3}$$

The written terms are the ones in (1.1) and (1.2) and T_m [K] is the melting temperature.

Finally, the thermochemical heat exchange is related to the breaking and subsequent formation of the chemical bonds in a reversible reaction. The energy contribution is absorbed and released during these processes and is related to the endothermic heat of reaction. However, the main issue related to these phenomena is the stability [4]: there is a degradation of the materials in time and the efficiency is not constant. Nowadays, this solution has not been studied sufficiently and in a detailed way, so the development is not so common.

1.2 Classification and properties

The phase change materials can be classified in three different ways [4]: based on the chemistry, on the phase transition or on the melting temperature.

1.2.1 Chemistry

This first distinction distinguishes three categories (figure 1.1):

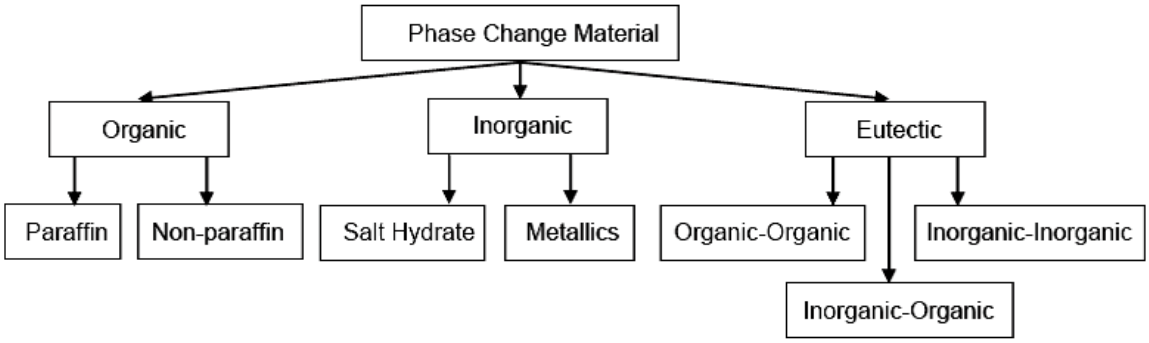

Figure 1.1 – Differences related to the chemistry for the distinction and classification of PCMs

The organic PCMs are paraffin and non-paraffin as esters, alcohols, glycols, fat acids or polymers. The inorganic PCMs are salt hydrate and metallics and finally, the eutectic PCMs are subdivided in mixtures of organic and inorganic PCMs.

1.2.1.1 Organic PCMs

The organic PCMs are classified in paraffin and non-paraffin and their composition is based on hydrogen and carbon chains [5]. These are composed by alkanes, with a variable number of carbon atoms between 8 and 40, depending on the type of paraffine (pure o wax): the pure paraffine has a number of the mentioned above atom varying between 14 and 40, while, as for the current application, the paraffine wax has a lower value, between 8 and 15. The property deriving from the number of carbon atoms is the melting temperature, directly proportional to that.

An important characteristic of these materials is their stability, related also to their poor degradation in time. Furthermore, they are not corrosive, not costly, chemically inert, with low variations of volume (as maximum value 10%) and finally stable below 500°C, as well as available in a large temperature range. On the cons side, their low thermal conductivity leads to long melting and solidification times, as well as thermal gradients. In addition, some of them are flammable. As a result, overall, the amount of energy generated is low (this consideration is still true for the organic PCMs in general).

The non-paraffin are widely used, from esters to alcohols, or glycols, fat acids and polymers. They have a broad spectrum of physical and thermochemical properties [3]. Due to their flammability, there should be no exposition to high temperatures, oxidant agents or, of course, to flames. In addition, they are slightly toxic. For the second type of characteristics, common to all paraffin, the thermal conductivity is low, while the latent heat is high. Furthermore, these substances can be melted and solidified different times without reaching the liquid subcooling, defined as the solidification of the material at a reduced temperature compared to the phase change [5]. The problem related to this issue is related to the necessity of having the external temperature decreasing to have the operative cycle, since the PCM during the cooling phase does not release the energy previously absorbed. Talking about costs, the one of non-paraffin is almost double than the paraffin one. The overall pros and cons are reported below:

Pros:

- High latent heat of melting
- Available in a wide range of temperatures
- Low capacity of liquid subcooling
- Thermal and chemical stability
- Low reactivity
- Not corrosive (applications with construction materials)
- Recyclable

Cons:

- Low thermal conductivity
- Low enthalpy
- Flammable (depending on the paraffin)

1.2.1.2 Inorganic PCMs

The inorganic PCMs are classified in two different types: hydrates and metallic salts, where the first ones contain crystallized water [5]. Salt are used above 150 °C until 900 °C, remembering that the melting enthalpy increases proportionally with the melting temperature expressed in K [6]. The main problem with the hydrates salts is related to their freezing in low-temperature region.

In addition, these materials encounter a separation of materials during the phase change, but, as noted from Kimura and Kai [7], with the addition of NaCl (1% in mass) inside of $CaCl_2 \cdot 6H_2O$, this problem is obviated. The second ones, metallic salts, are not really used to store thermal energy, due to the fact that they present a high weight. Overall, the melting point is higher than the organic PCMs, but the most interesting characteristics are the relatively high thermal conductivity (around 0.5 W m^{-1} K^{-1}) and their high absorption capacity per unit volume (300 ÷ 350 MJ m^{-3}). The summary of the overall pros and cons is listed below:

Pros:

- High thermal conductivity
- Low cost
- Great availability
- High enthalpy
- Contained volume variation
- Almost null flammability
- Low environmental impact
- Possibility to use them with plastic containers

Cons:

- Separation of materials during phase change
- Low nucleation properties
- Occurring of the subcooling of liquid phase
- High decomposition
- Low thermal stability
- Corrosive when in contact with metals (not compatible with construction materials)
- Slightly toxic

Compared to the organic PCMs, the main advantages presented by these materials are related to the high thermal conductivity and their non-flammability. However, their incompatibility with construction materials, as it will be reported in the display of the case study, and their toxicity limit the possibility of employing them in some applications.

1.2.1.3 Eutectic PCMs

This last category is a hybrid between the previous presented, since they are composed by two or more organic, inorganic or both PCMs [5]. With a proper mixing of the different materials available, it is possible to obtain the wanted melting temperature for the given application. This advantage is not achievable with the categories of PCMs listed before. Furthermore, they present a high enthalpy. On the other side, clearly, they present a higher cost compared with the others, almost three times, and limited thermodynamic properties.

1.2.2 Properties

In order to be efficiently used, a PCM should present the following properties:

1. Thermal properties:

    - High latent heat
    - Adequate temperature of the phase change

The melting temperature needs to be chosen based on the operating temperature, in order to have it the closest possible to the last one. Furthermore, a high value of latent heat corresponds to a reduced physical dimension of the storage system. Finally, the high thermal conductivity allows to obtain acceptable melting and solidification times.

2. Physical properties:

    - High density
    - Low volume variation
    - Low vapour tension

3. Kinetic properties:

    - No subcooling
    - Proper crystallization speed

4. Chemical properties:

    - Long-term chemical stability
    - Compatibility with other materials
    - Nontoxicity
    - Non flammability

5. Economic properties:

    - Low cost
    - High possibility of recycling

1.3 Applications for PCMs

The main advantage related to PCM is their intrinsic property of being able to store energy thanks to the change of phase. The first evident employment can be seen in the renewable energy technologies, such as photovoltaic and wind turbines since the production of these is quite discontinuous and varies randomly [8].

Adopting storage solutions helps their integration and the progressive reduction in the use of the fossil fuels, which are critical for the environmental impact and also scarce. However, the applications are not limited to the RES field, but see other important presences in the cooling of electronic devices, in the food industry for the conservation and transport of food and beverages, in buildings, in the textile sector and others.

1.3.1 PCMs in solar energy systems

The great advantages related to the solar energy are the following ones:

- It is totally free
- It is greater than the human needs (in less than one hour the incoming energy is equal to the annual energy consumed worldwide)
- It is widespread through the planet
- It is inexhaustible
- It has a low environmental impact

On the other side, as already stated, it is randomly variable, generally not "in phase" with the human needs (during the late afternoon and evening, when the needs are quite important, there is no presence of solar radiation) and finally it is possible to exploit in a proficient way in clear sky conditions [8]. From these points of view, the advantage in the use of PCMs is related to the storage of energy since the solar energy can be stored as thermal energy and then release at the occurrence of the need. The existing available technologies are systems to produce hot water and thermal system for the electricity production.

In systems for the production of domestic hot water, the great advantage is related to the savings achieved in terms of energy, and subsequently the reduction of the emissions related to the main alternative production of hot water with natural gas or other fossil fuels. The problem related to this application has to be found in the very low efficiency during cold days or cloudy sky, since there is a great dispersion of heat during the night. Nevertheless, the use of PCMs can solve, at least partially, this issue.

An interesting result is coming from Narayanan et al. [9], showing the coupling of a heating system with an eutectic PCM, with an addition of graphite nano-particles in order to enhance the thermal conductivity. The evident result is a better storage of the solar energy obtaining a more efficient conversion of the incoming light into heat. In addition, subsequently to the addition of the graphite and the improved thermal conductivity, there is a shortening of the storage time and energy transfer, with a benefit on the overall system. Another interesting case was studied by Riahi et al. [10]. This study provided an insight into the thermal performance and exergy efficiency of a cascade PCM-graphite system compared with the cascade PCMs, as well as the sensible heat storage systems of two-tanks and the graphite system. Moreover, it provided a means for a first level design and selection of cascade systems to achieve higher exergy efficiency for a specific exergy delivery coupled with the CSP cycle. As a result, the overall exergy efficiency of the two-tank systems is between 52.2 and 52.7%, in comparison to cascade PCMs with 49.67–50.12%. At the next level, a hybrid system of PCM-graphite provides about 49.48% and a system comprising of graphite as a solid sensible heat storage offers about 50% exergy efficiency. The higher exergy efficiency can be expected using PCMs with the melting temperature achieving the same phase change time, and higher thermal energy storage and release for different sections of the system. Moving to solar collectors, the results obtained by Khalifa et al. [11], in particular composed by six copper tubes having 80 mm of diameter with a paraffin inside, the behaviour is the subsequent: when there is no solar radiation, the liquid PCM cools down, transferring heat to the water, which maintains its temperature constant in a given time interval. Now it is interesting to focus on the electricity production [8]: an important development can be found in solar power towers, CSP (Concentrating Solar Power) technologies. The components are a central tower with a receiver on top, which concentrates the solar radiation incoming from a field of heliostats all around it. The actual applications see the use of molten salt, air or helium at 600-1200°C, pressure range in between 1-20 bar. Among the CSP technologies, the solar power tower is the second most developed after the parabolic trough in terms of technology mix, and has the great advantage, compared to the cited one, of reaching higher temperatures due to its conformation. With the solar radiation concentrated in the point concentrator, the heat is transferred to a working fluid that will carry it to the central where the electric energy is then produced (figure 1.2) [12].

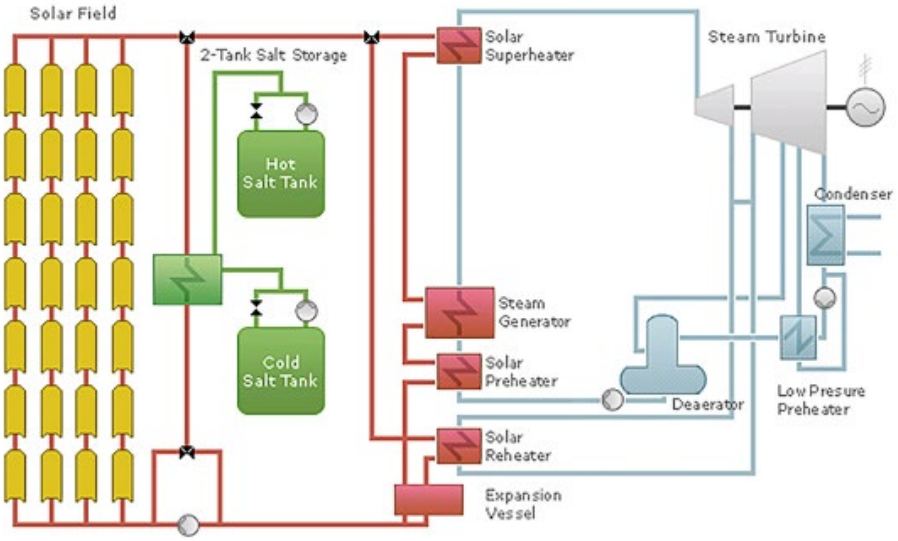

Figure 1.2 - Baseline plant configuration with indirect two-tank molten salt TES

1.3.2 PCMs for the cooling of electronics.

It is well-known how the performances of the electronic devices are strictly related to their operative temperature. A long condition of temperature out of the proper range comports a life reduction of the technology. A first analysis in literature has been carried out by Kandasamy et al. [13] with PCM-based heat sinks that can effectively store the dissipated heat from the components below a critical temperature, with an input power level relatively high for the first studies ($q > 2$ W cm^{-2}). Heat pipes with PCMs inside can be adopted as shown from Krishna et al. [14]: with this solution there is a sensible reduction of the energy needed to cool down the condenser, and also lower values about 10-15°C in the temperature at the evaporator. In addition, a fundamental component as the battery is heavily influenced by the temperature, presenting malfunctioning if subjected to overheating and an important reduction in the power with low temperatures. Using the PCMs it is possible to have a control on the temperature and subsequently a better operating condition.

1.3.3 PCMs in textile industry

In order to improve the thermal insulation level of clothes, the use of PCMs can be important, exploiting the isothermal property of these materials during the phase change.

There are different ways in order to integrate PCMs in textiles [6]:

- Microencapsulation, filling specific bags
- Microencapsulation, during the production process of the textile. The dimensions are in the order of micrometres
- Composite materials, composite powders made by PCMs and polymeric material

As reported from Mondal [18], a treated fabric with 22.9% add-on of microcapsules is able to absorb 4.44 J/g of heat if the microcapsules, in this case melamine–formaldehyde microcapsules containing eicosane, on the fabric undergo a melting process. The heat of absorption by them delays the microclimate temperature increase of clothing. This leads to enhanced thermo-physiological comfort and prevents heat stress. A further interesting analysis is given from Itani et al. [19], with the study of different types of vests cooled using PCM. The main issue was to find the proper position to locate the phase change material and the number of pockets containing it. In particular, the last choice was determined by the ambient temperature, with the use of 8, 10 or 20 pockets respectively for a temperature of 28°C, 35°C or 45°C.

1.3.4 PCMs for conservation and transport of food and beverages

Between the different fields of application for the PCMs, the food industry is a current field [8]. As reported from Alehosseini and Jafari [15] the preservation of many foods at refrigerated conditions and maintenance of low temperatures during storage and transportation is fundamental to avoid or postpone microbial, physical, and chemical changes. In this way, the use of PCMs may help in preventing temperature fluctuations. In addition, the high importance of energy saving in the food industry and its direct effect on the final price of manufactured food products is another important issue to be considered. In their study, along the analysis of the different techniques for the encapsulation, it is pointed out how the use of micro/nano-encapsulated PCMs, improves, as expected, the thermal storage capacity of the heat transfer fluids used in the analysis.
Some applications are reported in *Table 1.1*.

Type of phase change materials (PCMs)	Shell material	Encapsulation technique	Results	Application
Paraffin waxes of Rubitherm RT4® (RT4), Rubitherm RT-4® (RT-4)	Polycaprolactone (PCL), polystyrene (PS), and high-impact polystyrene (HIPS)	Electrospinning	Achieving a high encapsulation efficiency	Food packaging
Paraffin RT2, RT-4, and water with 10% food grade propylene glycol	-	-	Negligible super-cooling of paraffin and its low latent heat in system	Chilled food refrigerated cabinets
Climsel C-18 and Cristopia E−21	-	-	Maintaining product temperature using E21: −16/-12 °C and C-18: −12/-7 °C	Food transportation system
Dodecane	Zein	Uniaxial and coaxial electrospinning	Better yields of the coaxial electrospinning	Smart food packaging
Cristopia E−21	-	-	Preserving ice cream quality during storage	Ice cream containers
Paraffin wax of Rubitherm RT5	Polystyrene (PS)	Electrospinning	High encapsulation efficiency	Food packaging
Paraffin wax	-	-	Achieving a high energy saving	Drying of sweet potato
De-ionized water (98%) and borax (2%)	-	-	The uniform food temperature distribution	Food refrigerated cabinets
Rubitherm RT6	Nano-structured calcium silicate (NCS)	Physical entrapment	Sufficient thermal buffering capacity	Food packaging
Dodecane	Polycaprolactone (PCL) and polylactide (PLA)	Uniaxial electrospinning	Comparison of encapsulation efficiency: PCL/PCM=83% PLA/PCM=51%	Smart packaging
Paraffin hexadecane	-	Combination of Emulsification and ultrasonic treatment	Changing size diameter of particles	Research project (study on subcooling in hexadecane emulsions)
Octadecane and eicosane	Titanium dioxide (TiO2)-Polyvinylpyrrolidone (PVP) composite	Melt coaxial electrospinning	Development of long-chain hydrocarbon cores and composite sheaths	Controlled release
Rubitherm RT-2	-	-	Thermal protection in longer periods	Chilly bins
Climsel C-18 and Cristopia E−21	Polypropylene (PP), high density polyethylene (HDPE), polyethylene terephthalate (PET), and polystyrene (PS)	Physical coating	Showing negative reactions between copper and carbon steel structures containing PCM	Research project (for cold storage applications)

Table 2.1 - Selected studies on microencapsulated PCMs fabricated using different polymerization methods

1.3.5 PCMs in buildings

With the improvement of the life conditions, nowadays an essential requisite when talking about buildings is the so called “thermal comfort” [8]: defined as a mental condition of satisfaction related to the thermal environment, it implies a constantly increase in the energy consumptions as the parameter improves. A possible solution is given by the use of PCMs in this field, in order to improve the comfort and at the same time diminishing the contribution on the energy spent. An interesting analysis conducted by Shah et al. [16] shows the investigation of the difference in peak temperatures between both surfaces of a glazed window and the occurrence time. It was noted that the incorporation of the nanoparticles of PCM was helpful in reducing the consumption of cooling energy. Furthermore, it was pointed out a shift in the peak electricity consumption during summertime.

The additional introduction of conductive nanomaterials, such as carbon nanotubes or metallic nanoparticles, are able to improve the thermal conductivity of PCMs (*Table 1.2*). Lee et al. [17] used a salt-based hydrate with a melting peak temperature of 31.4 °C for their study. It was found that thermal comfort was improved as the peak heat flux was reduced by 36.4% in the walls containing PCMs. Moreover, peak heat fluxes are delayed when presenting a heat insulation and heat absorption phase change material layer. In conclusion, the material studied have significant impacts on passive cooling on the building.

PCM	Nanoparticle	Melting temperature of PCM* / PCM Composite** (° C)	Latent heat capacity of PCM* / PCM Composite** (J g^{-1})	Purpose	Key findings
Paraffin	MWCNT	27.1**	89.4**	To produce thermal energy storage cement-based composites	· Thermal conductivity increased by 42.45% · Increase in PCM heat storage and heat release rates
Hexadecane Octadecane Paraffin	xGnP	22.1** 30.2** 54.9**	120.8** 126.1** 63.8**	To investigate the thermal performance of SSPCM for building applications using xGnP	· Thermal conductivity increased by 133%. · Indoor temperature reduced by 0–6 °C
Paraffin	Cu CuO Al_2O_3	27-29**	205*	To develop advanced window units using NEPCM	· Enhancement of optical and thermal performance · Decrease in peak temperature on the interior surface of window · Increase in time lag of window unit · Recommended volume fraction of CuO under 1% and under the size of 15 nm
Paraffin	Al_2O_3	26.9*	212.3*	To investigate the thermal performance of NEPCM in ceiling board	· Absorption of heat flux increased by 15% · Inner surface temperature of ceiling remained almost constant at 26.6 ° C when temperature of outer roof surface changes from 25 to 50 ° C
n-octadecane	CNF	27.9*	69.7*	To enhance the thermal and mechanical properties of cement mortar	· Compressive strength increased by 22% · Thermal conductivity increased by 1% for 0.5 wt% of PCM/CNF nanocomposite
LA-SA	Al_2O_3	21.3**	205.9**	To develop a novel encapsulated SSPCM with ceramsite for building envelope	· Thermal conductivity increased by 43.3% for 0.5 wt% Al2O3 · Optimum mass fraction of PCM Composite (15%) meets the demand of stress bearing capacity (0.4 MPa) as a building material
Paraffin	Al_2O_3 TiO_2 ZnO	27-29**	205**	To investigate the impact of PCM with nanoparticles on the seasonal thermal performance of double-glazed windows	· In summer, peak temperature of interior surface increased by 0.19 K for Al2O3 and decreased by 0.82 K and 0.36 K for TiO2 and ZnO respectively · In transition season, peak temperature of interior surface increased by 0.56 K, 0.1 K and 0.84 K for Al2O3, TiO2 and ZnO respectively · In winter, peak temperature of interior surface increased by 0.55 K, 0.66 K and 0.89 K for Al2O3, TiO2 and ZnO respectively

Table 1.2 - Summary of published studies related to nanotechnology-incorporated phase change materials for building applications

1.3.6 PCMs in the heat recovery systems

In order to achieve greater energy savings and reduction in the emissions, it is important the application of phase change materials in the heat recovery systems. The issue related to the heat production and utilization is the distinction between the two phases in terms of space and time [8]. This problem is obviated thanks to their employment, and the subsequent exploitation of the stored latent heat. Numerous cases have been already illustrated in the previous paragraphs, but in addition to them, an interesting solution was studied by Gu et al. [20] in an air conditioning system. The experimental results indicate that technical grade paraffine wax with the additive, LP (liquid paraffin) or LA (lauric acid), qualify as PCM for heat recovery of air conditioning system. The addition of a solvent was related to the need of diminishing the melting temperature of the paraffin wax. Moreover, paraffin wax with 40% LP or 14,89% LA satisfies the temperature demand of the system, in addition to a congruent melting and freezing temperatures, the last one without super-cooling. Another important reported characteristic was related to the stability in time, over twenty heating and cooling cycles, with a volume contraction of the phase change process from liquid to solid below 12%. The only highlighted problem was related to the lauric acid because it is expensive. However, using liquid paraffin (paraffin oil), the melting point of the paraffin wax is still lowered, and the recovery of the unexploited heat was achieved successfully.

1.4 Improvement of the thermal conductivity

The problem related to the use of phase change materials has been already stated. In this way, the energy transfer is difficult in a short time, and in addition, in electronics application for example, the reached temperatures are too high to have an adequate cooling of the components [1]. One possible solution is to insert into the PCMs a solid material, with a high thermal conductivity, in order to improve the one of the overall PCM-solid material systems. Another possible solution is to scatter nanoparticles or microencapsulated spheres into the phase change material, again improving, thanks to their higher thermal conductivity, the overall property. It is important to observe how the convection process, with the pure liquid phase PCM, improves the overall heat transfer. However, the addition of any material, both macroscopically and microscopically, will reduce or even eliminate the convection in the liquid phase.

It is important, for this reason, to choose the best solution in order to achieve the proper result.

1.4.1 Solid medium application

There are three particular ways in order to improve the thermal conductivity of a PCM with the use of a solid material inside of it. The improvement is related to the heat transfer inside the new created system. It is possible to use finned surfaces, metallic foams, or carbon-based applications, due to its high porosity and thermal conductivity.

1.4.1.1 Finned surfaces

This solution is one of the most well-known and studied in literature, exploiting the increase of the exchange surface of the PCMs and the subsequent improvement of the conductive and convective heat exchange. Hosseinizadeh et al. [21] noted two peculiar behaviours of a heat sink with and without the PCM: increasing the number of fins and fin height led to an overall increase of the thermal performance and increasing the fin thickness only gave slight improvement. Furthermore, still related to fin height, the melt starting time was delayed and the melting period was reduced. Finally, they noticed how the lower regions of the PCM for the thin fins seemed to melt faster in the first period, while, in advanced stages, the upper part of the PCM appeared to melt faster. This fact is related to the internal fluid convection, which is a far more effective heat transfer mechanism compared to heat conduction within the PCM. Kim et al. [22] made a comparison between an enhanced cooling performance phase change material-integrated fin-type heat sink and a conventional fin-type heat sink in high power electronics with two localized hot spots. The investigated heating power, seen the field of application, were 400-800 W. It was possible to notice how the PCM solution improved the cooling properties of the system, even in convection-limited cooling environments (figure 1.3).

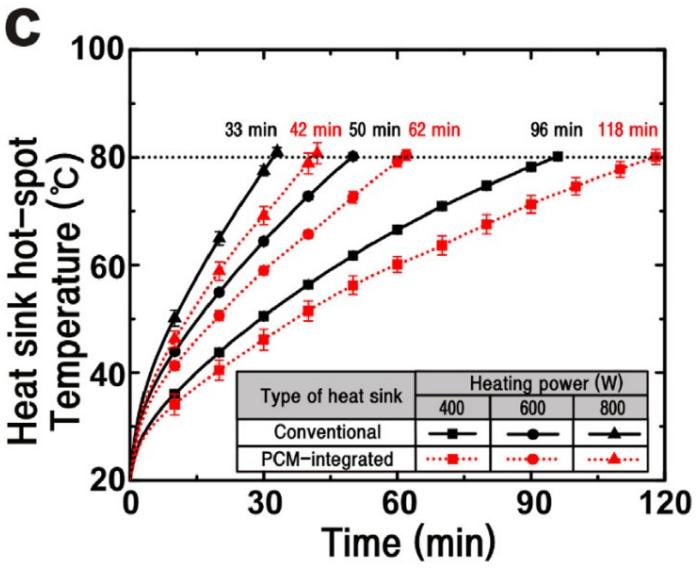

Figure 1.3 - Experimental and numerical results on cooling performance of the conventional and the PCM-integrated fin-type heat sinks. (c) Hot-spot temperature profiles of the heat sinks in terms of time upon different heating powers under reduced cooling condition.

1.4.1.2 Metallic foams

The aim of the metallic foams is the same stated in the previous paragraph: to improve the thermal conductivity of the PCMs. Metal foams are cellular materials with randomly oriented ligaments which form open or closed cells [1]. Metal foams are primarily characterized by two parameters: PPI, the number of pores that can be counted in a linear inch, and porosity, the ratio between the volume occupied by the air and the total volume, the volume of the air summed to the one of the solid. The use of metal foams as conductive medium, inside which phase change materials can be embedded to enhance their thermal conductivity, has been proposed in the open literature.

One of the first works regarding melting of PCMs embedded in metal foams was the one of Lafdi et al. [23] which experimentally investigated the solid-liquid phase transition of paraffin wax inside metal foams. The tested foam was an aluminum one with 5, 10, 20 and 40 PPI and porosity from 88.6% to 96.6%. The paraffin wax melting temperature ranged between 25.4 °C and 28.9 °C. The effect of pore size on the heater temperature was minor than that of porosity and the heater temperature was comparatively lower for the lower porosity foams than for the higher porosity foams due to greater heat conduction through the foam material. Chen et al. [24] carried out an experimental study on the melting behaviour of a paraffin wax, with melting temperature between 55 °C and 60 °C, embedded in aluminum foams.

With the use of an infrared camera and an optical microscope, the temperature field and the melting evolution of the PCM at the pore scale were studied, respectively. They also implemented a thermal Lattice Boltzmann model to simulate the two dimensional melting of the phase change material in metal foams. Baby and Balaji [25] studied the heat transfer performance of a PCM based copper metal foam, with N-eicosane used for this experiment. The structure was heated from a side, changing the inclination with respect to the horizontal axis (0, 25, 45, 60, 75, 90, 110, 130, 150, 180 and 210°). However, the result obtained showed how this parameter is not influencing the process, since after 90 minutes, the maximum temperature difference at the hot base in the different cases was lower than 0.5 °C. Defining the ratio between the time needed for the foam-PCM system and for the pure PCM to reach the temperature 52 °C and the ratio between the time needed for the foam-PCM system and for the foam to reach the temperature 52 °C, it was shown how the first ratio is increasing with an increase of the power supplied from the heater, reaching a maximum value of 715 for 10 W applied, while the second one was not influenced by the supplied power.

1.4.1.3 Carbon-based applications

The advantages related to carbon-based materials are the high thermal conductivity. Low density and the chemical stability [8]. Carbon based materials have a variety of morphological structures, such as expended graphite (EG), carbon fiber (CF), graphene, carbon nanotube (CNT).

Alshaer et al. [26] developed thermal control systems for the electronics in order to see the effect on the thermal conductivity. These systems were composed by a pure carbon foam and carbon nanotubes. Two different structures were tested, with different thermal conductivity: CF-20 with a lower value of 3.1 W m^{-1} K^{-1} and KL1-250 with a higher value of 40 W m^{-1} K^{-1} . Different levels of power were applied, and the thermal response was analysed. Overall, a reduction in the temperature in the PCM-foam module compared to the pure foam module was signalled. This reduction was even more enhanced with the addition of the carbon nanotubes. This behaviour has to be attributed to the conductive network between the foam and the nanotubes, that produced the overall increase in the thermal conductivity. This result was noted for each different power level.

In the comparison between the two different structures, it was highlighted how the one with higher thermal conductivity was able to absorb a larger amount of thermal power given the same temperature and, vice versa, a lower level of temperature was reached given the same power. KL1-250 was so able to better control high thermal loads.

However, the introduction of the nanotubes was more efficient in the CF-20, since the structure taken into account presented a lower value of thermal conductivity and in this way the improvement was more appreciable.

Mallow et al. [27] compared the thermal performances of aluminum and graphite foams saturated with phase change materials. Their melting temperatures were 54 °C and 37 °C, respectively.

It was shown that the thermal charging enhancement of graphite foams was superior to that of aluminum foams, on the basis of thermal charging rate and junction temperature due to high thermal conductivity, low density, and small pore size. Based on the experimental results, they developed a power law to relate Fourier number and dimensionless temperature. Tang et al. [28] put together the palmitic acid and capric acid to formulate eutectic mixtures as PCM, and utilized the diatomite as supporting material, and added expended graphite (EG) to improve the thermal conductivity of composite PCM. The results showed that the thermal conductivity of the composite PCM without EG is 0.119 W m^{-1} K^{-1} in freezing state and 0.190 W m^{-1} K^{-1} in melting state. The thermal conductivity of the composite PCM with 3 wt% (percentage by weight) and 5 wt% EG was improved by 15.1% and 25.2% in freezing state, and the thermal conductivity of the composite PCM with 3 wt% and 5 wt% EG was improved by 26.3% and 53.7% in the melting state. As the latent heat of the composite PCM is reduced slightly with the increase in mass fraction of EG, the composite PCM with 5 wt% EG is selected as the optimal one. In summary, carbon based materials as additives show the main advantages of high thermal conductivity, stable chemical property, and low density. There is no doubt that the high thermal conductivity of additives is beneficial to improve the thermal conductivity of PCMs, however, the most important factor is the aspect ratio, large aspect ratio of additives results in good thermal conductivity enhancement.

1.4.2 Nanoparticles and encapsulation

In recent years, different innovative systems were developed in order to improve the thermal conductivity of the phase change materials. Essentially, particles with dimensions lower than 100 nm, with high thermal conductivity, can be dispersed inside the PCMs, or to insert the PCMs can be inserted inside capsules. In the first case the category is called PCMs with nanoparticles addition, in the second one encapsulated PCMs.

1.4.2.1 Nanoparticles

As it has already been stated, the advantage in using the nanoparticles inside the PCMs is related to the improvement of the thermal conductivity [29]. The main problem is related to the Van der Waals forces, which can cause adhesion and subsequent deposit of the nanoparticles, reducing the effectiveness of the addition. The required characteristics from these materials are their chemical stability, in order to avoid chemical reactions inside the PCMs, and of course a high thermal conductivity. Praveen and Suresh [30] studied the thermal and chemical properties and heat transfer performance of a solid-solid nano-enhanced PCM (SSPCM) comprising of neopentyl glycol (NPG) and copper oxide (CuO) nanoparticles for its possible usage in thermal energy storage (TES) based heat sink application. The SSPCM samples were prepared by mixing NPG with CuO nanoparticle in 0.5, 1 and 3% weight proportions (figure 1.4 a,b). As result, the thermal conductivity of the composite SSPCMs measured through laser flash technique, showed a maximum relative enhancement of about 4.08 to the value for pure NPG with 3 wt% CuO nanoparticle additions and the time needed to reach a temperature of 60 °C during heating of the heat sink was increased by 2.36 times the time taken without using any PCM by the addition of 3wt% of CuO nanoparticles. This made the heat sink to be maintained at a lower temperature for a longer period of time. Also, addition of CuO nanoparticles in the NPG reduced the recovery time of the heat sink during cooling. Bahiraei et al. [31] used three different carbon-based nanostructures embedded in a paraffin. These carbon additives were carbon nano-fiber (CNF), graphene nano-platelets (GNP) and graphite nano-powder (GrP). Four different samples were prepared for each structure, 2.5wt%, 5wt%, 7.5wt% and 10wt%, respectively. On one hand, the increase in thermal conductivity was 620% and 1100% for the 7.5wt% and 10wt%. On the other hand, nanoparticles severely degrade natural convection heat transfer in the liquid phase, due to the viscosity increase. For this reason, the two samples with the higher percentage by weight showed a reduced final temperature compared with the pure paraffin, after 1000 s.

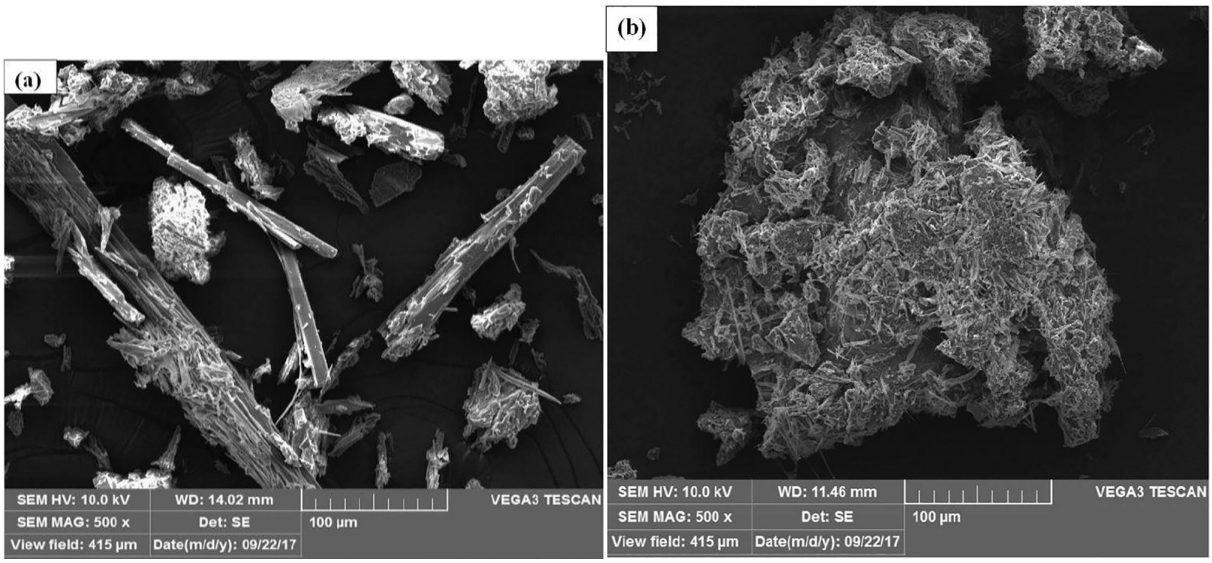

Figure 1.4 – Surface morphology and particle dispersion of NPG, NPG added with CuO nanoparticles. (a) SEM image of NPG; (b) NPG added with CuO.

1.4.2.2 Encapsulation

There are two different existing types of encapsulation: microencapsulation and macroencapsulation [5]. The microencapsulation is based on the introduction of PCM into tubes, panels, or other large containers, which have more than 1 cm of diameter. Using this technique, it is possible to fit a significant amount of PCM in a single container. The main advantages of this method are the easy transport and handling, the possibility of the encapsulation design specifically for the intended application, a better compatibility with the material and the reduction of external volume changes. The disadvantages are the low thermal conductivity, the need of protection containment elements against the destruction and the possibility of PCM solidification in the corners and edges, with subsequent reduction of the heat transfer.

Microencapsulation methods are basically divided into three different categories [32]:

- Chemical processes
- Physical-chemical processes
- Mechanical processes

Chemical processes are essentially polymerization, polycondensation or dispersion processes in which the wall of the microcapsule is formed in-situ. Physical-chemical methods are those in which walls are formed by preformed polymers by processes such as solvent removal. Mechanical processes include a variety of spray processes and fluid deposition coating processes. One of the most widely used methods for PCM microencapsulation is the dispersion of PCM droplets in an aqueous solution and the formation of polymer walls around the droplets using techniques such as coacervation, interfacial polycondensation and other in situ polymerization processes.

The choice of the microencapsulation process as well as the material for capsule formation is of particular relevance, due to the fact that its subsequent application depends on its chemical, physical, and mechanical stability. The macroencapsulation is a widely used and efficient method to incorporate PCM into prefabricated walls and roofs. In this case, the PCM is not mixed with the basic materials, such as concrete and mortar. In this way, the decrease of the mechanical characteristics of the basic materials is avoided. Generally, the performance of the PCM macroencapsulation strongly depends on several factors, starting from the location of the PCM macrocapsule, following with the microclimate conditions, the configuration of the building element, the thermal properties of the building material and, finally, the PCM type. Some examples are reported in figure 1.5.

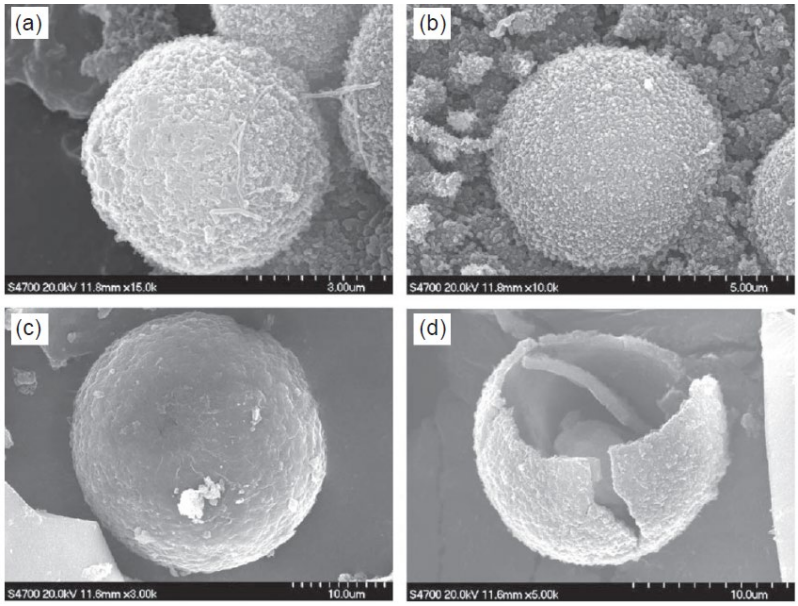

Figure 1.5 – SEM images of the microcapsules synthetized by using different amine monomers: (a) EDA, (b) DETA, (c) Jeffamine, and (d) cracked microcapsule particle (source: Zhang and Wang, 2009a)

CHAPTER 2 – Experimental equipment

2.1 Overview on the selected PCMs

The case study provided sees the use of the same type of PCM, the organic one, with three different paraffin due to their melting temperature. These PCMs were bought from *Rubitherm Technologies GmbH*, and the advantages in the use of such a PCM are related to their safety in terms of toxicity and corrosivity. The main properties are listed in *Table 2.1*. The main characteristics are the ones listed in the previous chapter, namely high latent heat and reduced variation in volume during the phase change.

However, the main problem still remains the low thermal conductivity, 0.2 W m^{-1} K^{-1}.

Property	RT42	RT55	RT64HC
Fusion temperature, T_{melt} [° C]	42	55	64
Congealing area, T_{cong} [° C]	43 ÷ 37	56 ÷ 57	64 ÷ 61
Melting area, T_{melt} [° C]	38 ÷ 43	51 ÷ 57	63 ÷ 65
Specific heat capacity, cp [kJ kg^{-1} K^{-1}]	2	2	2
Latent heat, h [kJ kg^{-1}]	165	170	250
Density solid, ϱ_{sol} [kg m^{-3}]	880	880	880
Density liquid, ϱ_{liq} [kg m^{-3}]	760	770	780
Thermal conductivity, k [W m^{-1} K^{-1}]	0,2	0,2	0,2
Volume expansion [%]	12,5	14	11

Table 3.1 – Properties of the used PCMs

2.2 Overview on the structures

2.2.1 Body-Centred-Cubic structure (BCC)

The already printed geometry present in the laboratory was obtained from a full cubic body subtracting the spheres located at the vertexes of the cube itself [33].

The geometrical characterizing parameters are the side of the cube l and the radius of the spheres r. Since this is only a geometry used for a comparison, further construction details will be omitted, the focus will be on the physical dimensions. The relative density, defined as the ratio between the volume occupied by the solid and the total volume, of the two structures is set the same, what changes is the dimension of the cell, related to previous studies. The two main parameters are listed below:

- BCC structure, cube side l = 5 mm, radius of the spheres r = 5.10 mm
- BCC structure, cube side l = 10 mm, radius of the spheres r = 10.20 mm

The overall relative density was fixed at the 13%, so that the complementary porosity is 87%, and all the elementary cells were located one side of another. As it will be shown multiples times later on, the overall cells dimensions were 100 × 20 × 100 mm. In order to transfer heat from the side heater and to contain the paraffin, two aluminum plates were used, one on the left side and the other on the right side.
The dimensions of those were 100 × 10 × 100 mm, leading to a total dimension of the main structure of 100 × 40 × 100 mm, common to all the other geometries.

2.2.2 Lattice structure

In recent years, the rapid prototyping technology of metal developed rapidly, and topics as 3D printing (additive manufacturing technology) started to attract extensive attention. In particular, Hu and Gong [34] presented a schematic diagram of aluminum foam which consisted of cubic periodic cells. The basic unit of aluminum foam is ideal cube-shaped, in which aluminum struts are connected together with 90° angle at each vertex. Paraffin wax is impregnated in the pore space of aluminum foam as PCM. The metal geometry with cubic periodic cell possesses all specificity of a metal foam, high thermal conductivity, high porous structure, and low relative density. Once again, the geometrical characterizing parameters are the side of the cube l and the fibre thickness t. In order to better understand the construction figure 2.2 is displayed as an example.

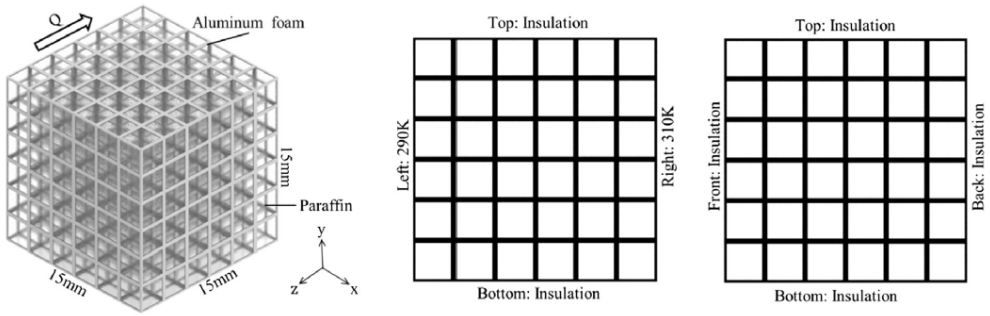

Figure 2.1 – Lattice structure basic construction figure

The main parameters of the tested structures are listed below:

- lattice structure, cube side l = 10 mm, fibre thickness t = 0.8 mm , porosity ε = 93% (this will be the case study, figure 2.3 a and b)
- lattice structure, cube side l = 5 mm, fibre thickness t = 0.4 mm , porosity ε = 93%
- lattice structure, cube side l = 10 mm, fibre thickness t = 1.13 mm , porosity ε = 87%
- lattice structure, cube side l = 5 mm, fibre thickness t = 0.565 mm , porosity ε = 87%

Each structure was printed between two 10 mm thick plates, as it will be presented in the following paragraph.

The dimensions of each plate were 100 × 10 × 100 mm, leading to a total dimension of the main structure of 100 × 40 × 100 mm, common to all the other geometries (figure 2.3 and figure 2.4).

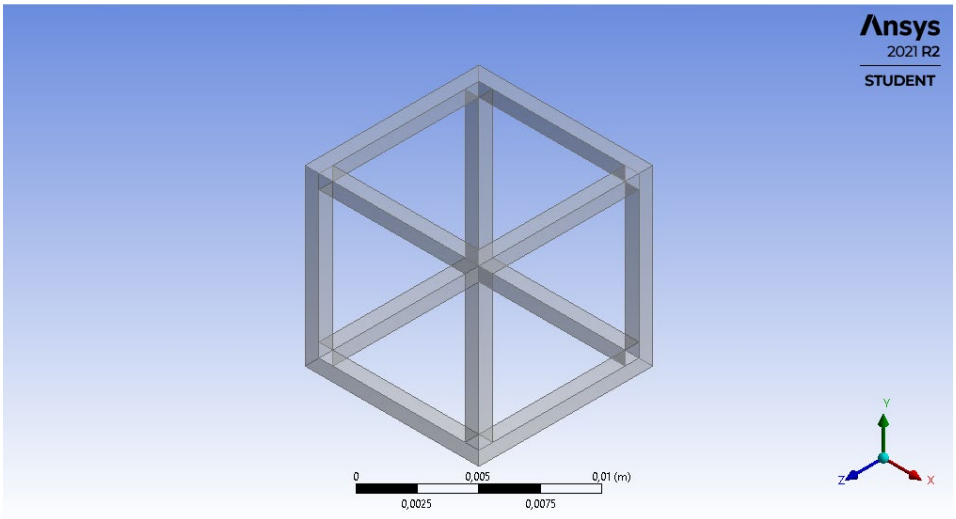

Figure 2.2 - Unitary cell for the lattice geometry (first prospective)

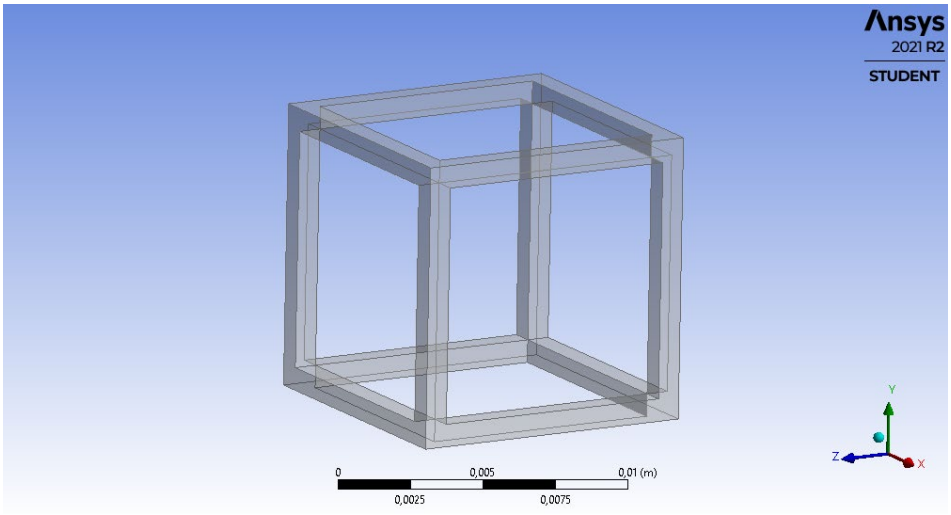

Figure 2.3 – Unitary cell for the lattice geometry (second prospective)

2.3 Presentation of the case study

The test module is essentially composed by:

- Total aluminum structure, having dimension 100 × 40 × 100 mm (figure 2.5), composed by:
    - Aluminum structure, having dimension 100 × 20 × 100 mm
    - Aluminum lateral plates, having dimension 100 × 10 × 100 mm each one
- Bakelite base (15 × 40 × 120 mm) and rear sustain (100 × 40 × 15 mm)
- Frontal glass, having dimension 100 × 40 × 4 mm
- Heater made by copper, having dimension 100 × 10 × 100 mm
- Insulant Teflon housing

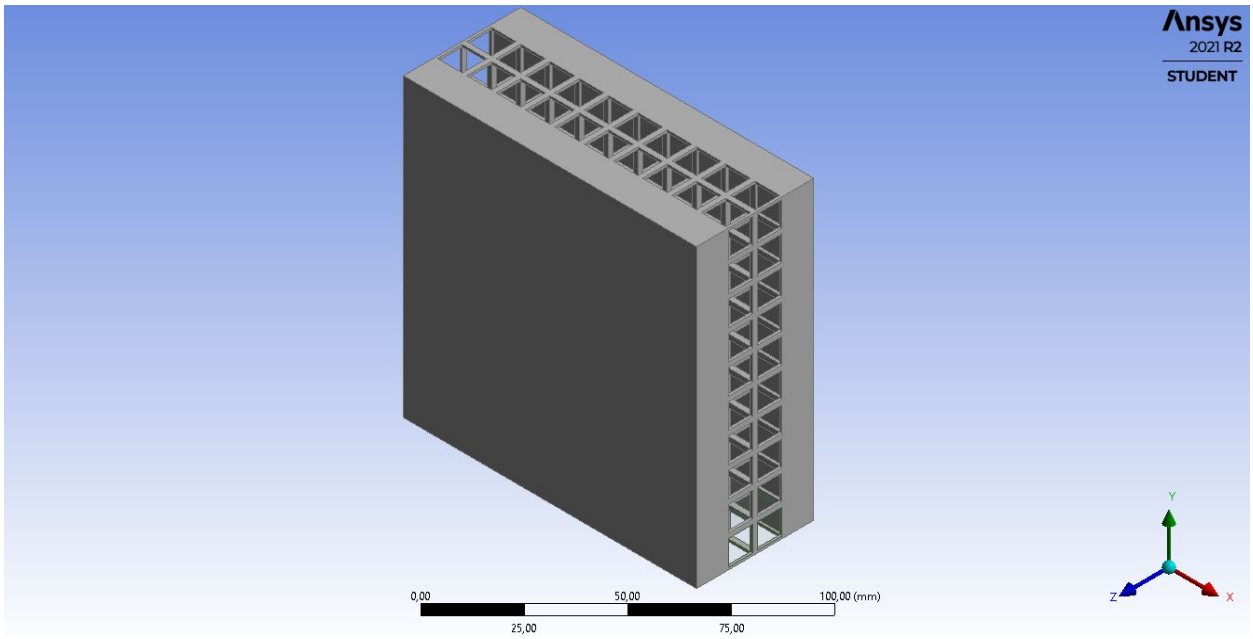

Figure 2.4 – Heat transfer support structure made by aluminum alloy

The creation of the aluminum structure was reported in the previous paragraphs, the physical properties of the used alloy are listed in *Table 2.1.*

Property	AlSi10Mg
Thermal conductivity, *k* [W m^{-1} K^{-1}]	175
Specific heat capacity, *cp* [J kg^{-1} K^{-1}]	900 ± 50
Density, *ρ* [kg m^{-3}]	2670

Table 2.1 – Physical properties of the aluminum alloy

There is no presence of discontinuity between the cells and the lateral plates since they are obtained from the same technology. A further process needed to be done, since all the necessary instrumentation for the measurements has to be inserted: different holes and slots in order to collocate the different thermocouples, six for the heated and six for the adiabatic side (figure 2.6).

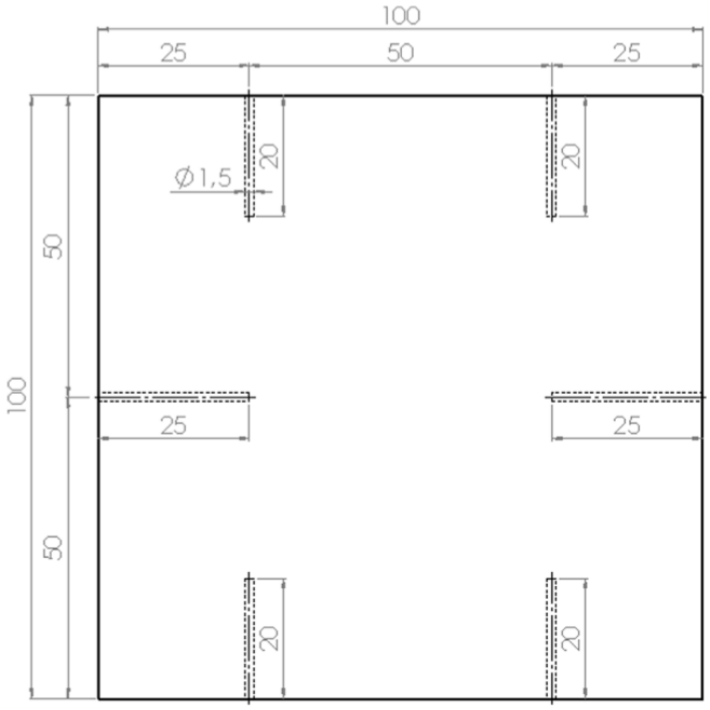

Figure 2.5 – Location of the thermocouples

The bottom and rear sides are covered with Bakelite, an insulating material, glued to the plates between which the main structure is brazed. Each Bakelite side is 15mm thick as reported previously. The front side is covered with a glass window (figure 2.7), glued thanks to silicon *Saratoga* to the two aluminum plates. The glass window is needed to observe the development of the melting front of the paraffin embedded into the structure. The melting front propagation of the paraffin will be described by means of pictures taken with a 12 Mpixel camera.

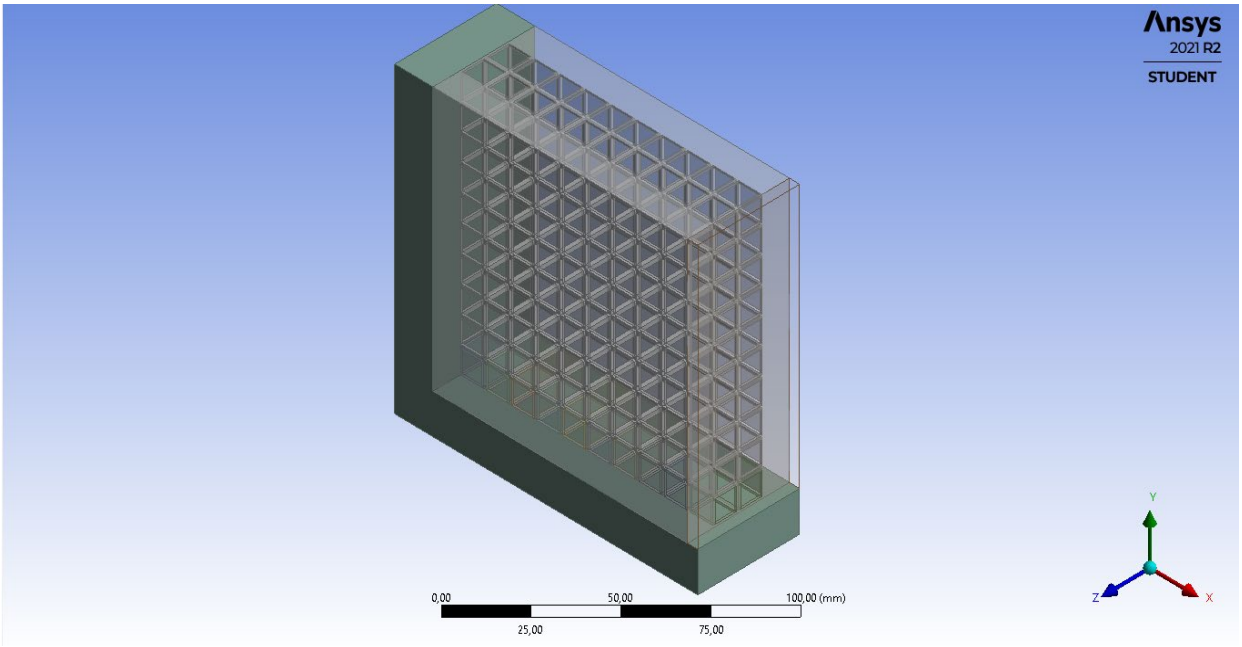

Figure 2.6 – Overall structure without heater and Teflon casing

In order to provide the adequate heat flow rate to the PCM, an electric heater powered by a DC current generator, was used. The heat flux was set at 20 kW m^{-2}, in order to be able, varying the current and the tension of the generator, to obtain lower values of specific power, namely 10 and 15 kW m^{-2}. In this way, taking into account the previously reported geometrical characteristics of the heater, 100 × 10 × 100 mm, the selected lattice structure will be tested for heat flow rate equals to 100, 150, and 200 W. Talking about the manufacturing of the plate, the heater is composed by a copper plate inside which a guide was milled as reported in figure 2.7. A nickel-chrome wire resistance was inserted inside the guide. The left aluminum plate is leant against the electrical heater, therefore the samples are heated from the left side, while on the right side three holes were drilled on the right side of the aluminum plate.

The tip of the probes is inserted halfway between the left (heated) plate and the right one. In this way, they measure the temperature of the paraffin in the middle of the lattice. The holes were drilled 25 mm, 50 mm, and 75 mm apart from the bottom side along the vertical centreline of the plate, and the same process is done for the insulant Teflon housing, completing the structure (figure 2.8) [1].

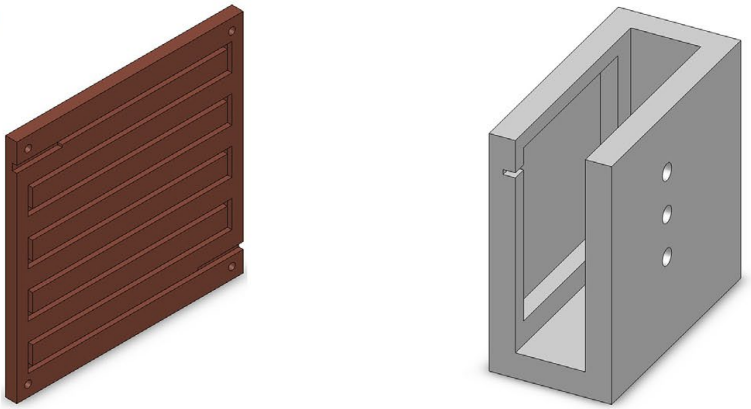

Figure 2.7 – Heater (left side) and casing in Teflon (right side)

The overall structure is reported below (figure 2.9).

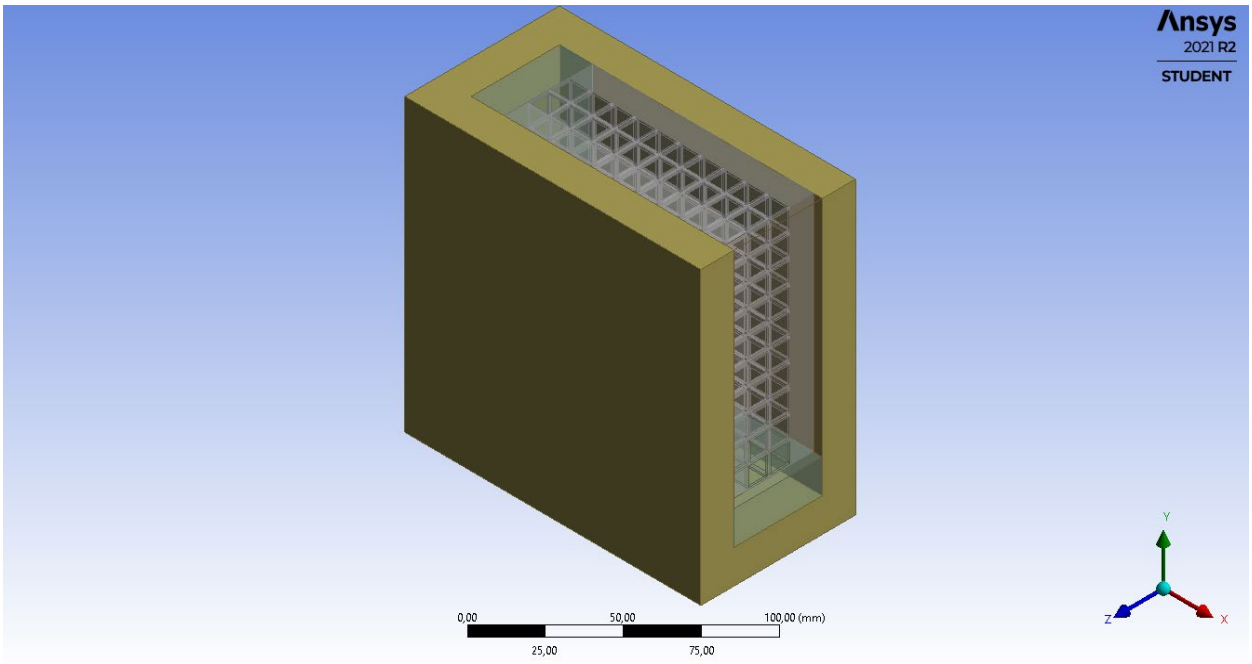

Figure 2.8 – Overall structure of the test module

2.4 Overview on the instrumentation

The following instrumentation was used during the calibration:

- *Kaye K170* ice-point reference, which gives the reference value of the temperature for the cold junction of the used thermocouples, 0 °C.
- *Agilent A34970* acquisition system, with the conversion of the voltage signal coming from the thermocouples to a digital signal, sent to the main computer of the laboratory. This system presents three boards, with 60 channels (1-20, 21-40, 41-60).
- *Techne RB-12A* thermostatic bath (associated to a Pt100 thermoresistance for the calibration). Thanks to its display, it is possible to set the constant temperature that has to be maintained for the water.
- *Pt100 thermoresistance,* ± 0.03 °C accuracy, reference for the calibration.
- *Dc current generator.*
- *T-type thermocouples,* copper/constantan, inserted in 1 mm thick stainless-steel probes, ± 0.05 °C accuracy.
- *Copper/constantan thermocouples,* inserted in the aluminum plates, ± 0.05 °C accuracy.

2.4 Thermocouples calibration

As it was stated in the previous paragraph, the temperature of the PCM was measured thanks to the T-type thermocouples. The reference thermoresistance for the calibration is the Pt100, with low uncertainty and an accuracy of ± 0.3 °K. The considered range of temperatures signalled from the T-type thermocouples was ± 0.5 °C with respect to analysed temperatures from the Pt100. The thermocouples were connected to the *Kaye K170* ice-point reference and to the *Agilent A34970* acquisition system, which allows the conversion tension-digital signal. Then both the thermocouples to be calibrated and the Pt100 were put into the thermostatic bath, trying to maintain them at the same hight and without having any contact between parts. The first step was taking the thermostatic bath at a 20 °C temperature, and once it was reached, the value reported from the Pt100 was measured and the initialization started. It is necessary to wait the proper amount of time in order to reach the state condition.

Once it is reached, it is possible to vary the temperature of 10 °C, having the analysis for the range 20 °C – 70 °C, in order then to evaluate the differences between the values obtained from the Pt100 and the T-type thermocouples, within the already stated range.

For each value of temperature (10, 20, 30, 40, 50, 60, 70 ° C) the mean voltage value on 100 measured values was calculated. For the conversion from the output in [mV], x in the formula represents the mean voltage obtained from the 100 readings in [V], and the temperature in [°C], which is y in the formula, was calculated thanks to the following polynomial expression:

$$y = a + bx + cx^2 + dx^3 + ex^4 \tag{2.1}$$

where the values of each constant are listed below, and the results reported in figure 2.10:

- a = 0.01334110023
- b = 25.96625448
- c = -0.6625435429
- d = -0.03685919268
- e = 0.01678956801

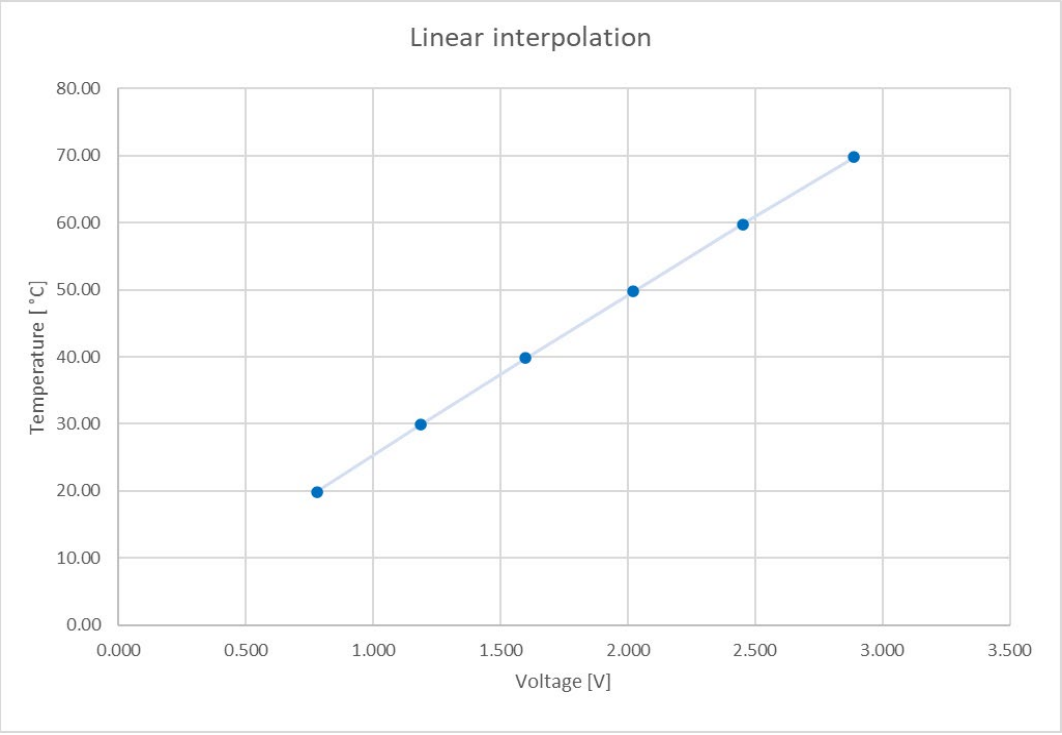

Figure 2.9 – Graphical representation of the polynomial expression for the calibration of the thermocouples

CHAPTER 3 – Experimental analysis

3.1 Followed procedure

First of all, the structure needs to be filled with the chosen paraffin. In order to do so, it is possible to proceed by heating in a proper container the paraffin at a temperature higher than the melting one, thanks to an electric heater, in order to be able to pour the PCM in the module without having any solidification and formation of void spaces or bubbles. The geometry is filled. Now it is only a matter to wait for the solidification, and once it is occurred, due to the contraction in the phase change, it is possible to pour a little bit more of paraffin in the structure in order to add some material to the module. It is important to remember that the paraffin will melt again later on, so this final procedure needs to be done carefully, without filling completely the structure, or it will be present the risk of overflooding from the top.
Said so, the procedure for each test is exactly the same for every different paraffin and heat flow rate selected:

- Switching on the instrumentation and waiting for the state conditions to be achieved (*Kaye K170* temperature level).
- Regulation of the generator in order to obtain the desired power level.
- Simultaneous starting of the acquisition system, camera for the images acquisition and generator.
- Recognition of the total melting of the paraffin after a given variable time interval.
- Switching off the instrumentation, namely the acquisition system, the camera, and the generator.

This procedure is repeated for the three different heat flow rates (100, 150, 200 W corresponding to the heat fluxes 10, 15, 20 kW m^{-2}), then the test module is emptied and the paraffin changed.

The obtained data from the software *Labview* are listed in the following way:

- First column: time interval from the starting of the instrumentation to the switching off.
- Second to sixth columns: temperature values of the six T-thermocouples on the heated side.
- Seventh to twelfth columns: temperature values of the six T-thermocouples on the adiabatic side.
- Thirteenth to fifteenth columns: temperature values of the three lateral thermocouples, inserted in the middle of the structure and so of the PCM.
- Sixteenth to eighteenth columns: ambient temperature values.
- Nineteenth column: value of the generator current.
- Twentieth column: value of the generator voltage.

The data obtained were firstly transferred to an *Excel* file and secondly to the *software Matlab* for the final reduction.
In order to be able to present the graphical results of the data, there was the need to evaluate:

- The mean temperature on the heated side, given by the mean of the six T-thermocouples on that side.
- The mean temperature on the adiabatic side, given by the mean of the six T-thermocouples on that side.

And some other parameters, reported now for completeness, which will be used in a following chapter:

- The mean initial ambient temperature.
- The mean initial temperature of the PCM, given by the mean of the three thermocouples on the lateral side.

In this way it is possible to represent the progress of the studied variables:

- Graph of the values obtained from the thermocouples on the heated and adiabatic side, as function of the time.
- Graph of the values obtained from the lateral thermocouples, as function of the time.

The two graphs have been merged in order to have a better overall picture of the behaviour.
Since in a following chapter the comparison between the test results and the ones recreated with the *software ANSYS Fluent* will be reported, the graph of the mean values of temperature obtained from the different thermocouples will be represented later on.

Once the results were analysed, a comparison was made in terms of:

- Different paraffin.
- Different thermal powers applied.
- Differences between the case study and previous studied structures.

3.2 Presentation of the results

This chapter reports the achieved results from the tests on the presented module, using the already listed paraffin, as well as the different applied heat flow rates. The following figures are shown:

- Graph temperature-time on the heated, adiabatic, and lateral side, reporting the different temperatures in the aluminum structure and PCM, from the beginning of the experiment to the complete melting (figure 3.1). It is important to remember that the temperatures are expressed as mean of the obtained values.
- Images taken with the camera from the frontal glass, extracted every 60 s from the videos. The time interval was chosen based on the possibility to individuate variations in the aspect of the paraffin itself (figure 3.2).

As it will be possible to be seen, the trend of the provided curves is similar for each effectuated test. For this reason, it is possible to notice, neglecting the final contributions when the melting was almost totally achieved, how the three curves related to the lateral thermocouples inserted in the PCM are quite overlapped. The phenomenon is related to the fact that there is no presence of thermal gradients in the vertical direction. It is even more evident in the provided images since the melting front is parallel to the heated side. However, the departure from the explained behaviour in the final period of melting can be seen in the front variation, starting from the top and then propagating to the bottom [1]. This is due to the fact that there is an expansion during the phase change (*Table 2.1*). Following the melting of the paraffin, the subsequent expansion occurs over the uncovered side, exposed to air: in this way the higher parts of the paraffin melt rapidly. Nevertheless, thanks to the use of the metallic structure, a limitation of the convective currents in the liquid paraffin. Finally, the slope of the temperature-time curves sees an important variation, and in particular a decrease, related to the starting of the melting process, as it is very well-known from the previous studies in thermodynamics, where the curve became horizontal, having the isothermal condition during the phase change. In this case this is not happening since each instant of time there is the phase change and the overheating of the already melted paraffin. Furthermore, it is better to consider a melting temperature range rather than a punctual melting temperature. In conclusion, it is important to remember how the change in the slopes of the curves is always related to the type of heat exchange. Since in the study there is a first phase with a sensible heat exchange, followed by a latent one, and finally going back to a sensible one once the total melting is achieved, this behaviour is expected and recognized.

3.2.1 Presentation of the results related to the lattice geometry

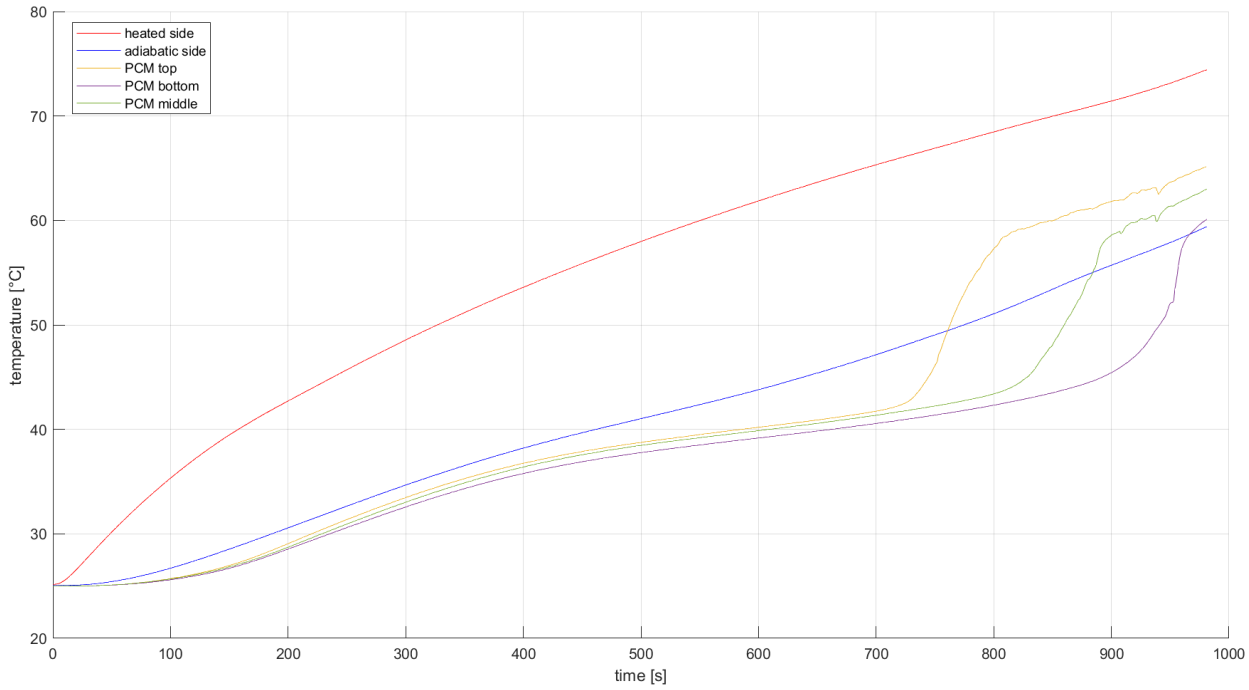

Figure 3.1 – Profile of temperatures for the different sides, obtained with the presented thermocouples, RT42, 100 W

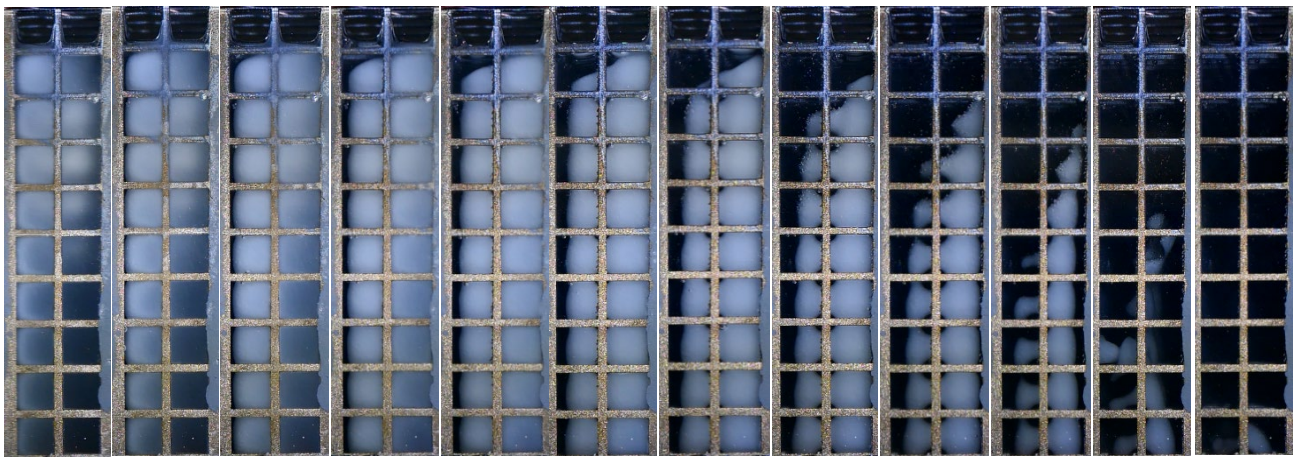

Figure 3.2 – Melting profile, paraffin RT42, 100 W

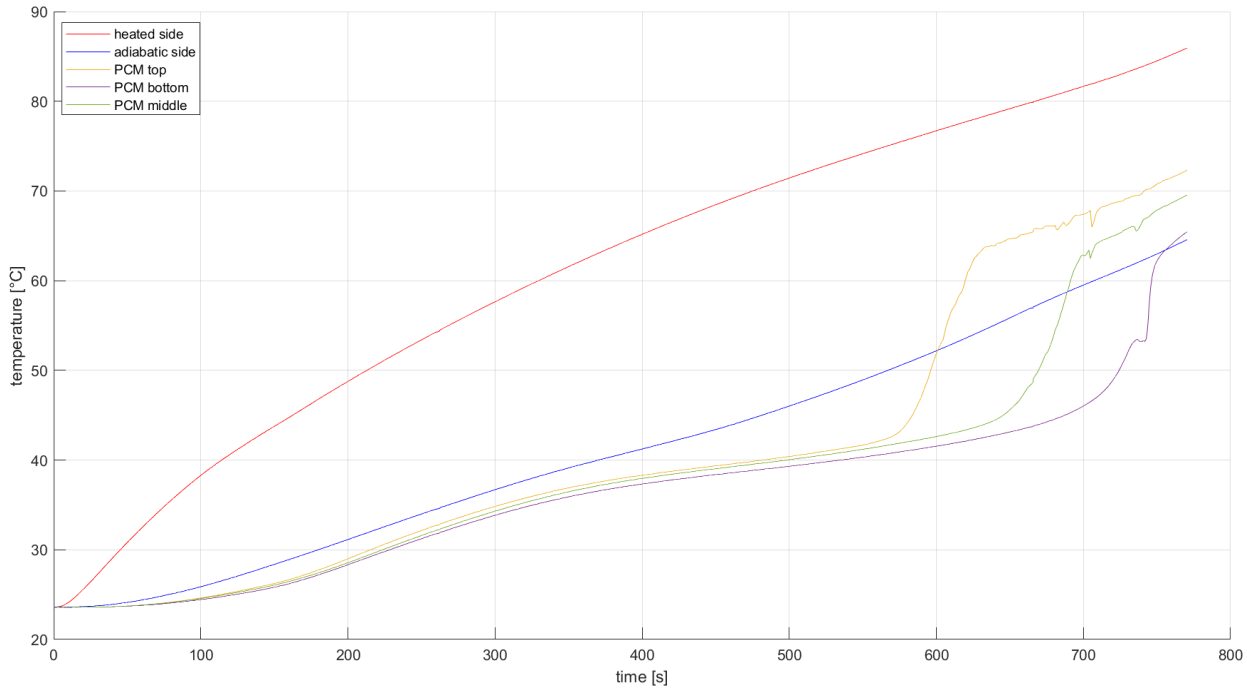

Figure 3.3 – Profile of temperatures for the different sides, obtained with the presented thermocouples, RT42, 150 W

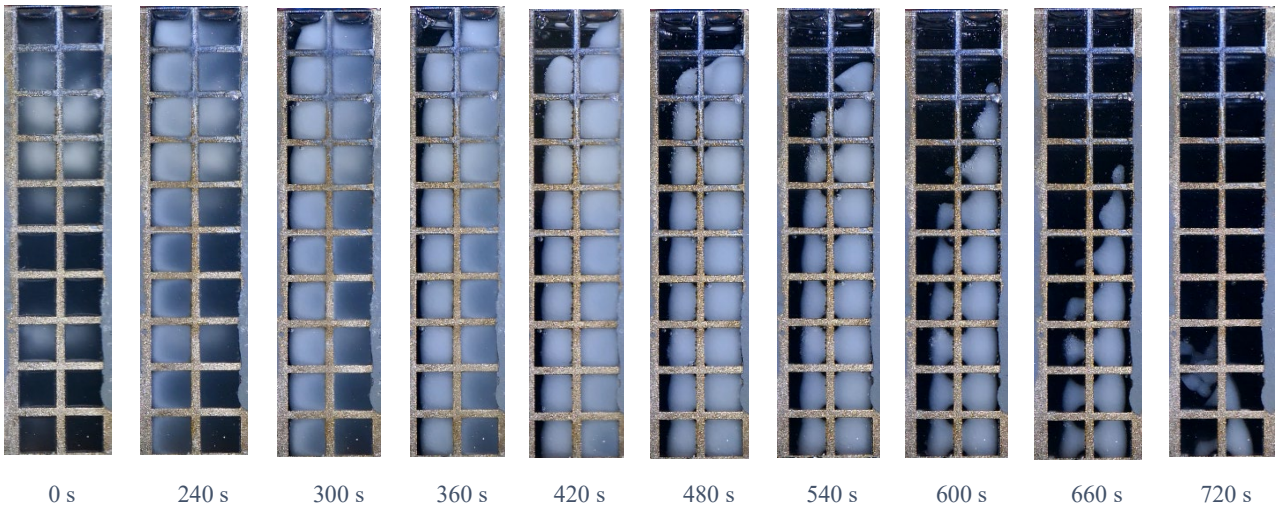

Figure 3.4 – Melting profile, paraffin RT42, 150 W

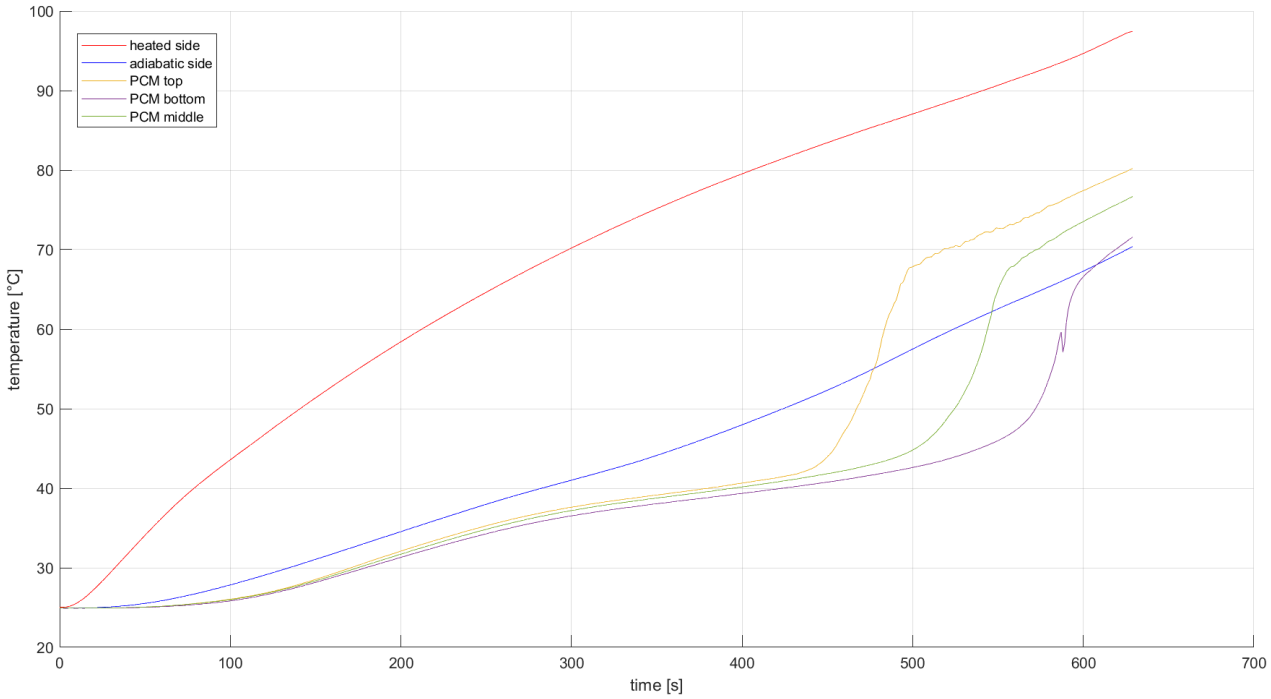

Figure 3.5 – Profile of temperatures for the different sides, obtained with the presented thermocouples, RT42, 200 W

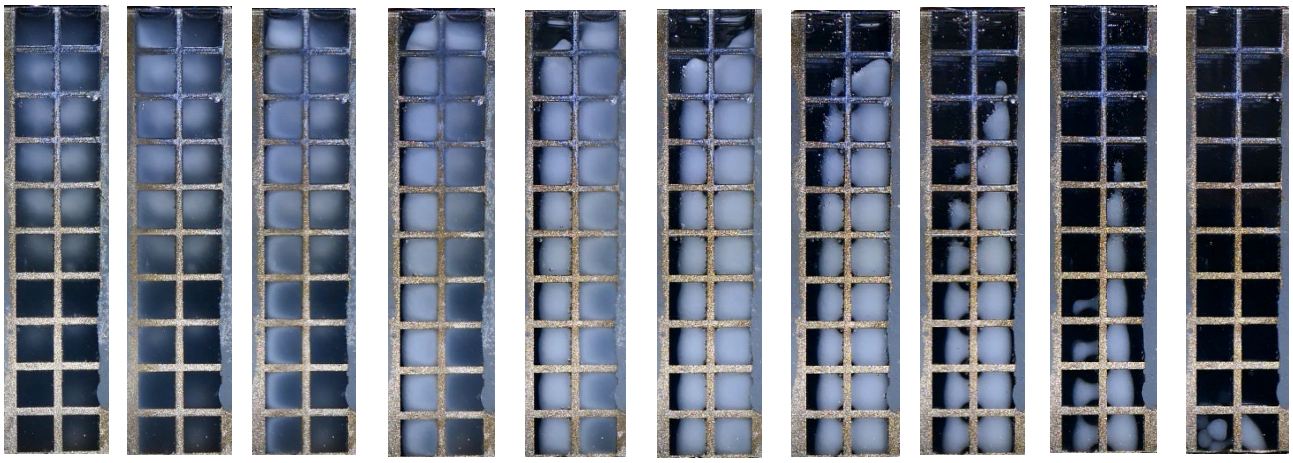

Figure 3.6 – Melting profile, paraffin RT42, 200 W

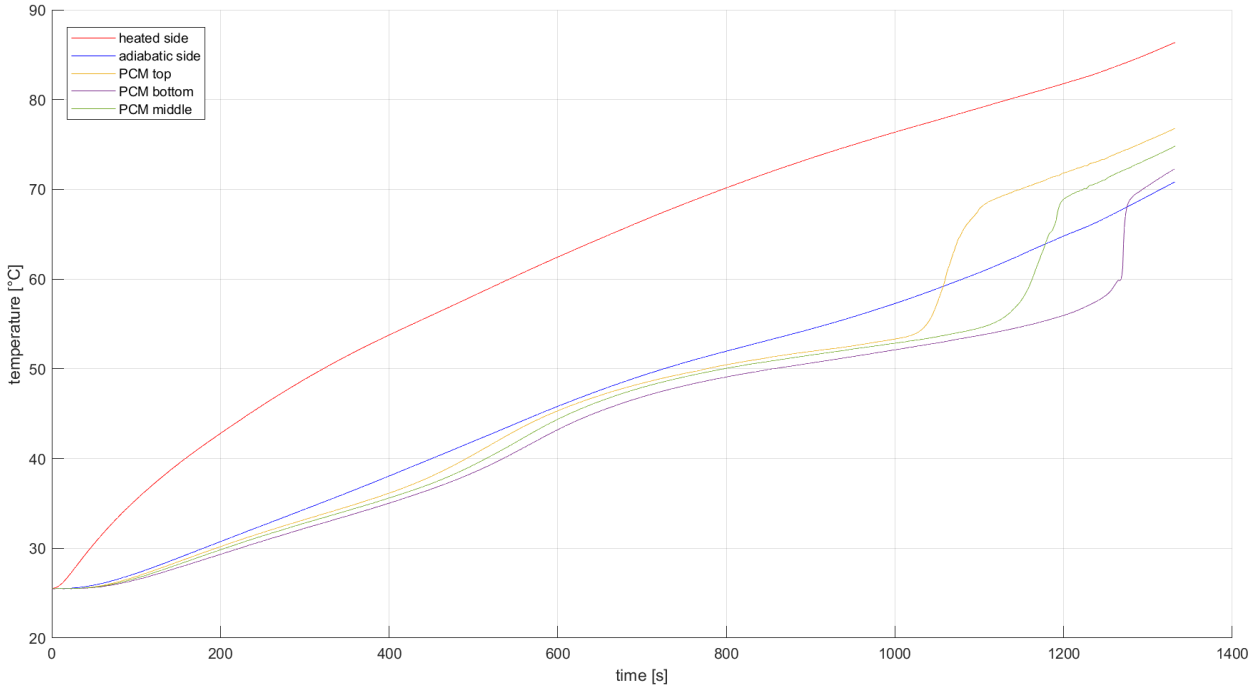

Figure 3.7 – Profile of temperatures for the different sides, obtained with the presented thermocouples, RT55, 100 W

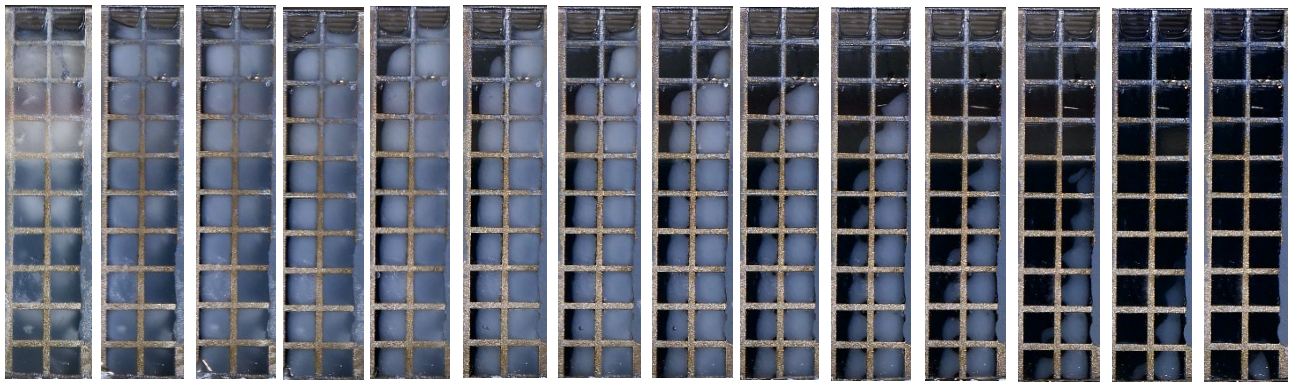

Figure 3.8 – Melting profile, paraffin RT55, 100 W

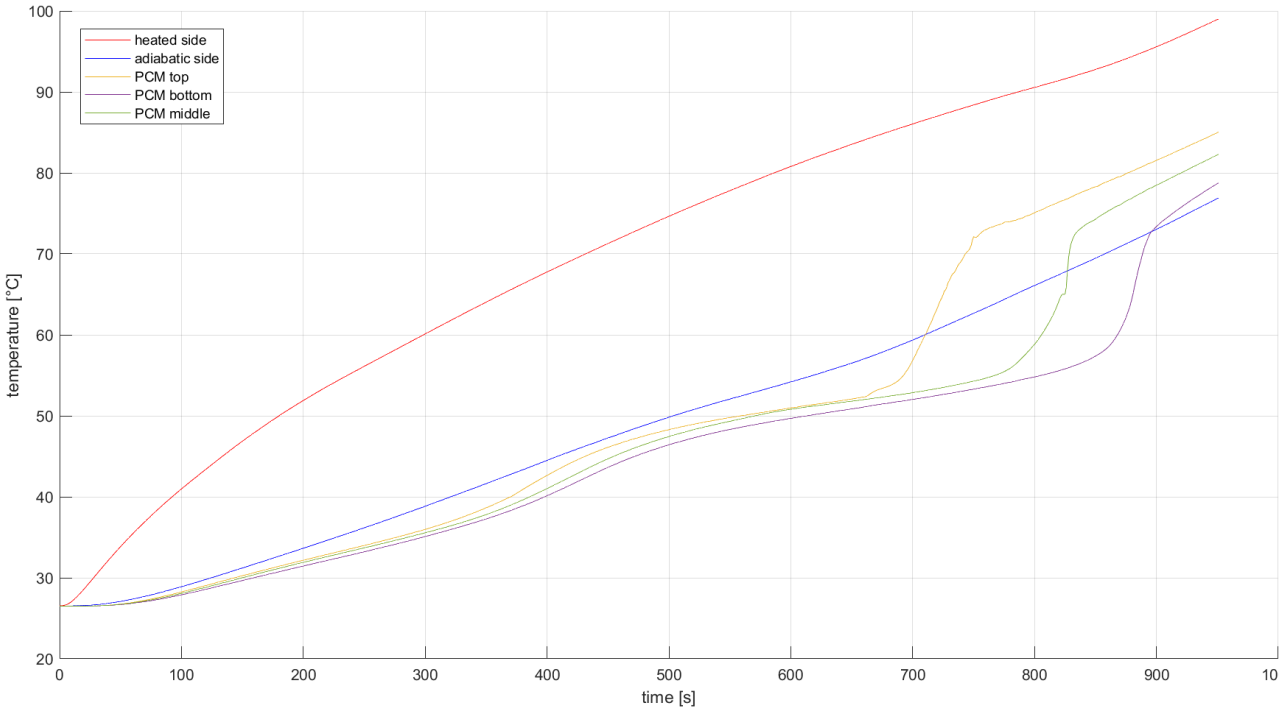

Figure 3.9 – Profile of temperatures for the different sides, obtained with the presented thermocouples, RT55, 150 W

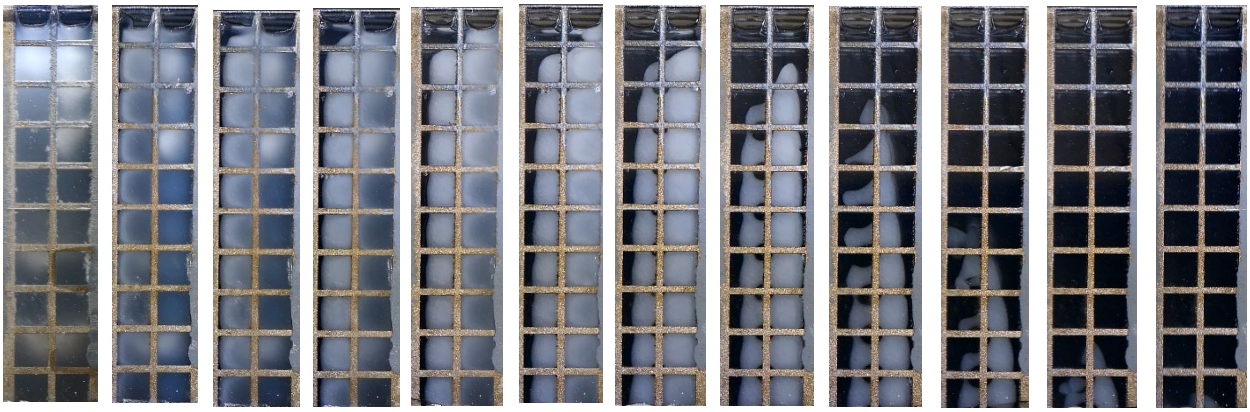

Figure 3.10 – Melting profile, paraffin RT55, 150 W

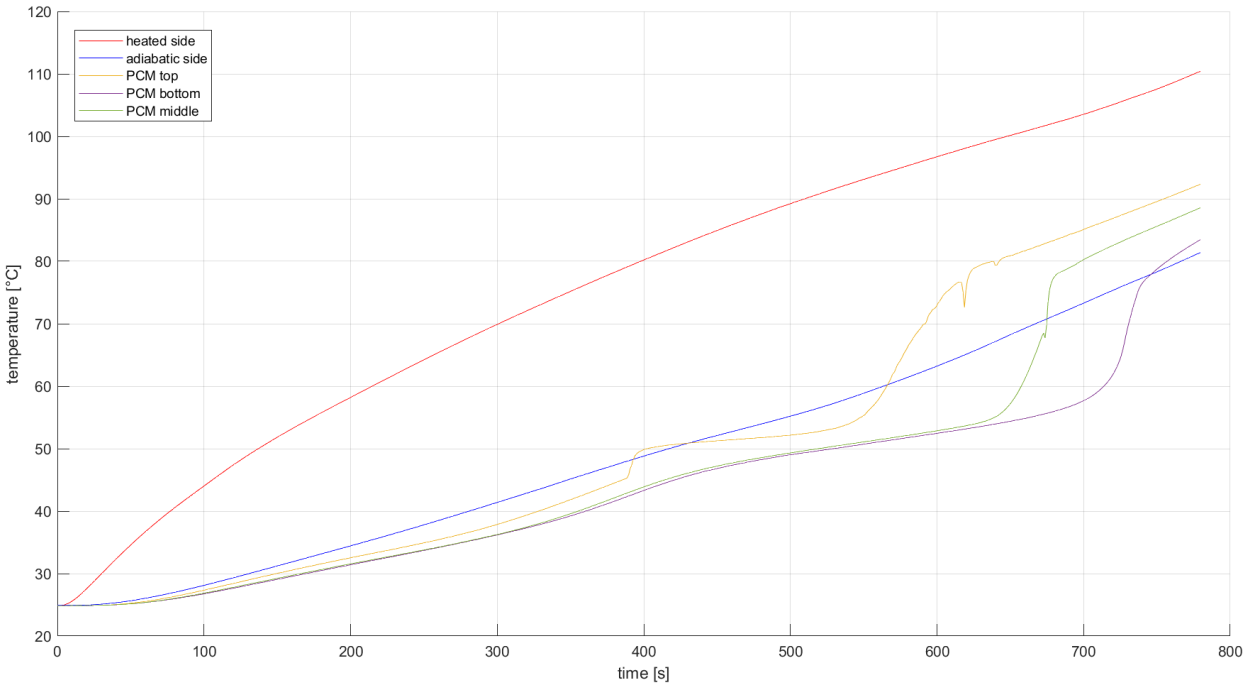

Figure 3.11 – Profile of temperatures for the different sides, obtained with the presented thermocouples, RT55, 200 W

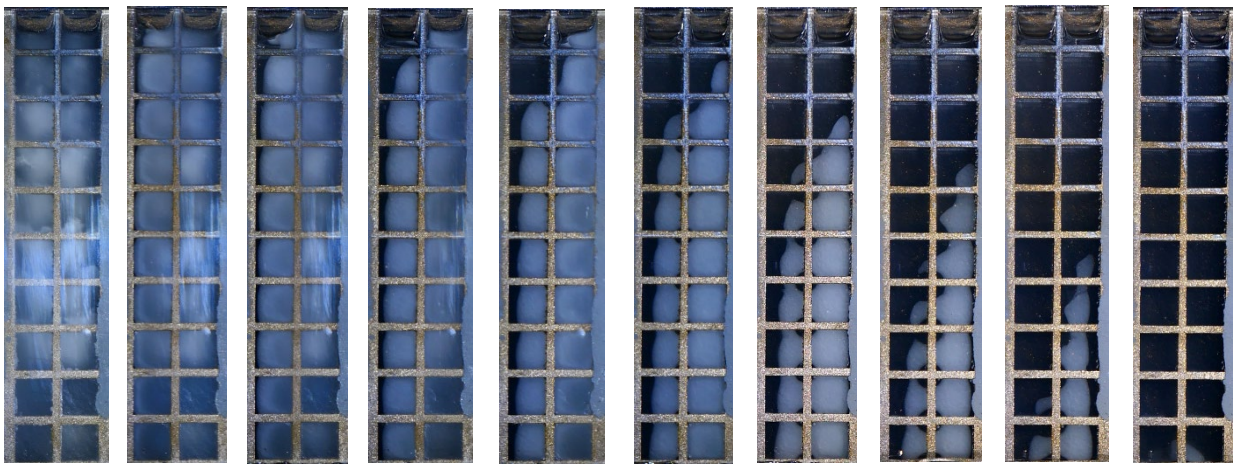

Figure 3.12 – Melting profile, paraffin RT55, 200 W

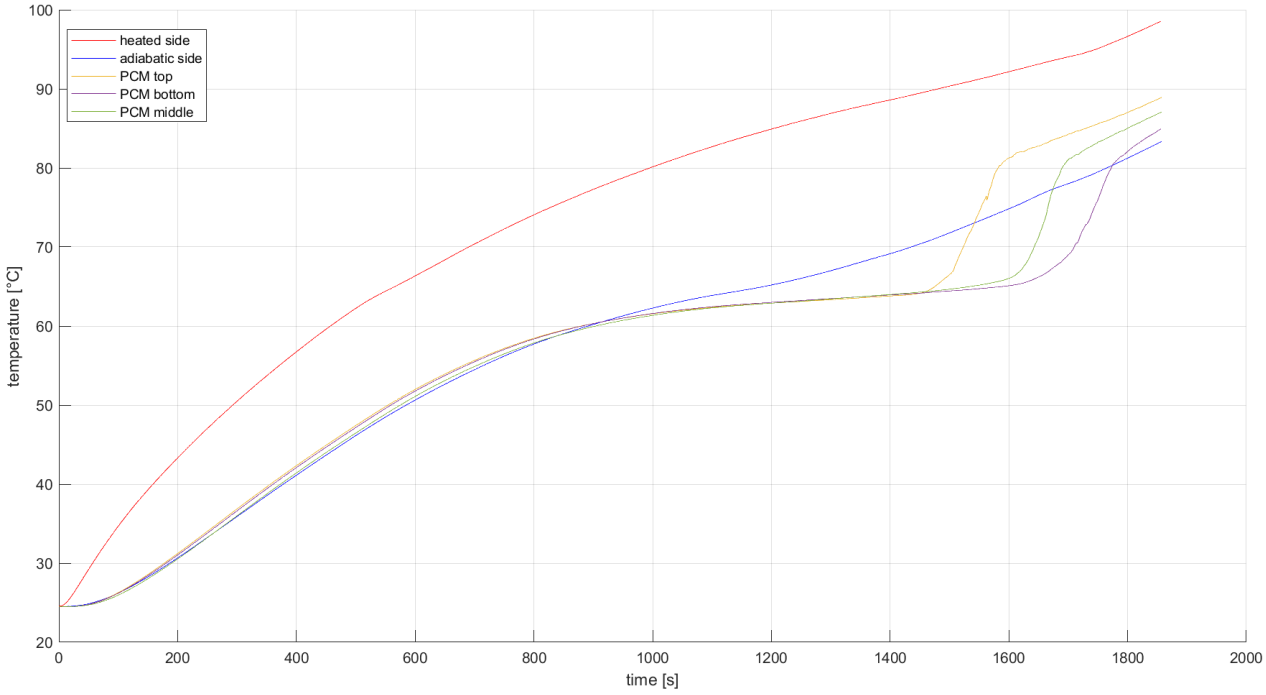

Figure 3.13 – Profile of temperatures for the different sides, obtained with the presented thermocouples, RT64HC, 100 W

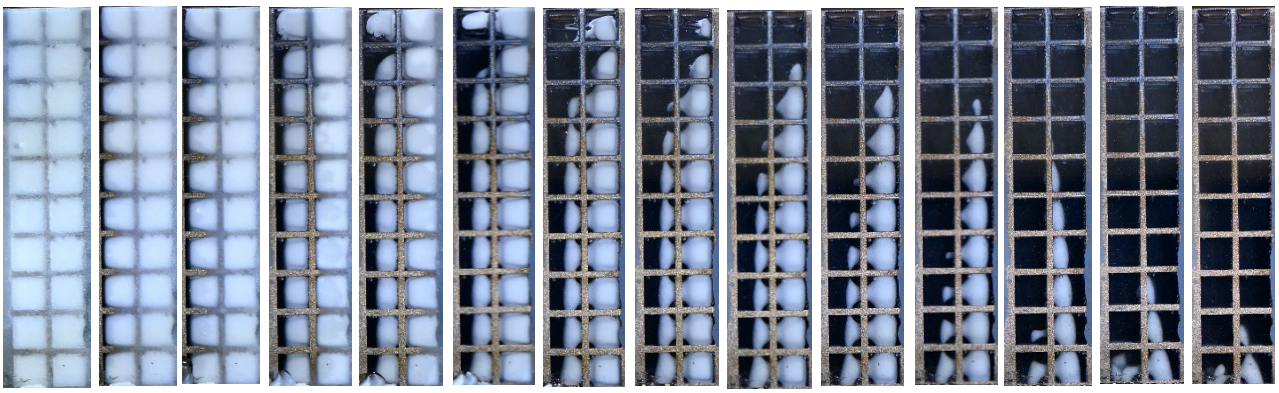

Figure 3.14 – Melting profile, paraffin RT64HC, 100 W

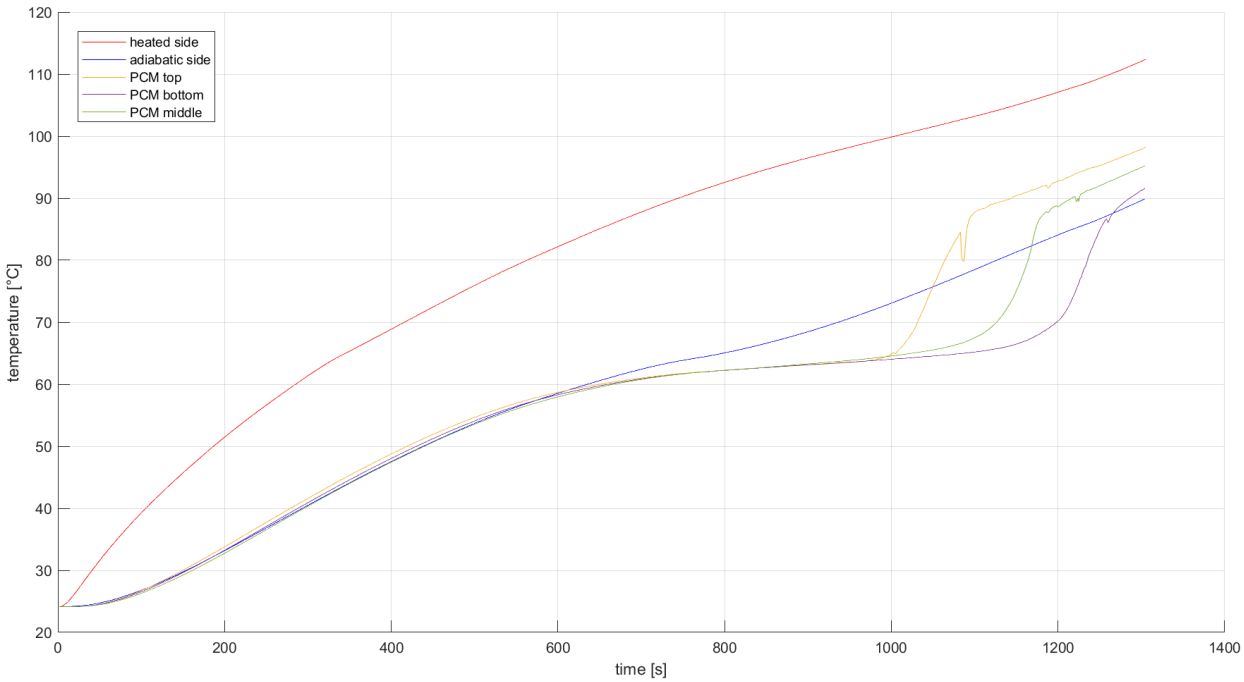

Figure 3.15 – Profile of temperatures for the different sides, obtained with the presented thermocouples, RT64HC, 150 W

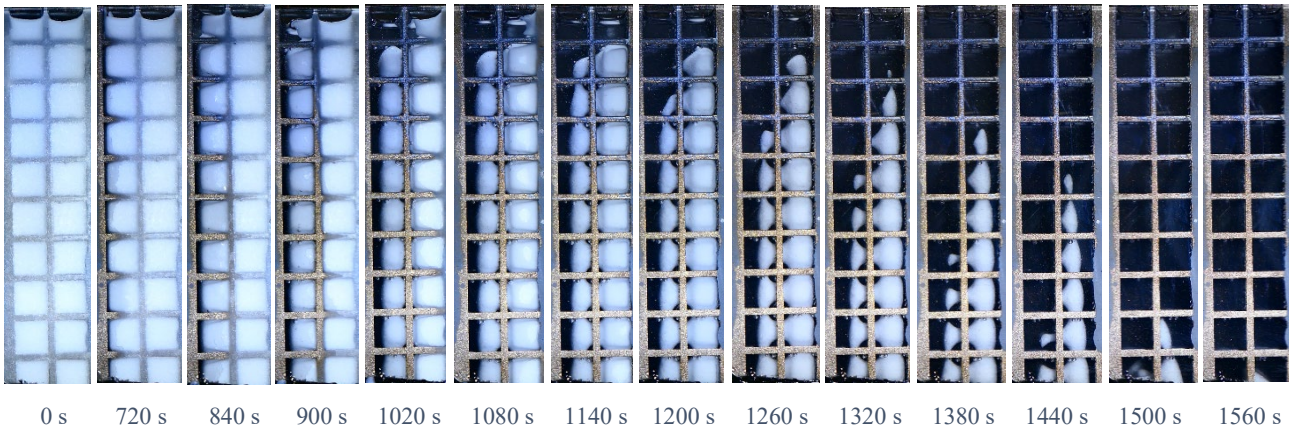

Figure 3.16 – Melting profile, paraffin RT64HC, 150 W

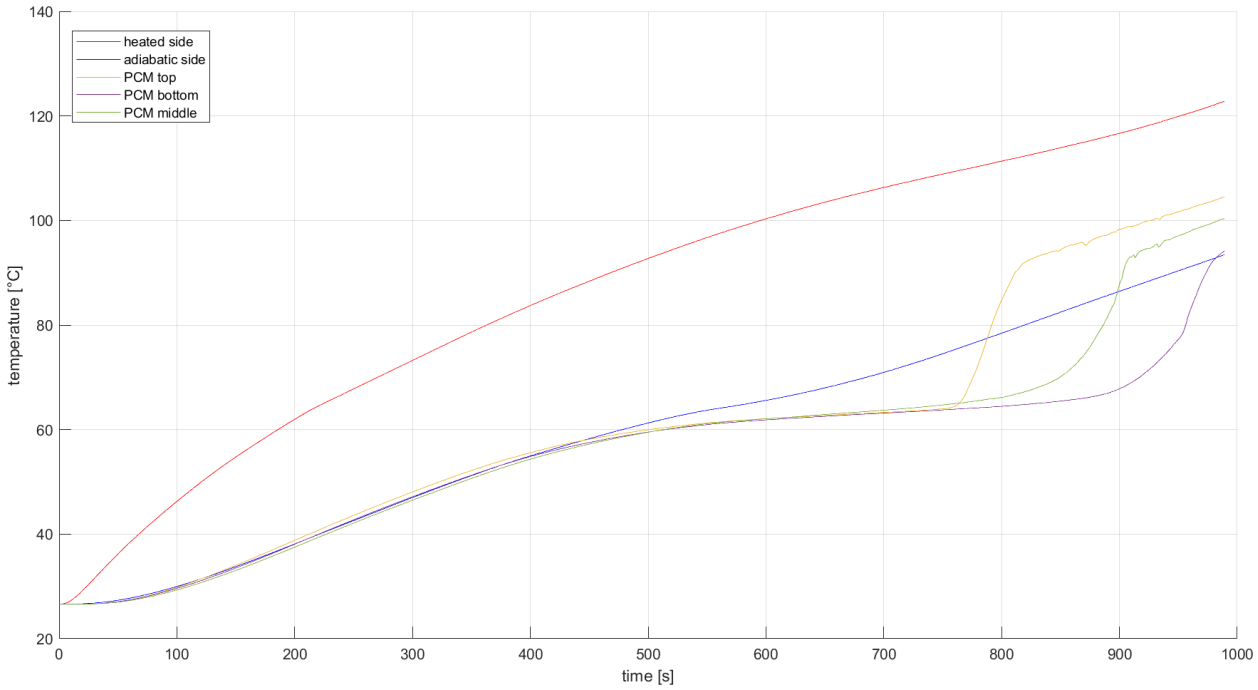

Figure 3.17 – Profile of temperatures for the different sides, obtained with the presented thermocouples, RT64HC, 200 W

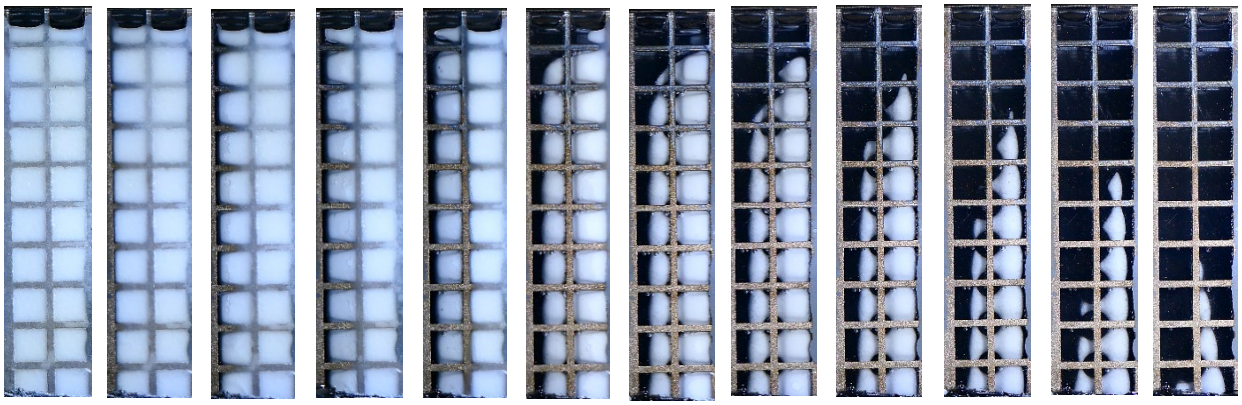

Figure 3.18 – Melting profile, paraffin RT64HC, 200 W

An overall display of the result is reported in *Table 3.1*, *Table 3.2,* and *Table 3.3*.

RT42	Power [W]	Time [s]	Temperature [°C]
	100	977	74.26
	150	767	85.65
	200	621	96.78

Table 3.1 – Results for RT42, obtained from tests for the lattice (10 mm, 93% porosity) structure

RT55	Power [W]	Time [s]	Temperature [°C]
	100	1327	86.15
	150	947	98.73
	200	776	110.03

Table 3.2 – Results for RT55, obtained from tests for the lattice (10 mm, 93% porosity) structure

RT64HC	Power [W]	Time [s]	Temperature [°C]
	100	1853	98.44
	150	1302	112.2
	200	985	122.51

Table 3.3 – Results for RT64HC, obtained from tests for the lattice (10 mm, 93% porosity) structure

3.3 Comparisons

In this paragraph some considerations that are visible and obtained from the tests done on the given geometry are reported. First of all, a comparison between the different paraffin, in terms of melting time and final temperature reached on the heated side (*Paragraph 3.3.1*) is performed. Secondly, a comparison between different thermal powers applied (*Paragraph 3.3.2*) is proposed. Finally, the last analysis done is related to the current geometry and the data obtained in previous experiments with different geometries, both lattice and BCC (*Paragraph 3.3.3*).

3.3.1 Comparison between different paraffin

Considering the different paraffin used and the same heat flux applied, it is possible to highlight how the paraffin RT42 starts before the others two the melting process, followed by the RT55 and finally from the RT64HC. Focusing on the temperature, it is possible to notice how, increasing the melting temperature, also the final temperature increases. On the other side, lower melting temperature means lower melting time. At the end of the phase change process, the slope of the curve increases again. The final considerations that can be done are related to times and temperatures. In particular, on one side, if the application that needs to be developed requires cooling for short intervals of time, the RT42 paraffin should be chosen. On the other side, with a greater absorption of heat, with long time interval and higher temperatures reached, the choice should fall on the paraffin RT64HC. In all the other cases, the RT55 should be taken into account.

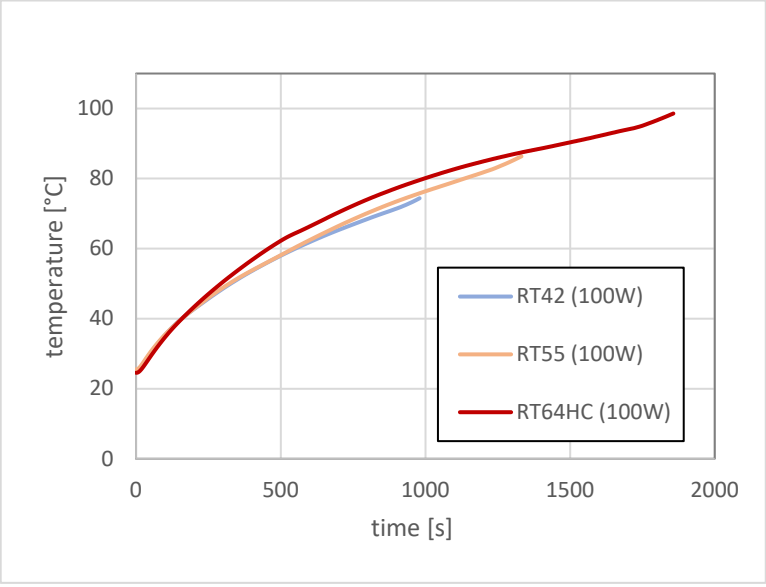

Figure 3.19 – Profile of temperatures for the heated side, obtained for the same value of heat flow rate (100 W)

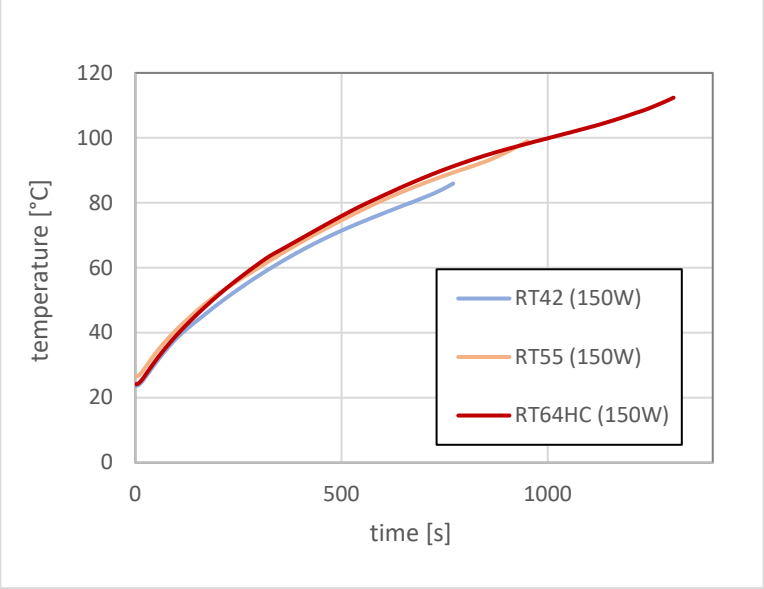

Figure 3.20 – Profile of temperatures for the heated side, obtained for the same value of heat flow rate (150 W)

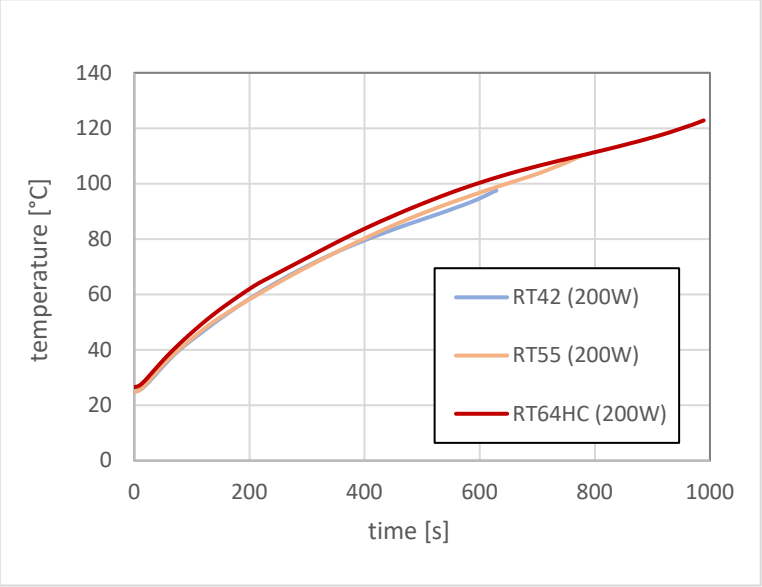

Figure 3.21 – Profile of temperatures for the heated side, obtained for the same value of heat flow rate (200 W)

3.3.2 Comparison between different heat flow rates applied

The three different applied heat flow rates were 100, 150, 200 W respectively, considering the same type of module and the same paraffin. Increasing the thermal power and subsequently the heat flux, the slope of the curve of temperature, in particular on the side of interest, the heated one, increases. This is due to the fact that the temperature on that side is directly proportional to the applied heat flux. As a consequence, having a greater heat flux means having a more rapid change in the slope: this led to an early process of melting, as well as to a shorter time interval for it.

In conclusion, the overall time for the test is sensibly reduced, as it is possible to see in each table reported in the previous page.

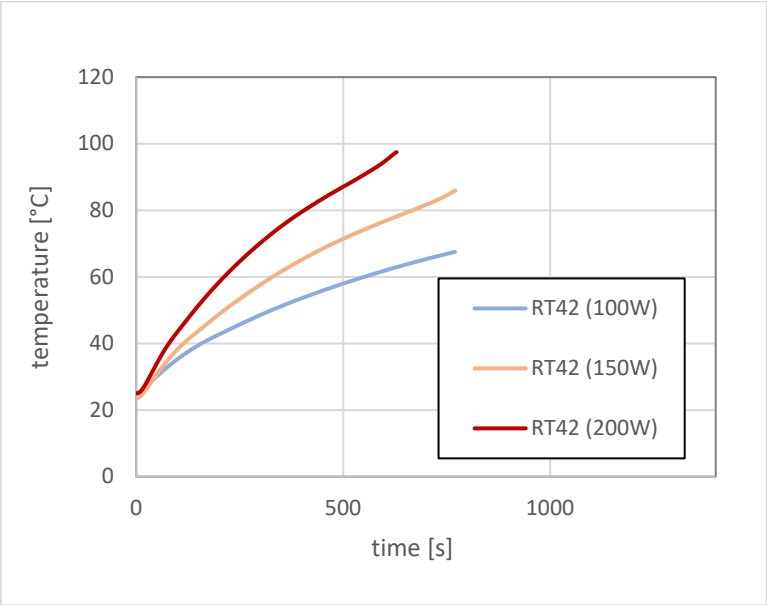

Figure 3.22 – Profile of temperatures for the heated side, obtained for the same paraffin (RT42)

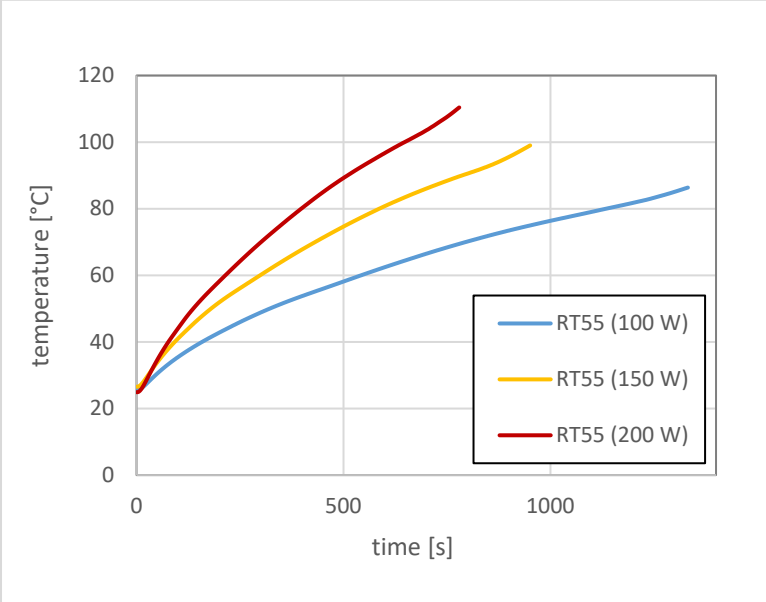

Figure 3.22 – Profile of temperatures for the heated side, obtained for the same paraffin (RT55)

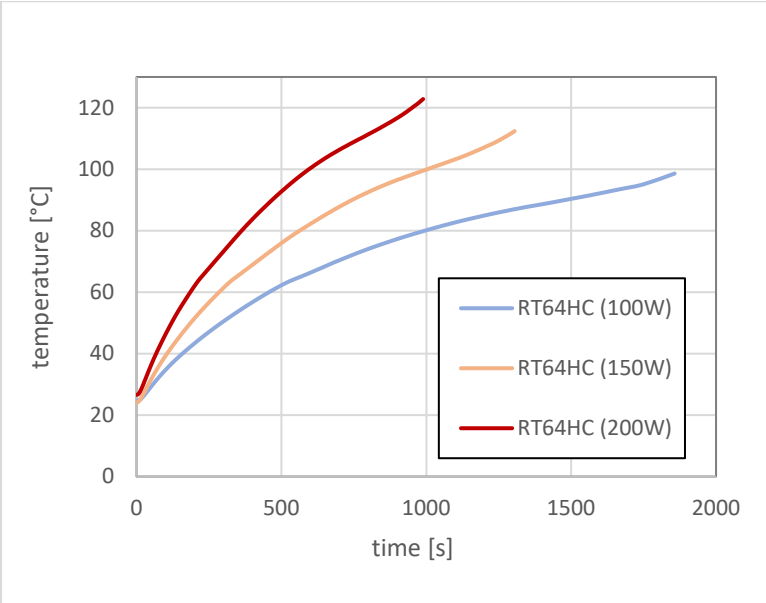

Figure 3.23 – Profile of temperatures for the heated side, obtained for the same paraffin (RT64HC)

3.3.3 Comparison between the case study and previously studied structures

In order to better appreciate this comparison, *Table 3.4*, *3.5, 3.6* and *Table 3.7, 3.8* report the overall experimental results obtained in previous studies, with the analysis of five different structures, with porosity either 87% or 93%, varying from lattice to BCC ones.

Lat10-87	RT42	Power [W]	Time [s]	Temperature [°C]
		100	1050	67.76
		150	819	77.74
		200	659	85.91

	RT55	Power [W]	Time [s]	Temperature [°C]
		100	1395	78.55
		150	978	87.97
		200	755	98.25

	RT64HC	Power [W]	Time [s]	Temperature [°C]
		100	1925	96.27
		150	1301	107.25
		200	991	116.32

Table 3.4 - Results obtained from tests for the lattice (10 mm, 87% porosity) structure

Lat5-87	RT42	Power [W]	Time [s]	Temperature [°C]
		100	920	62.21
		150	648	68.76
		200	/	/

	RT55	Power [W]	Time [s]	Temperature [°C]
		100	1101	71.77
		150	758	80.08
		200	599	86.09

	RT64HC	Power [W]	Time [s]	Temperature [°C]
		100	1518	84.82
		150	1011	92.31
		200	780	98.74

Table 3.5- Results obtained from tests for the lattice (5 mm, 87% porosity) structure

Lat5-93	RT42	Power [W]	Time [s]	Temperature [°C]
		100	784	65.18
		150	593	74.27
		200	479	81.04

	RT55	Power [W]	Time [s]	Temperature [°C]
		100	1144	77.66
		150	794	86.26
		200	636	95.15

	RT64HC	Power [W]	Time [s]	Temperature [°C]
		100	1636	89.44
		150	1096	100.78
		200	841	109.66

Table 3.6 - Results obtained from tests for the lattice (5 mm, 93% porosity) structure

Starting from the analysis of the lattice structures, it is possible to notice different things. Firstly, passing from a 10 mm unitary cell side to a 5 mm one, the melting time, as well as the final temperature on the heated side are reduced. The cause is quite clear, since, having the same available volume to be occupied by the structure, the 5 mm side unitary cells are double then the others: in this way, even with the same amount of aluminum, the value of a_{sv}, ratio between the surface and the volume of the structure [m^{-1}], varies. Secondly, taking into account the different porosities, 87% and 93% respectively, but considering the same unitary cell dimension, despite the slightly greater melting time required from the first type of structures, the final temperature achieved varies more significantly, and in particular it is lower.

This allows to have a better management of the heat exchange, since we have a double benefit in term of greater time to which the paraffin is subjected to the heat absorption and a lower final temperature of the component. Finally, it is possible to notice, focusing on the single geometry, how the behaviours described in the previous paragraph are still valid.

BCC10	RT42	Power [W]	Time [s]	Temperature [°C]
		100	890	63.10
		150	655	70.30
		200	523	76.00

	RT55	Power [W]	Time [s]	Temperature [°C]
		100	1289	75.00
		150	869	82.70
		200	691	89.90

	RT64HC	Power [W]	Time [s]	Temperature [°C]
		100	1615	86.10
		150	1111	93.00
		200	858	100.20

Table 3.7 - Results obtained from tests for the BCC (10 mm) structure

BCC5	RT42	Power [W]	Time [s]	Temperature [°C]
		100	833	56.82
		150	575	62.18
		200	441	66.86
	RT55	Power [W]	Time [s]	Temperature [°C]
		100	1107	67.85
		150	749	73.37
		200	578	78.38
	RT64HC	Power [W]	Time [s]	Temperature [°C]
		100	1434	77.30
		150	936	82.80
		200	713	88.31

Table 3.8 – Results obtained from tests for the BCC (5 mm) structure

In the comparison with the body-centred-cubic structures, the behaviour is the same from one case to another: it is possible to highlight a lower melting time and melting temperature reached.

CHAPTER 4 – Simulations in ANSYS Fluent

4.1 Assumptions

The numerical simulations were performed by using the software ANSYS Fluent 2021. In the previous chapter, with the presentation of the different experimental tests, it was possible to notice how the melting front proceeded almost parallel from the heated side to the adiabatic one. This behaviour has to be charged to the lattice of aluminum, since the possibility of movement of the liquid phase was limited, and as a consequence the natural convection. In this way the efficiency of the heat transfer is restricted. It needs to be remembered how the thermal conductivity of the aluminum is almost three orders of magnitude greater than the one of the considered paraffin. In addition, as it is possible to notice from the temperature curves provided by the three thermocouples inserted at 25, 50 and 75 mm of height into the PCM, the vertical gradient is negligible. However, this phenomenon can be better observed in the experiments conducted by Diani and Campanale [1], into a test module without the metallic structure inside. Once this problem was addressed and analysed, the following simplifications were introduced:

- Constant density of the paraffin
- Constant melting temperature
- Neglected radiant heat exchange
- Analysis of a vertical section, having 10 mm thickness (100×40×10)

The last consideration lead to the analysis of the given geometry as a symmetric model, even if the test module does not reflect this peculiarity. In fact, in reality, there is the presence of the frontal glass side, while the back side of the structure is insulated with 15 mm of Bakelite and Teflon each. Since the computation in this case was done taking into account only a row of cells out of the ten composing the assemble, the heat transfers in those two surfaces were neglected.
The characteristics of each material are listed in *Table 4.1*.

	Density [kg m^{-3}]	Specific heat capacity [kJ kg^{-1} K^{-1}]	Thermal conductivity [W m^{-1} K^{-1}]
Copper	8900	371	390
Aluminum	2670	900	175
Teflon	2200	970	0.35
Ni-Cr	8300	450	11.3

Table 4.1 – Properties of the materials present in the test module

The case presented is not a steady-state one, but a transient problem. For this reason, it is needed to be solved differential equations:

$$\frac{\partial}{\partial t}(\rho H) = \nabla(k\Delta T) + S \tag{4.1}$$

given:

$$H = h + \Delta H \tag{4.2}$$

Where h is the specific enthalpy, while ΔH is the term accounting for the latent heat. Furthermore, the term appearing in the equation (4.1) S accounts for the internal heat gains, in order to describe the copper heating. Clearly, it is not possible to solve analytically these equations: for this reason, two different discretizations are done, one in space, the other in time.

- Discretization in space: it is the operation done in the "mesh" section of ANSYS Fluent and correspond to the meshing operation. A subdivision into finite dimension little volumes is imposed to the drawn geometry. Decreasing the size of those elements it increases the final accuracy of the model, due to the fact that a continuous geometry, made by an infinite number of points, is gradually represented in a finer way.
  However, on the other hand, the time needed to execute calculations is increasing as the model became more and more fine.

- Discretization in time: it is the interval of time in which the differential equations are applied.

  The considerations done for the discretization in space are still valid.

The number of elements composing the mesh was chosen in order to be able to work also when not in laboratory, since the student version does not allow to set the wanted number of elements. The value is set equal to 73880, corresponding to an "Element Size", in the "Body Sizing" section, at 0.5 mm. These digits were selected after different simulations, in order to be sure that the mesh was representing faithfully the analysed geometry. From the point of view of the discretization in time, the parameter to be fixed was the "time-step": after trying with 5, 10 and 20 seconds intervals respectively, the choice was for the 5 seconds one, even if the overall results were pretty close one to the others. The time for the calculations was quite important since the lowest value was chosen. On the other side, if the 20 seconds time-step had been selected, the shape of the curves would have become edgy. The iterations done by the software are done in between two time-steps, and the maximum value of them can be selected: in this case the proper number was 20 s since after this value, the deviation from the convergence value was no more diminishing. In order to consider properly the convection phenomena, due to the contact with the external air, the heat transfer coefficient inserted was 20 W m^{-2} K^{-1}.

All these assumptions were done in order to obtain an acceptable burden of calculations in ANSYS Fluent. This is a fair compromise between a very detailed and precise mesh representing the real geometry and physical model accounting for the real conditions in the environment, and an acceptable time for the numerous simulations that were done along this study.

For the sake of completeness, it is important to remember how these hypotheses are totally subjective, in literature it is possible to find, as reported in [21], for example, choices of lower time-step, 2 and 3 seconds respectively.

4.2 Lattice structure analysis

In this paragraph there will be reported the applied previous assumptions in order to have a proper representation of the evolution in time and space of the melting front along the overall process. The aim was to validate the simulations thanks to the experiments conducted in the laboratory and guarantee the fairness of the results: for this reason, the main focus will be on the curves of temperatures of the aluminum and PCM, always remembering how, once again due to the simplifications, the melting process will be represented in the simulations as an isothermal line. In particular, this fact is related to the choice of imposing a constant density, and so the absence of expansion during the phase change and of the natural convection, and to the adoption of a fix temperature for the melting process, without a range of it between the solid and liquid phase respectively.

4.2.1 RT44

The following figures are reported:

- Temperature-time graph, for the heated side, experimental and simulation, as for example is shown in figure 4.1
- Temperature-time graph, in the middle of the section for the PCM, as for example is shown in figure 4.2

4.2.1.1 100 W

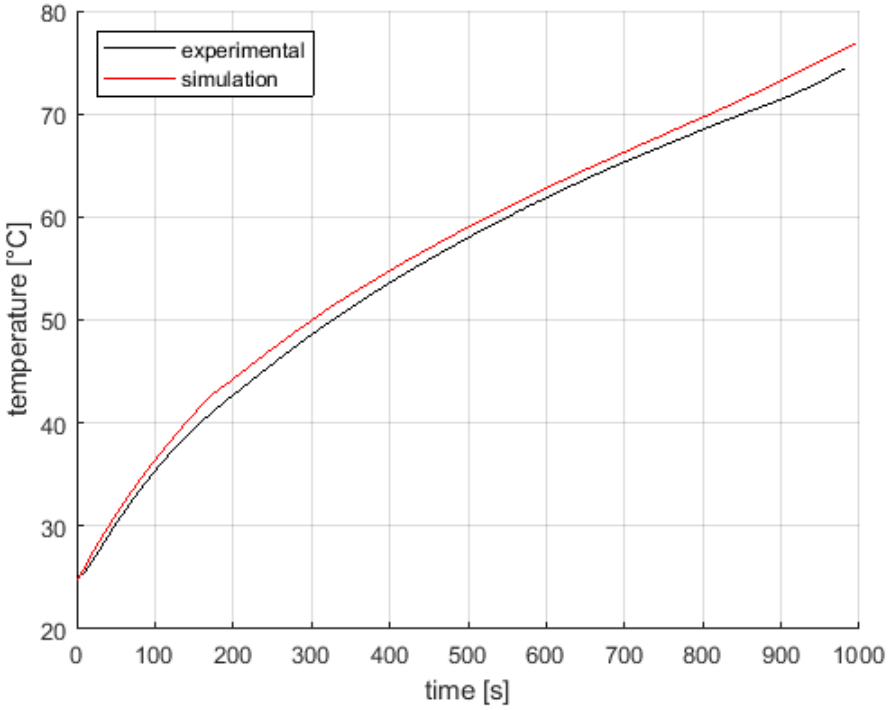

Figure 4.1 – Profile of the heated side of the structure (aluminum), RT42, 100 W

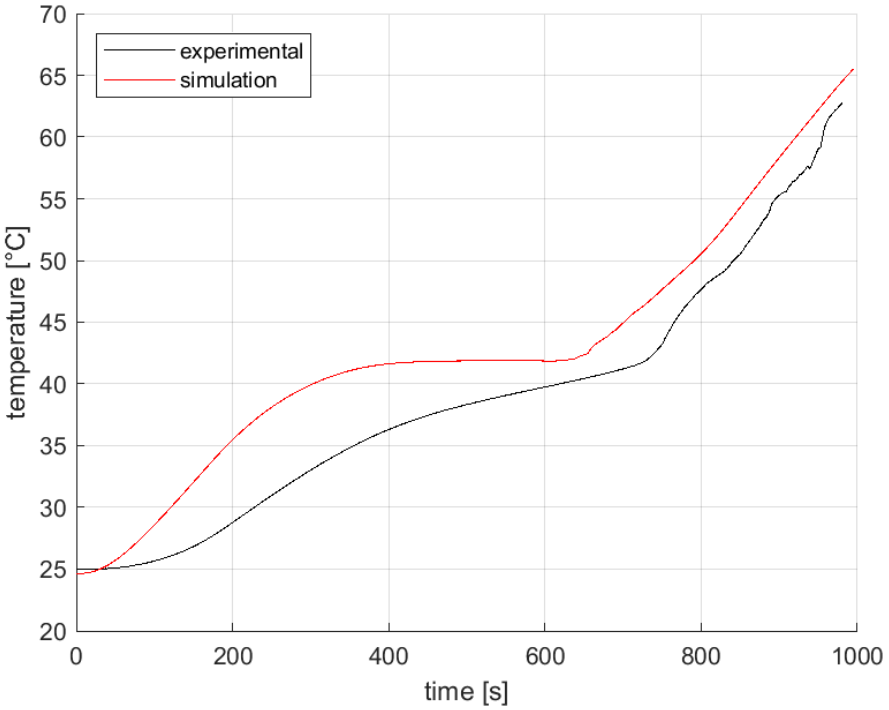

Figure 4.2 - Profile of the melting of the PCM, RT42, 100 W

4.2.1.2 150 W

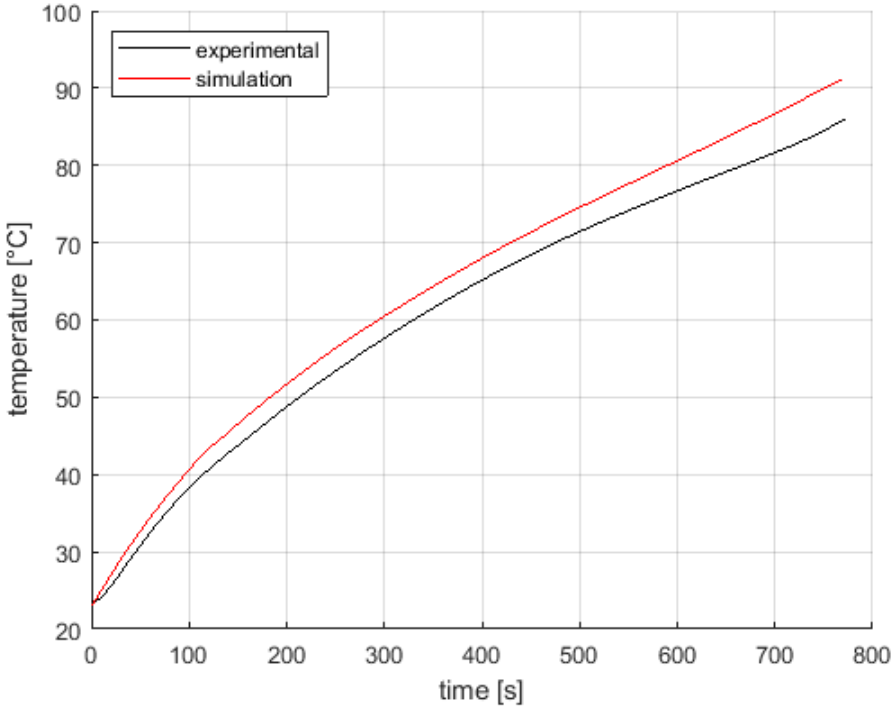

Figure 4.3 – Profile of the heated side of the structure (aluminum), RT42, 150 W

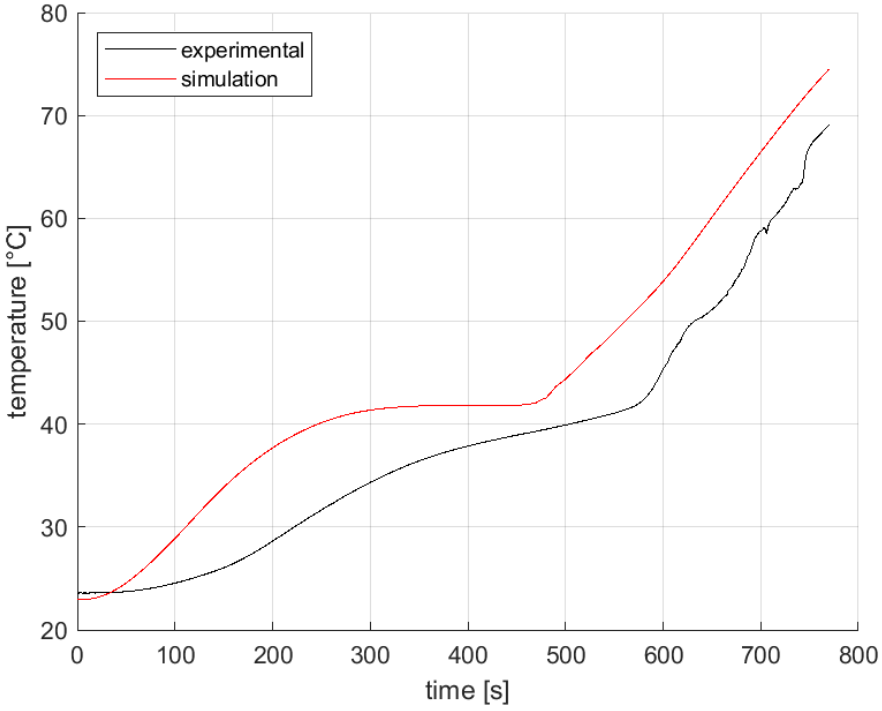

Figure 4.4 Profile of the melting of the PCM, RT42, 150 W

4.2.1.3 200 W

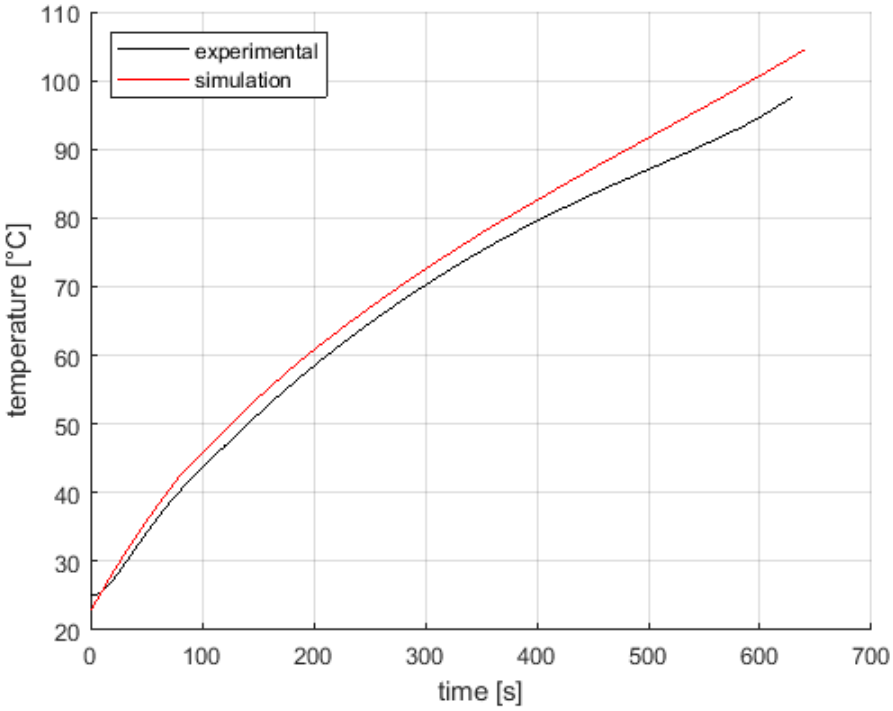

Figure 4.5 – Profile of the heated side of the structure (aluminum), RT42, 200 W

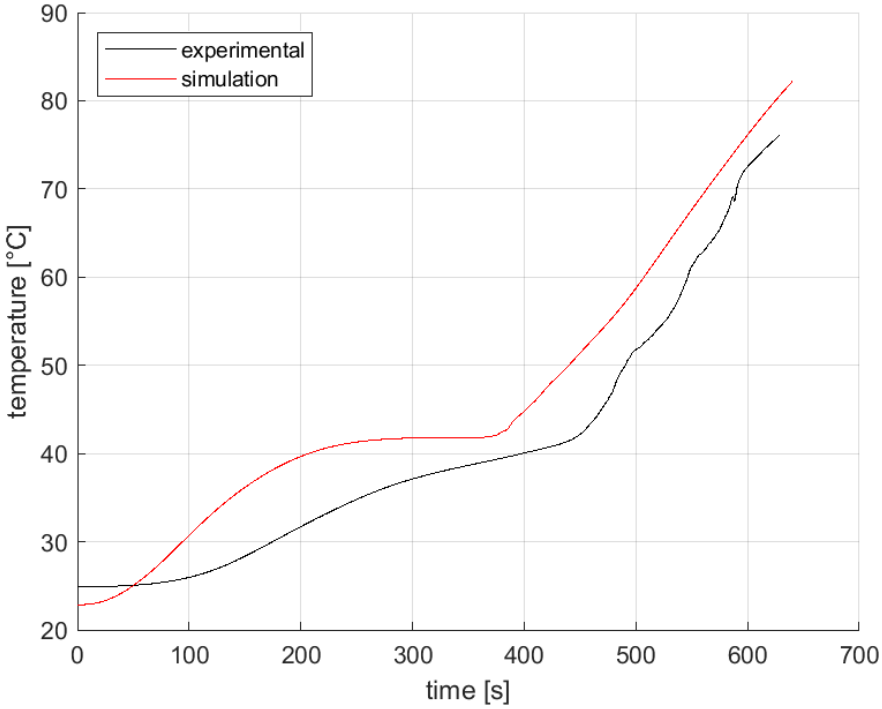

Figure 4.6 – Profile of the melting of the PCM, RT42, 200 W

4.2.2 RT55

The same graphs are reported for the other paraffin

4.2.2.1 100 W

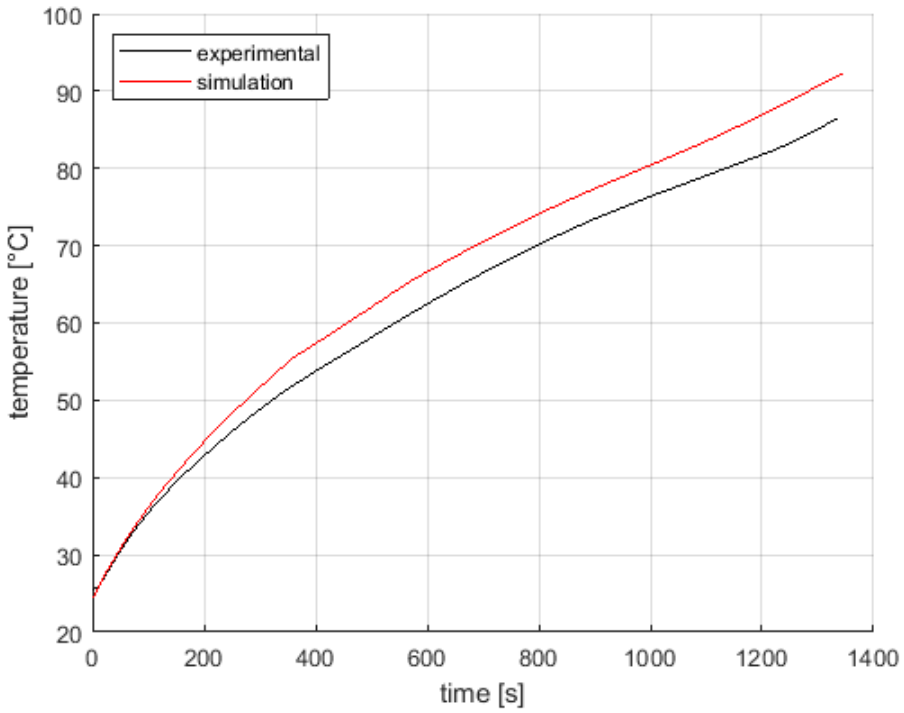

Figure 4.7 – Profile of the heated side of the structure (aluminum), RT55, 100 W

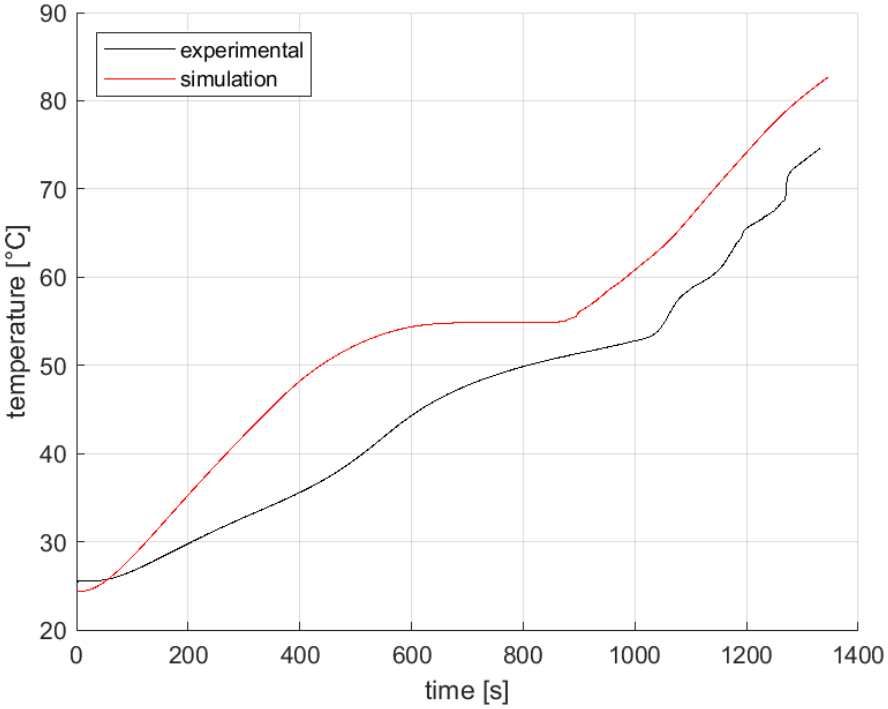

Figure 4.8 – Profile of the melting of the PCM, RT55, 100 W

4.2.2.2 150 W

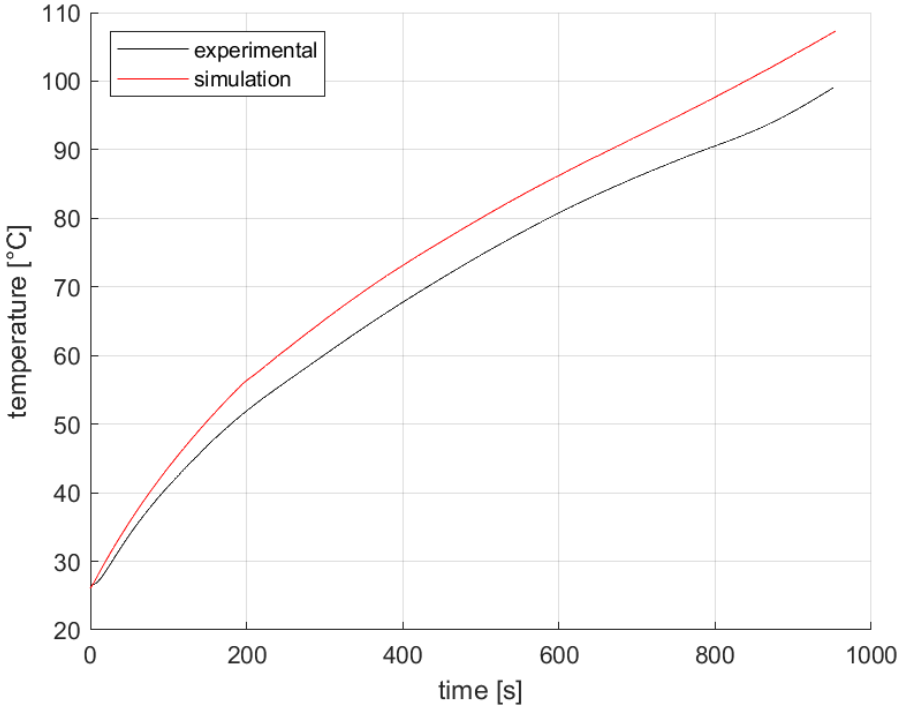

Figure 4.9 – Profile of the heated side of the structure (aluminum), RT55, 150 W

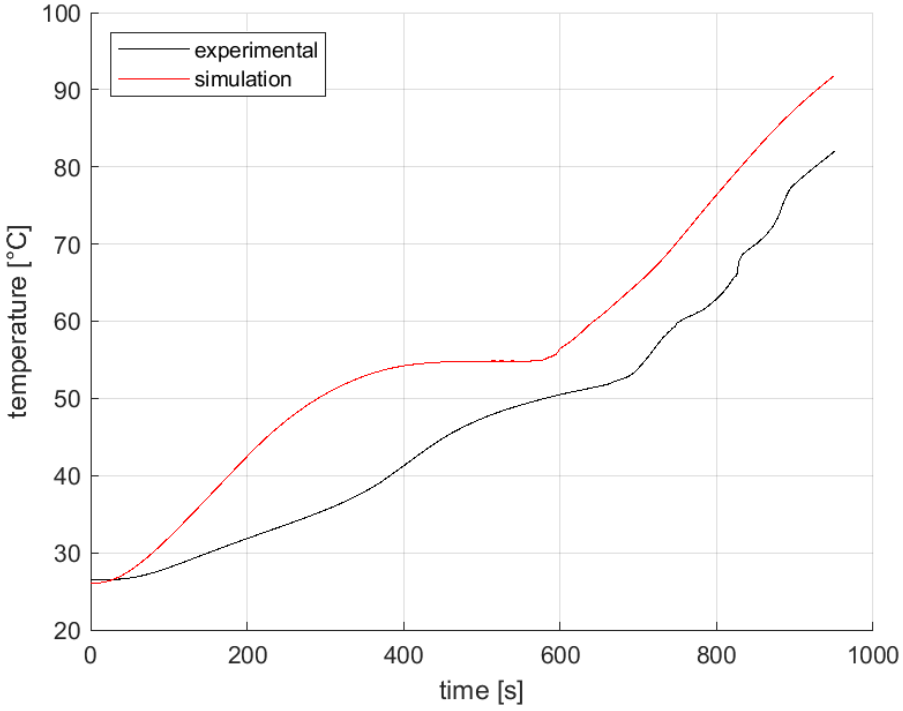

Figure 4.10 – Profile of the melting of the PCM, RT55, 150 W

4.2.2.3 200 W

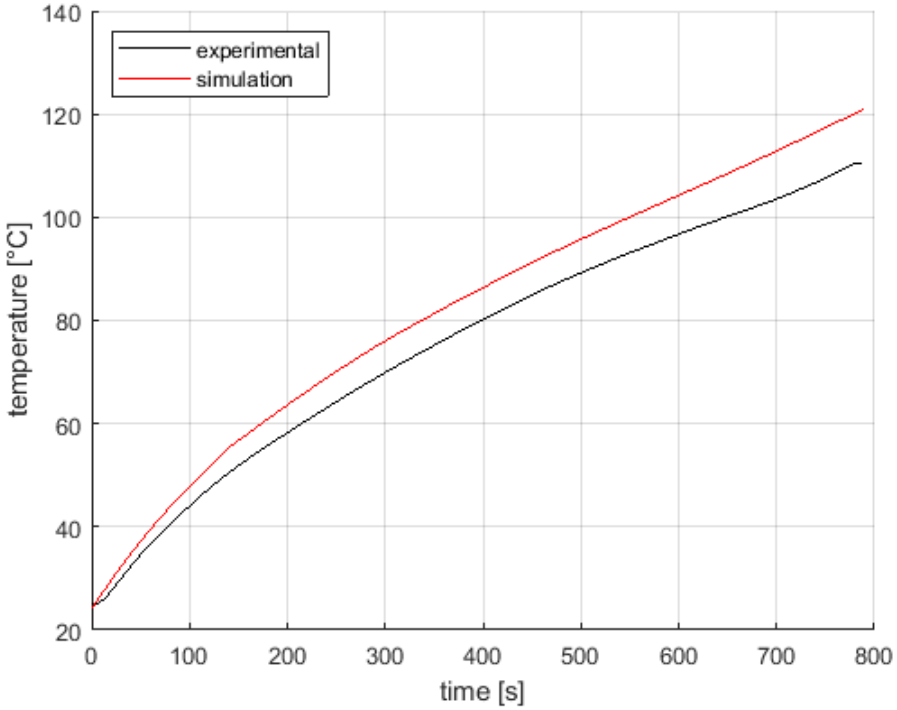

Figure 4.11 – Profile of the heated side of the structure (aluminum), RT55, 200 W

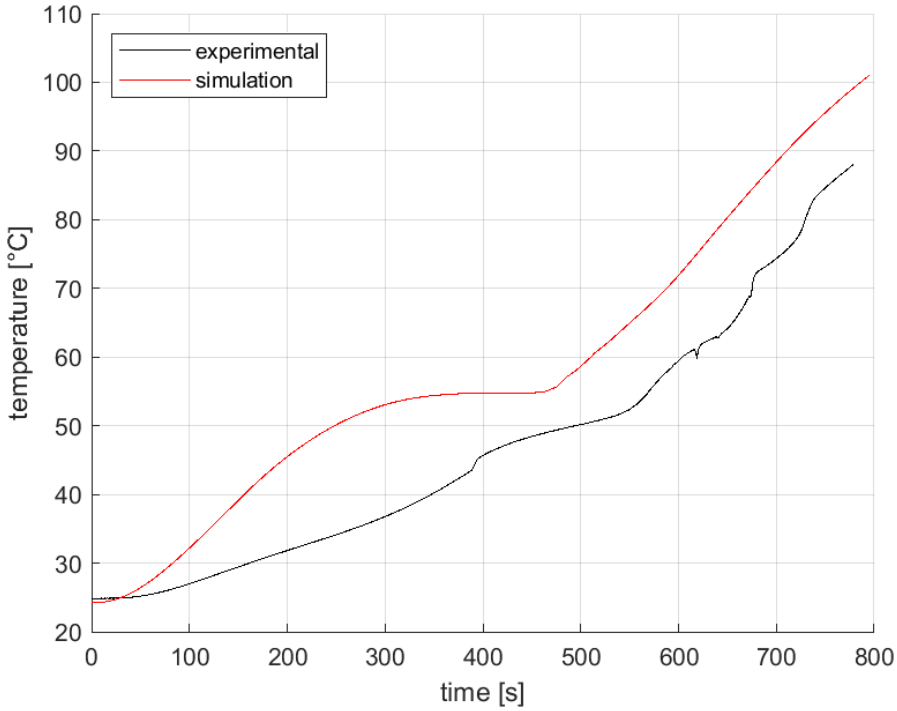

Figure 4.12 – Profile of the melting of the PCM, RT55, 200 W

4.2.3 RT64HC

The same graphs are reported for the other paraffin

4.2.3.1 100 W

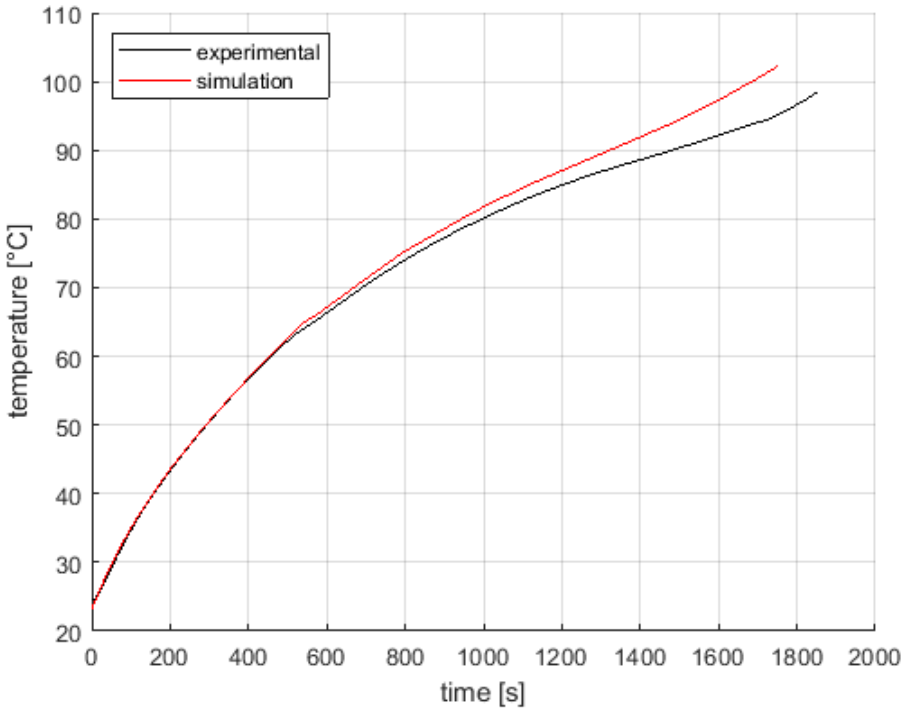

Figure 4.13 – Profile of the heated side of the structure (aluminum), RT64HC, 100 W

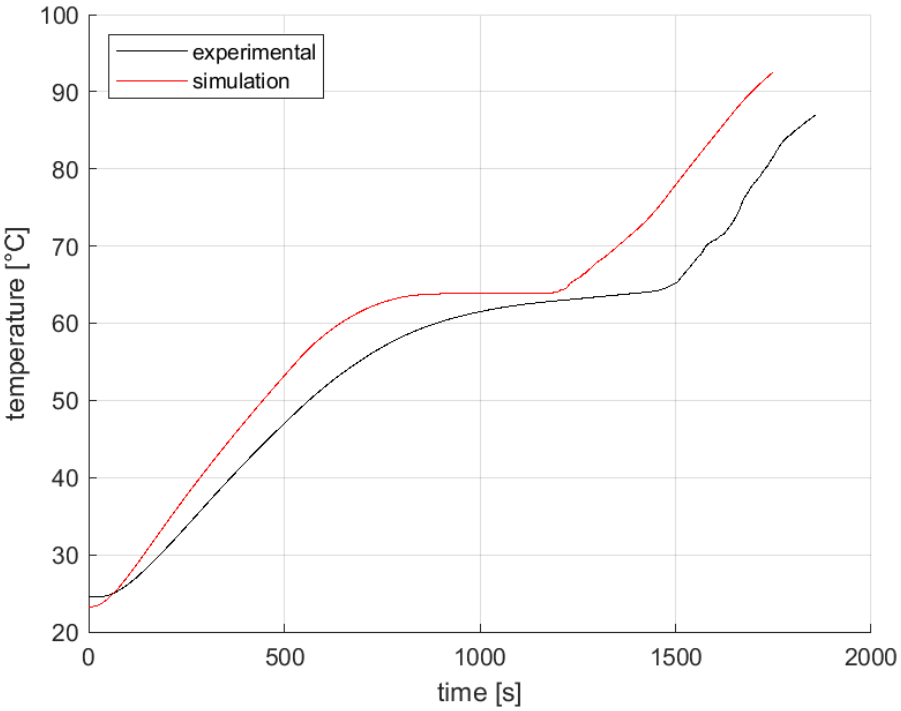

Figure 4.14 – Profile of the melting of the PCM, RT64HC, 100 W

4.2.3.2 150 W

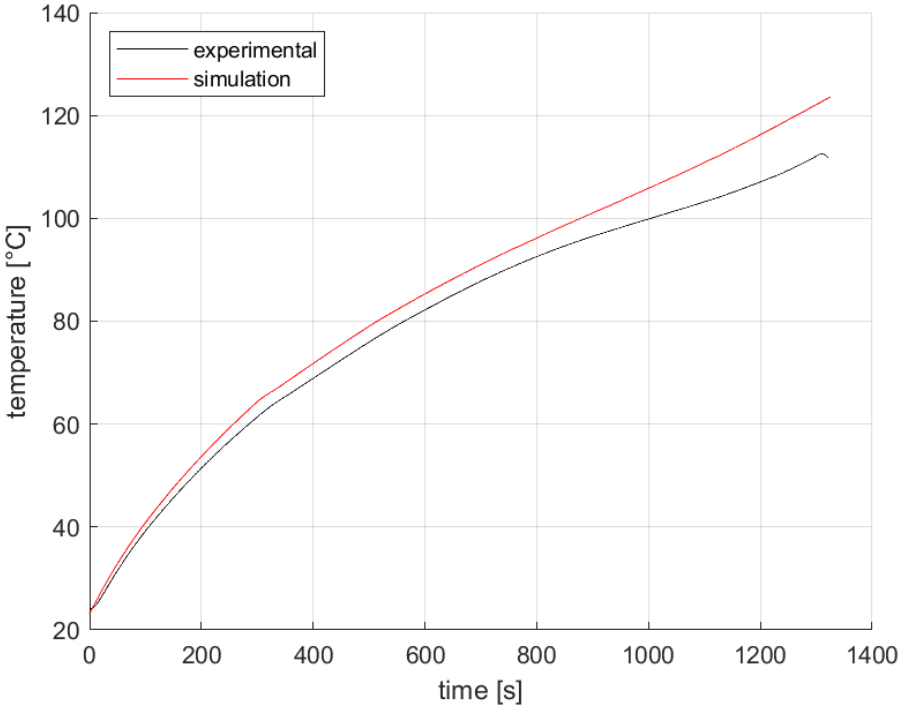

Figure 4.15 – Profile of the heated side of the structure (aluminum), RT64HC, 150 W

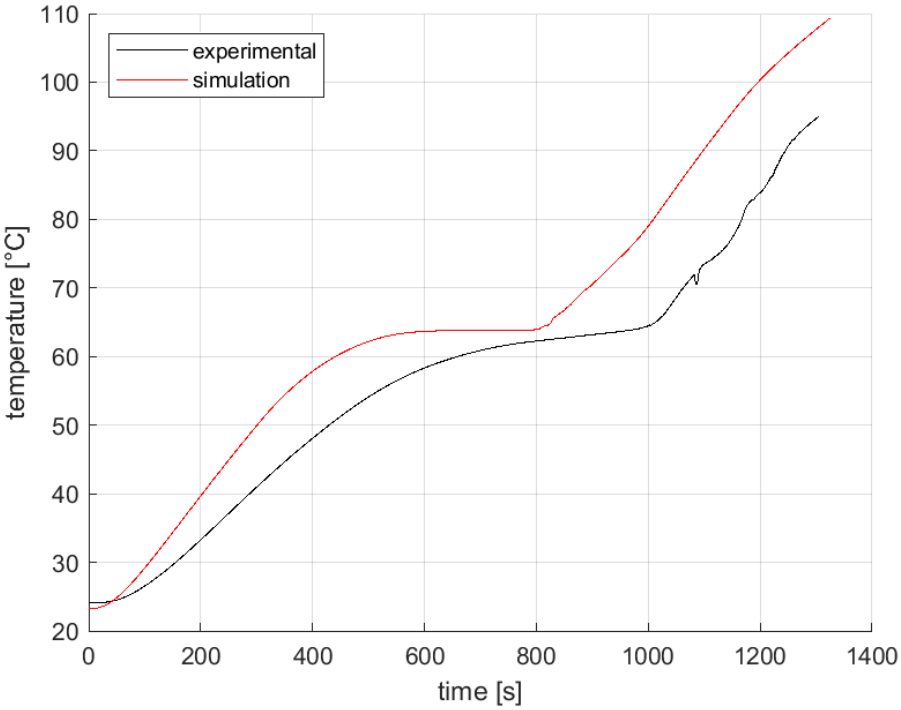

Figure 4.16 – Profile of the melting of the PCM, RT64HC, 150 W

4.2.3.3 200 W

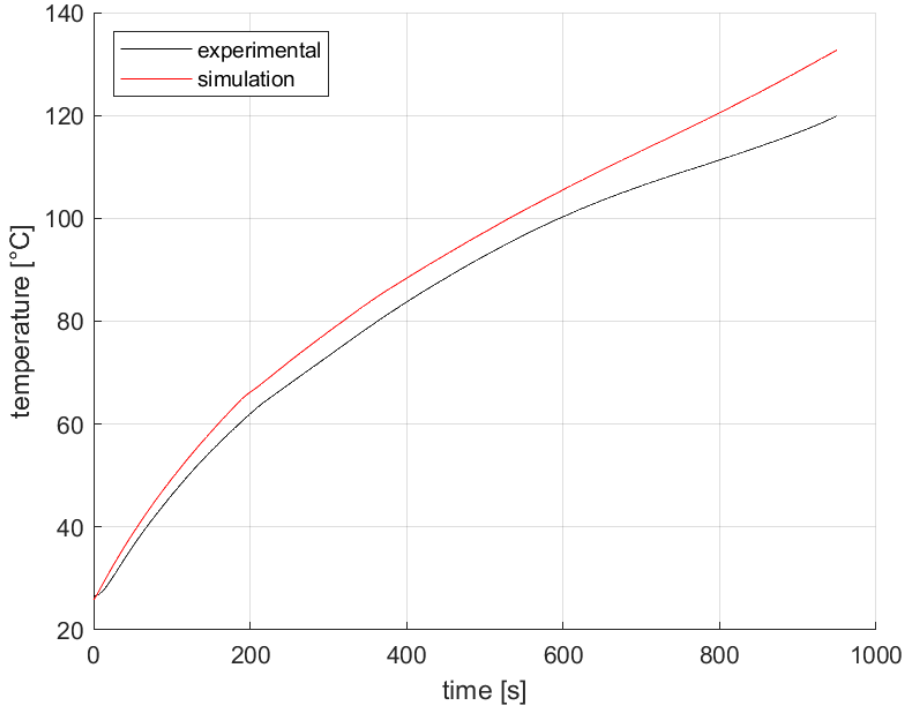

Figure 4.17 – Profile of the heated side of the structure (aluminum), RT64HC, 200 W

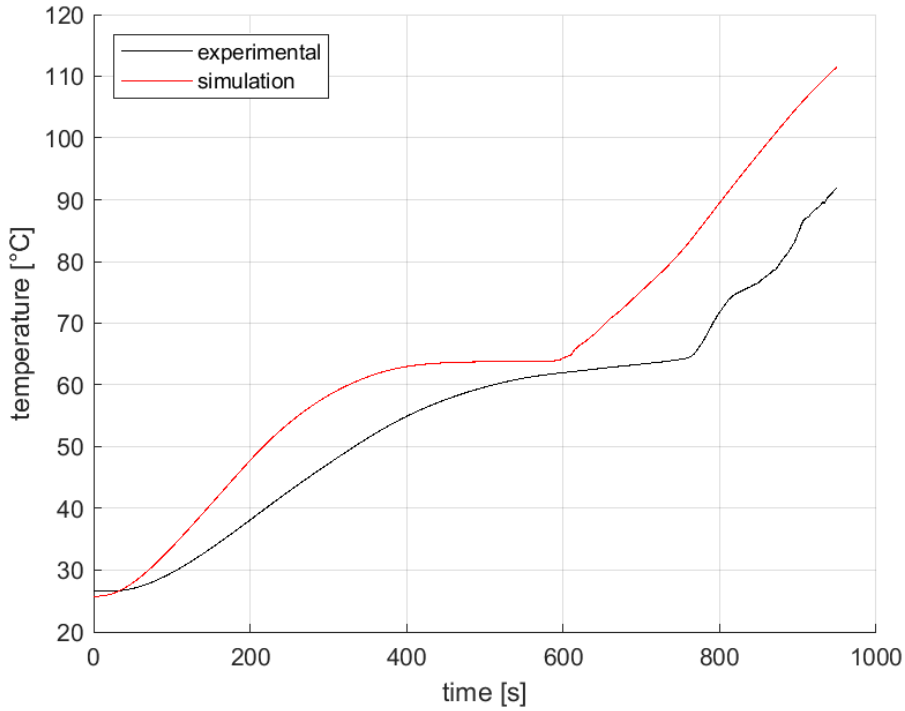

Figure 4.18 – Profile of the melting of the PCM, R64HC, 200 W

The discrepancies that can be seen in particular in the graphs related to the PCM are due to the already listed simplifications. In particular, the obtained representation is due, once again, to the choice of imposing a constant density, and so the absence of expansion during the phase change and of the natural convection, and to the adoption of a fixed temperature for the melting process, without a range of it between the solid and liquid phase respectively. In conclusion, this problem can be neglected if the focus of the simulation is on the optimal description of the heat transfer process on the heated side, which was the main goal of the study. A further addition can be done noticing how the behaviour of the PCM changes with the type of paraffin used. In particular, the highest the latent heat and the melting temperature, the more adherent is the curve to the experimental one.

CHAPTER 5 – Empirical model

5.1 Diani and Campanale [1] power law

All the acquired data, also from previous studies, where compared with the correlation developed and proposed by Diani and Campanale [1]. The steps to obtain the interest parameters are shown, in particular, the equation is composed by different dimensionless quantities, related one to the others. Starting from the Fourier number, it is possible to represent the ratio between the transfer by diffusion and the stored energy:

$$Fo = \frac{k_{eff} \cdot t_{melt}}{\rho_{eff} \cdot c_{p,eff} \cdot h^2} \tag{5.1}$$

where:

- t_{melt} is the time needed to melt all the paraffin
- h is the height of the PCM, compared to the fusion front, so the distance of the fusion front on the heated side, in this case set 0.02 m
- k_{eff} is the effective thermal conductivity, from:

$$k_{eff} = 0.33 \cdot k_{solid} \cdot (1 - \varepsilon) \tag{5.2}$$

with k_{solid} the density of the metal support structure, made by aluminum alloy (175 W m^{-1} K^{-1}) and ε the porosity.

- ρ_{eff} is the effective density, taking into account both the PCM and the aluminum structure, namely subscript “PCM” and “solid”:

$$\rho_{eff} = \varepsilon \cdot \rho_{PCM} + (1 - \varepsilon) \cdot \rho_{solid} \tag{5.3}$$

- $c_{p,eff}$ the specific heat, evaluated as:

$$c_{p,eff} = \varepsilon \cdot \frac{\rho_{PCM}}{\rho_{eff}} \cdot c_{p,PCM} + (1 - \varepsilon) \cdot \frac{\rho_{solid}}{\rho_{eff}} \cdot c_{p,solid} \tag{5.4}$$

The considerations done in the previous point, on the subscripts, are still valid.

Stefan number is the second dimensionless parameter, defined as the ratio between the sensible heat transfer and the latent heat transfer:

$$Ste = \frac{c_{p,eff} \cdot (T_{melt} - T_i)}{L_{eff}} \tag{5.5}$$

defining:

- T_{melt} melting temperature of the considered paraffin [°C]
- T_i the initial temperature [°C]
- L_{eff} the effective latent heat [J kg^{-1}], from:

$$L_{eff} = \varepsilon \cdot \frac{\rho_{PCM}}{\rho_{eff}} \cdot L_{PCM} \tag{5.6}$$

The last dimensionless parameter is the dimensionless temperature θ, described as:

$$\theta = \frac{T_f - T_{melt}}{T_{melt} - T_i} \tag{5.7}$$

with T_f is the temperature of the heated plate at the end of the melting process [°C].

Finally, it is possible to develop in a graph the dimensionless temperature θ as function of the product between Fourier and Stefan number:

$$Fo \cdot Ste = \frac{k_{eff} \cdot t_{melt} \cdot (T_{melt} - T_i)}{\rho_{eff} \cdot h^2 \cdot L_{eff}} \tag{5.8}$$

High values of this product and low values of the dimensionless temperature θ correspond to low heat flux.

The final power law shown from Diani and Campanale [1] is:

$$\theta = 1.9073 \cdot \ (Fo \cdot Ste)^{-0.717} \tag{5.9}$$

Figure 5.1 reports the overall experimental points, coming from analysis with BCC structure with 5 mm side cell and 10 mm side cell, lattice structures with 5 mm side cell and 10 mm side cell, porosity 87% and 93%.

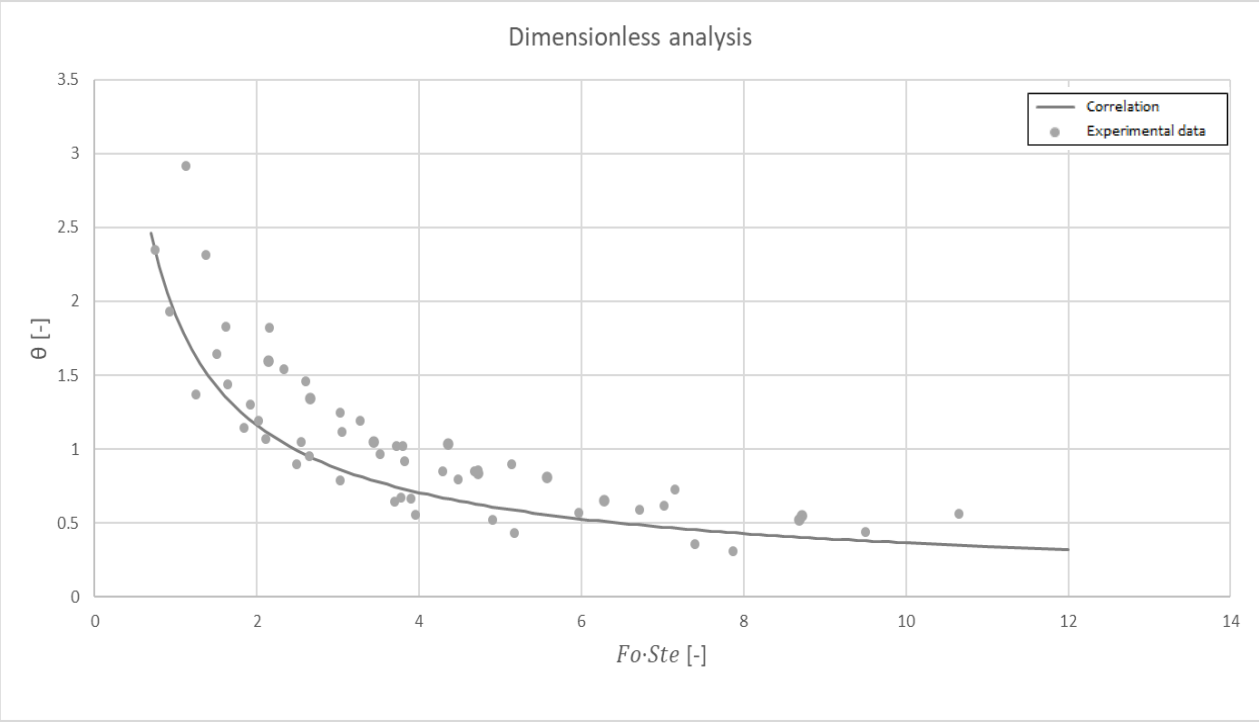

Figure 5.1 – graphical representation of the existing power law proposed from Diani and Campanale [1]

5.2 Development of the new power law

The main goal of the presented dimensionless analysis, as it was shown, regarded the possibility to represent a relationship linking θ as function of the product between Fourier and Stefan number, in order to obtain a curve as the one shown in figure 5.1 that interpolates effectively the experimental point, leading to a general formulation usable to estimate present data. The further assigned step was to propose a new definition of this power law. It was introduced a further constant c_3 to the previous one, exponent of the added product between a_{sv}, ratio between the surface and the volume of the structure [m^{-1}] and the distance of the melting front from the heated plate, that is the height of the PCM perpendicular to the melting front (0.02 m for the present tested structures).
In the end, the new power law will have the form:

$$\theta = c_1 \cdot \ (Fo \cdot Ste)^{c_2} \cdot (a_{sv} \cdot h)^{c_3} \tag{5.10}$$

All the process was coded in Matlab, with the input of the data coming from the current experimental tests and the values obtained in past observations. In particular, it was developed a formulation for the lattice geometries, the BCC ones and finally and overall power law including all the structures. Equation (5.10) is used to predict the time needed to melt the paraffin inserted in the given metallic structure, as well as the temperature of the side in contact with the heater. This equation must be coupled with an energy balance of the entire system, which depends on the specific application, as [1]:

$$\begin{aligned} q \cdot A_{heated} \cdot t_{melt} = \ & m_{PCM} \cdot L_{PCM} + m_{PCM} \cdot c_{p,PCM} \cdot \left(\frac{T_f + T_{melt}}{2} - \ T_i\right) \\ & + m_{Al,cage} \cdot c_{p,Al} \cdot \left(\frac{T_f + T_{melt}}{2} - \ T_i\right) \\ & + m_{heater} \cdot c_{p,heater}\left(T_f - \ T_i\right) \\ & + \sum_i Q_i \end{aligned} \tag{5.11}$$

and the results of which will be shown in a subsequent paragraph, as well as the terms composing it. Equations (5.10) and (5.11) form a system of two unknowns, T_f and t_{melt}, the temperature reached by the heated plate at the end of the melting process and the time needed to completely melt the paraffin respectively.

The value of a_{sv} is obtained finding an equation that links the porosity with the thickness of the fibre, t, value which is varying depending on the geometry taken into account. The porosity is evaluated as the difference from the unity given by the relative density, ϱ^*, evaluated as the ratio between the volume occupied by the fibres and the total volume. At the end it is possible to calculate both of them as:

$$\varepsilon = 1 - \frac{12 \cdot l \cdot t^2 - 16 \cdot t^3}{l^3} \tag{5.12}$$

where:

$$\varrho^* = \frac{12 \cdot l \cdot t^2 - 16 \cdot t^3}{l^3} \tag{5.13}$$

Finally:

$$a_{sv} = \frac{24 \cdot l \cdot t - 48 \cdot t^2}{l^3} \tag{5.14}$$

5.2.1 Lattice structures

The analysis started with the lattice structures since it was the main geometry for which the experiments were taken. Once the power law was developed, it was applied also for the previous analyzed geometries. In this paragraph the obtained outcomes are reported, taking into account the relative deviation in order to evaluate the fairness of the results:

$$dev = \frac{\theta_{calc} - \theta}{\theta} \cdot 100 \tag{5.15}$$

Where θ_{calc} is the value obtained from (5.10), while θ is coming from the conducted tests.
The results will be reported both in graphs and tables, considering the mean of the deviations and the mean of their absolute values. The maximum acceptable value is fixed to 10%. The final power law is:

$$\theta = 0.1118 \cdot \ (Fo \cdot Ste)^{-0.729} \cdot (a_{sv} \cdot h)^{-0.559} \tag{5.16}$$

for the combined data, considering both the geometries (10 mm and 5 mm) and both porosity (87% and 93%).

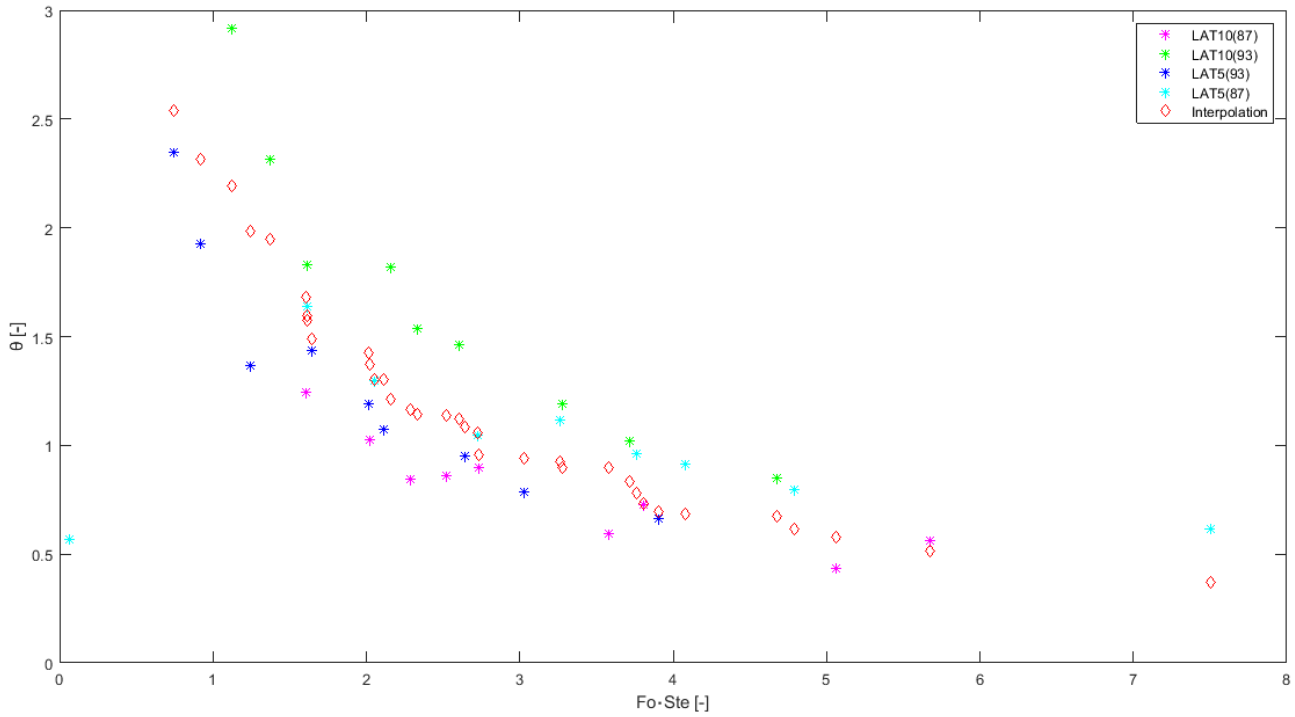

Figure 5.2 - representation of the result of the application of the power law for the overall lattice structures (from (5.16))

From the mean of the values of the relative deviation, it is calculated the mean relative error, and from the mean of the absolute values of the same, it is evaluated the mean absolute error. Finally, it is proposed a comparison between the previous power law and the new one:

Lat old	**mean relative error** [%]	**mean absolute error** [%]
	-8.36	18.35

Table 5.1 - values of the errors with the old power law, for the lattice structures

Lat new	**mean relative error** [%]	**mean absolute error** [%]
	1.28	8.15

Table 5.2 - values of the errors with the new power law, for the lattice structures

Overall, all the limits are respected and the obtained interpolation is fine. It is important to remember that, for the tested geometry, it will be presented the energy balance solution, in order to evaluate the previously presented two variables: at the end, those values will be the reference ones in order to understand if the power law describes adequately the behaviour of the system.

5.2.1.1 10 mm cells

The same assumptions done in the previous paragraph remain valid for the current geometry. The final power laws are:

$$\theta = 2.0398 \cdot \ (Fo \cdot Ste)^{-0.735} \cdot (a_{sv} \cdot h)^{0.031} \tag{5.17}$$

for the geometry with 87% porosity

$$\theta = 2.1238 \cdot \ (Fo \cdot Ste)^{-0.816} \cdot (a_{sv} \cdot h)^{-0.064} \tag{5.18}$$

for the geometry with 93% porosity

$$\theta = 2.0818 \ \cdot (Fo \cdot Ste)^{-0.776} \cdot (a_{sv} \cdot h)^{-0.017} \tag{5.19}$$

for the combined data, considering both the geometries.

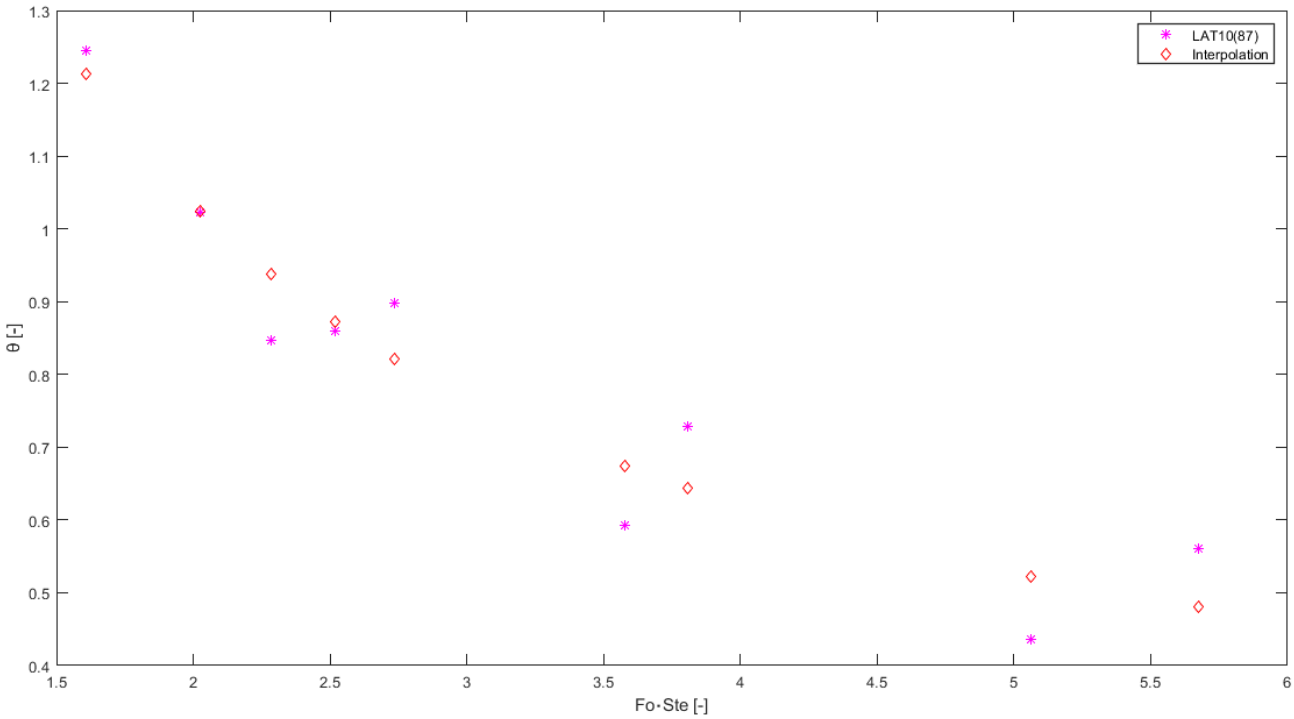

Figure 5.3 - representation of the result of the application of the power law (from (5.17)) for the 10 mm side structures, 87% porosity

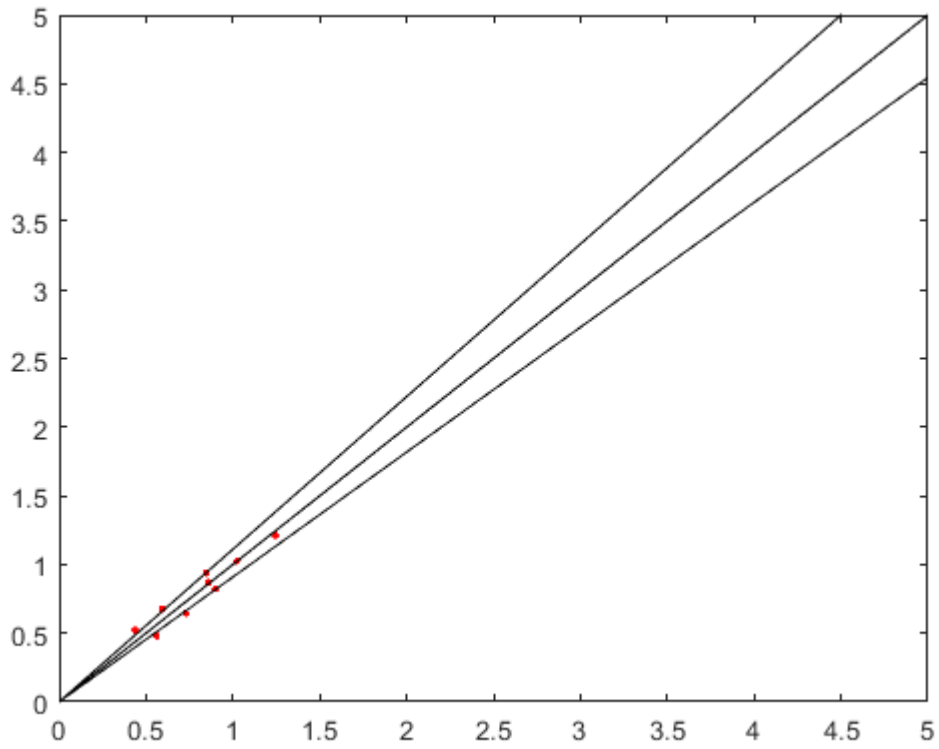

Figure 5.4 - deviations of the obtained values of teta in between -10% and +10% for the structure with 87% porosity

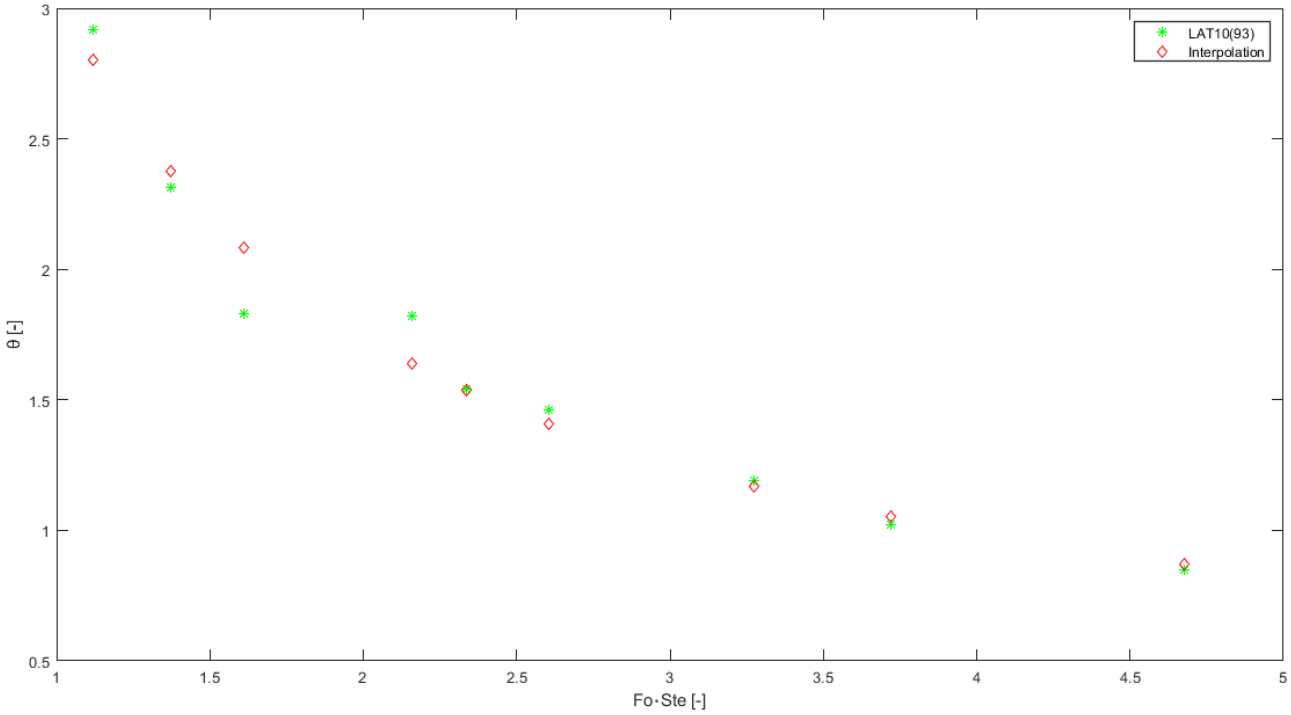

Figure 5.5 - representation of the result of the application of the power law (from (5.18)) for the 10 mm side structures, 93% porosity

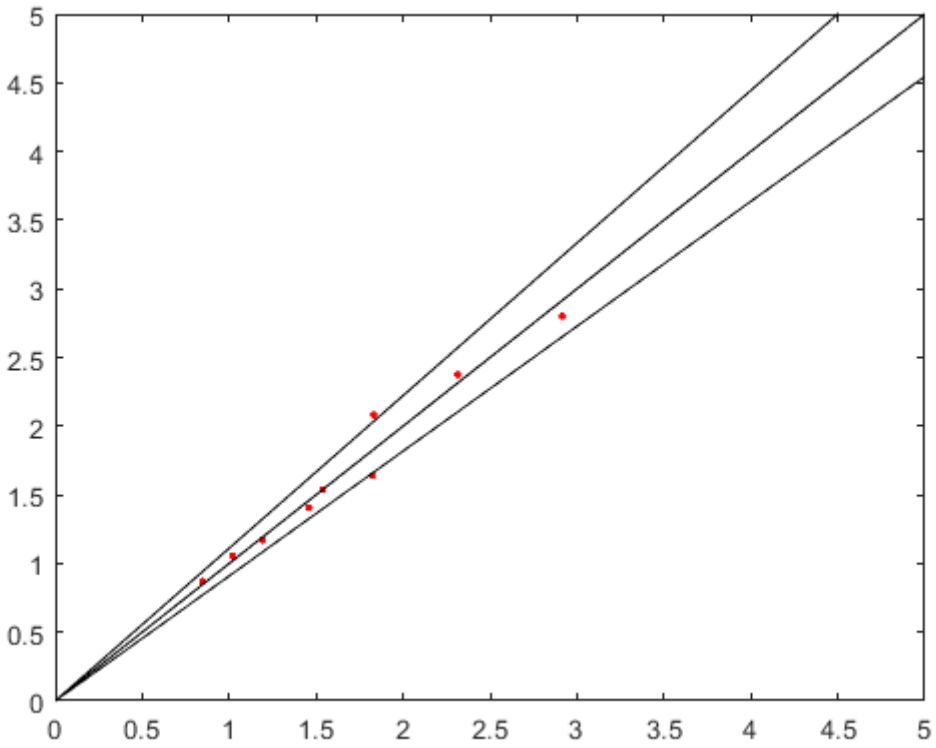

Figure 5.6 – deviations of the obtained values of teta in between -10% and +10% for the structure with 93% porosity

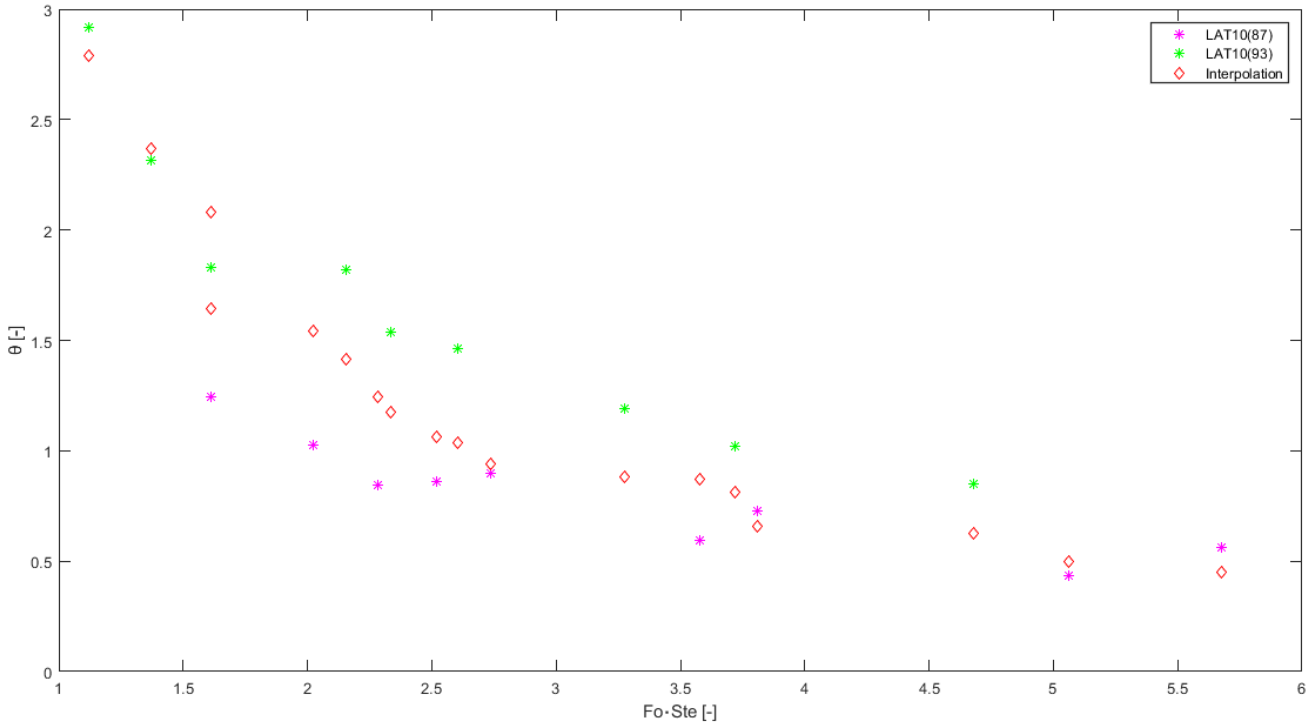

Figure 5.7 - representation of the result of the application of the power law for the overall lattice structures (from (5.19)) for the 10 mm side structures

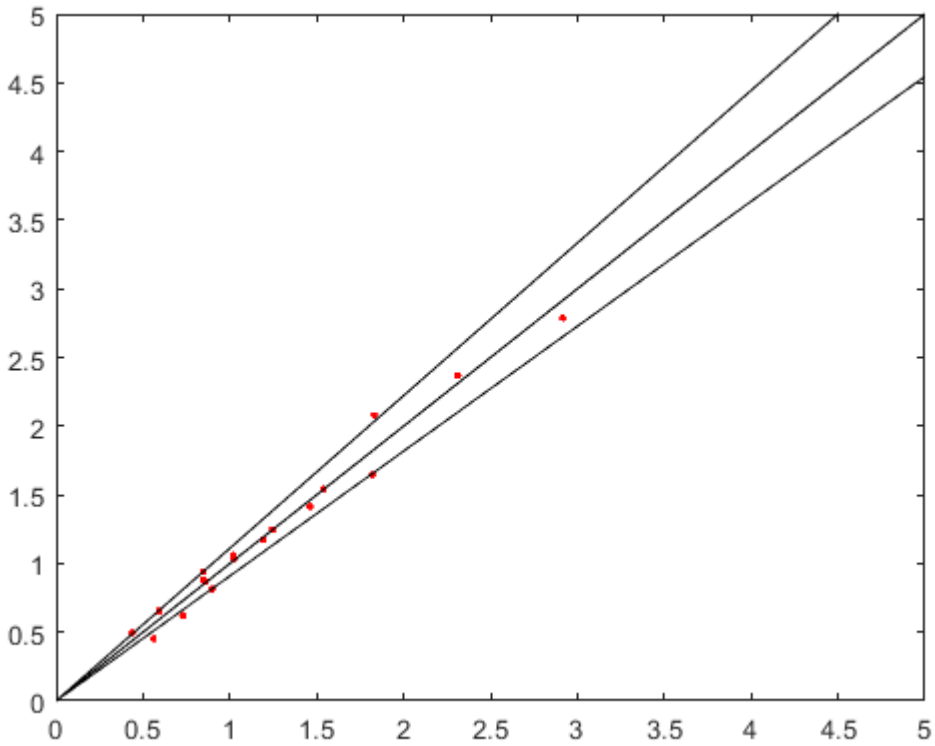

Figure 5.8 – deviations of the obtained values of teta in between -10% and +10% for the overall 10 mm structures

From the mean of the values of the relative deviation, it is calculated the mean relative error, and from the mean of the absolute values of the same, it is evaluated the mean absolute error. Finally, as before, it is proposed a comparison between the previous power law and the new one:

Lat 10 old	mean relative error [%]	mean absolute error [%]
87%	-30.72	30.72
93%	-32.32	32.32
both	-31.52	31.52

Table 5.3 - values of the errors with the old power law, for the lattice structure (10 mm)

Lat 10 new	mean relative error [%]	mean absolute error [%]
87%	0.92	9.19
93%	0.3	4.66
both	0.02	6.89

Table 5.4 - values of the errors with the new power law, for the lattice structure (10 mm)

All the limits are respected and the obtained interpolation is more than fine.

5.2.1.2 5 mm cells

The same assumptions done in the previous paragraph remain valid for the current geometry. The results will be reported both in graphs and tables, considering the mean of the deviations and the mean of their absolute values.

The final power laws are:

$$\theta = 2.0608 \cdot \ (Fo \cdot Ste)^{-0.614} \cdot (a_{sv} \cdot h)^{-0.006} \tag{5.20}$$

for the geometry with 87% porosity.

$$\theta = 2.1184 \cdot \ (Fo \cdot Ste)^{-0.722} \cdot (a_{sv} \cdot h)^{0.027} \tag{5.21}$$

for the geometry with 93% porosity.

$$\theta = 2.08976 \cdot \ (Fo \cdot Ste)^{-0.668} \cdot (a_{sv} \cdot h)^{0.011} \tag{5.22}$$

for the combined data, considering both the geometries.

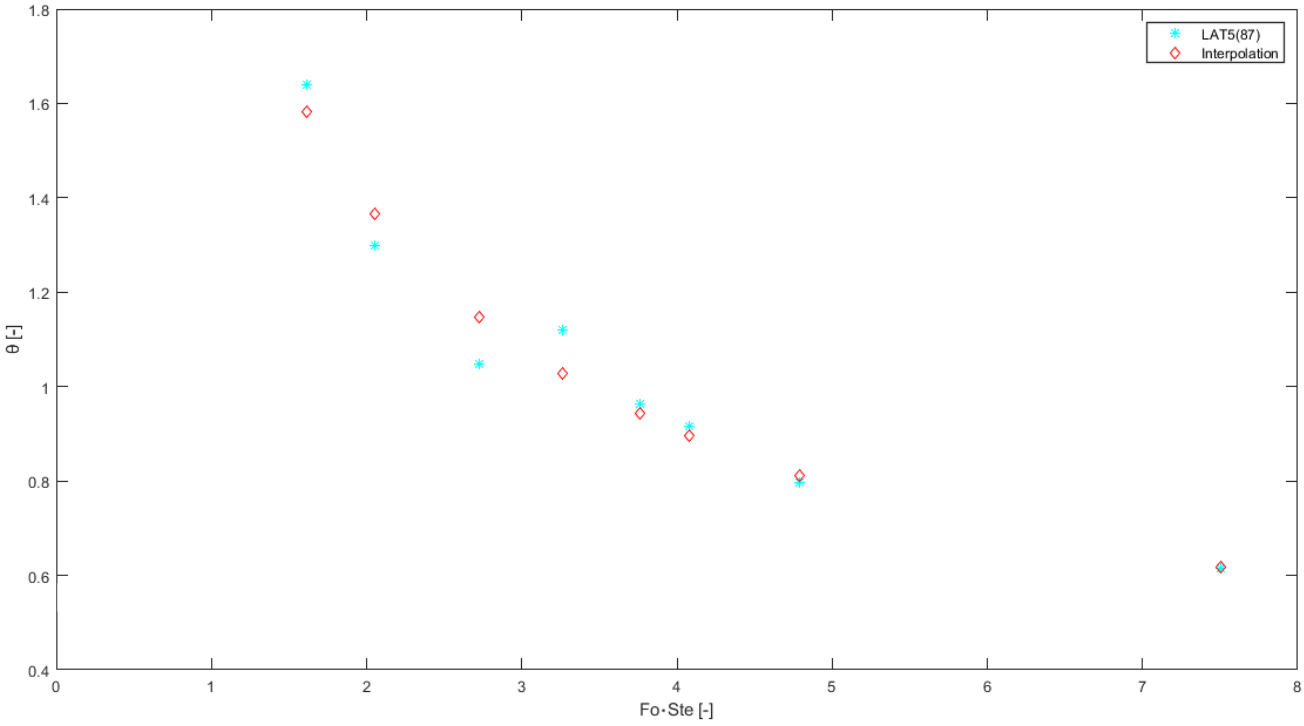

Figure 5.9 - representation of the result of the application of the power law (from (5.20)) for the 5 mm side structures, 87% porosity

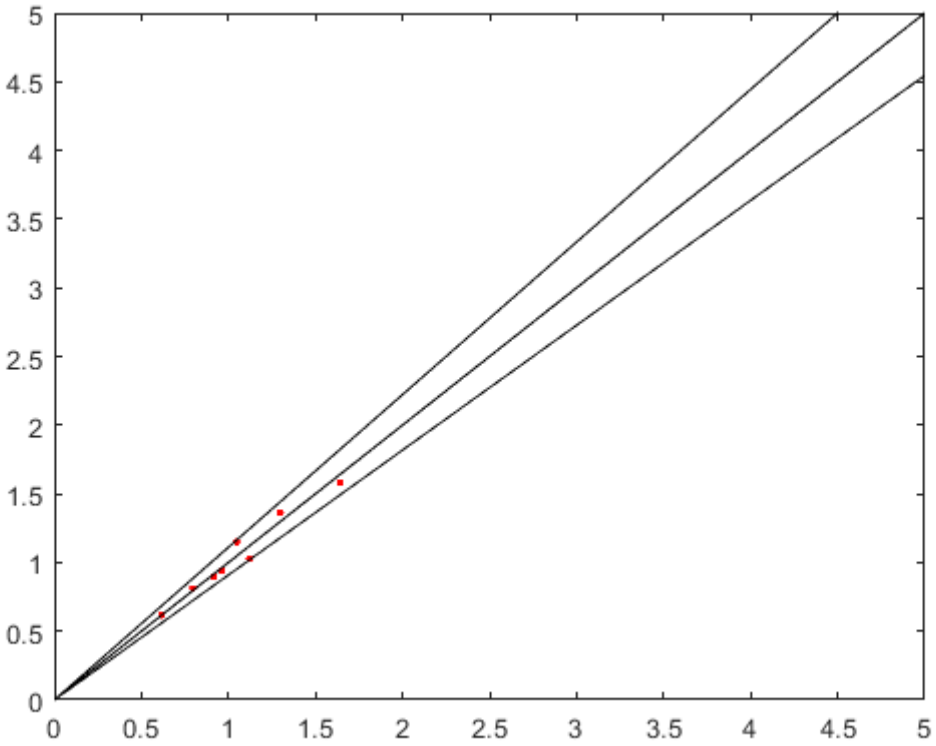

Figure 5.10 - deviations of the obtained values of teta in between -10% and +10% for the structure with 87% porosity

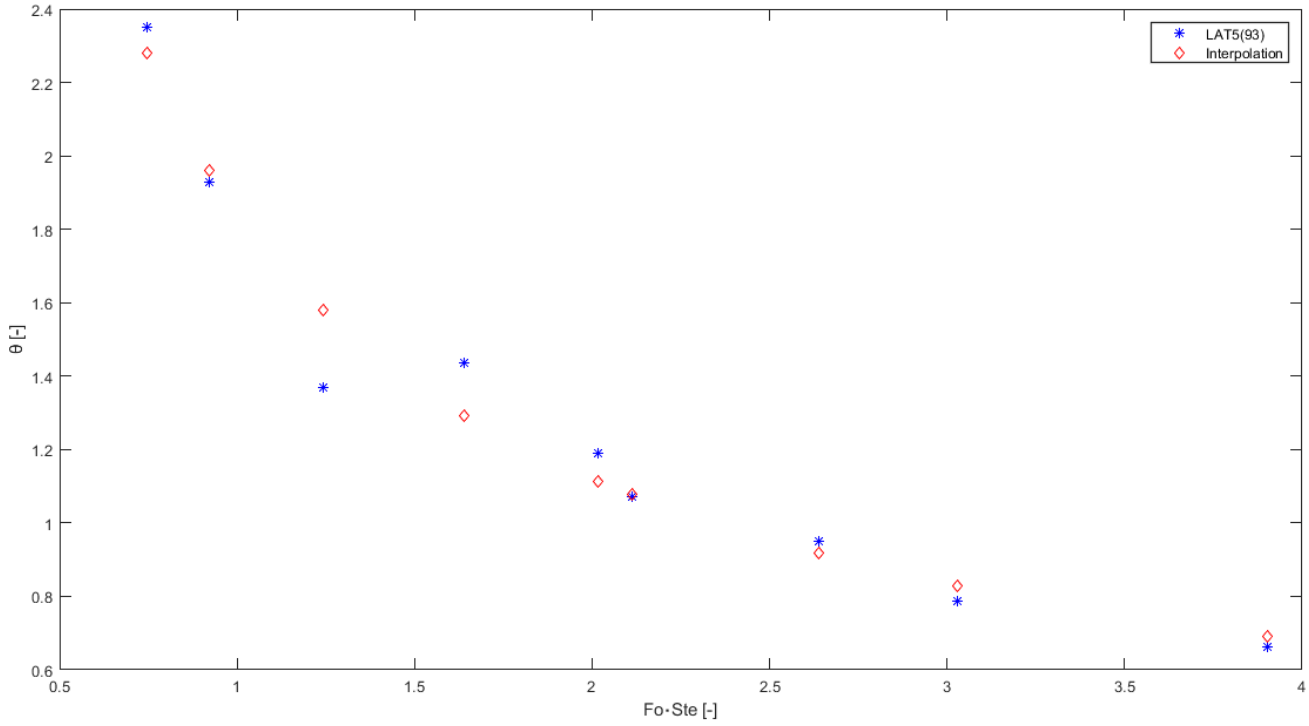

Figure 5.11 - representation of the result of the application of the power law (from (5.21)) for the 5 mm side structures, 93% porosity

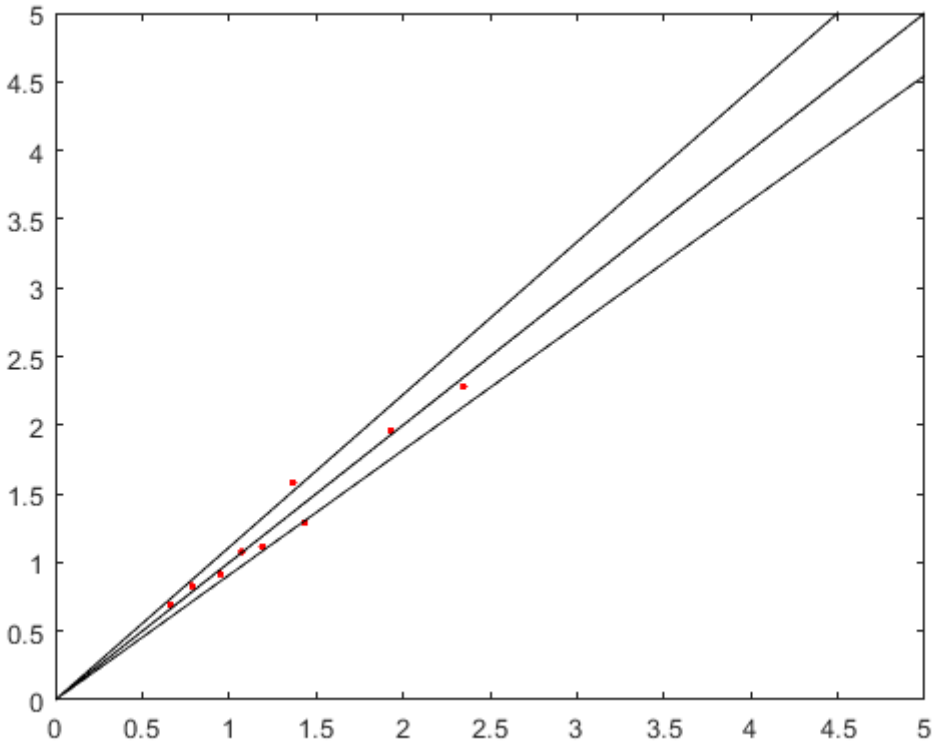

Figure 5.12 - deviations of the obtained values of teta in between -10% and +10% for the structure with 93% porosity

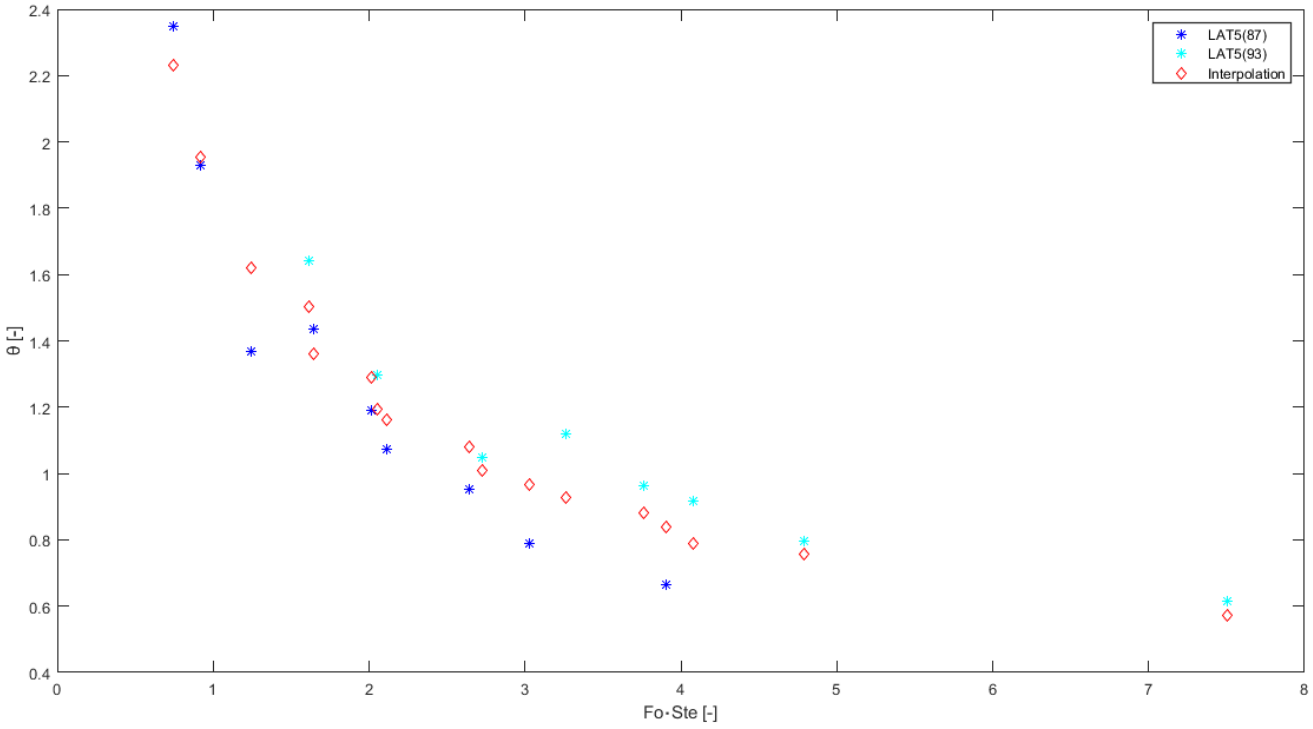

Figure 5.13 – representation of the result of the application of the power law for the overall lattice structures (from (5.22)) for the 5 mm side structures

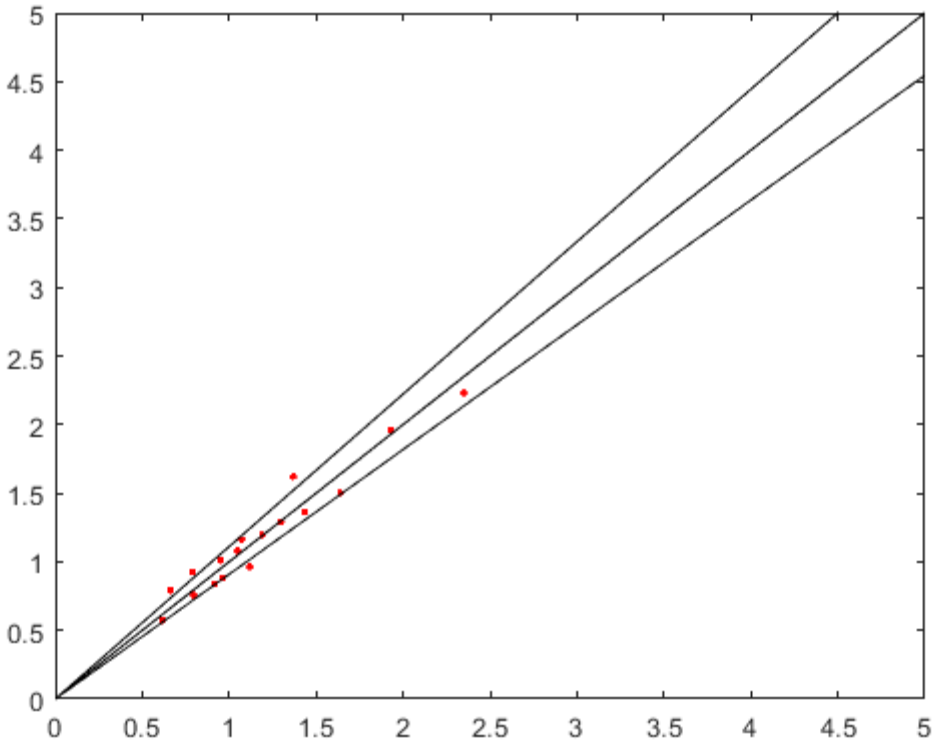

Figure 5.14 – deviations of the obtained values of teta in between -10% and +10% for the overall 5 mm structures

Lat 5 old	mean relative error [%]	mean absolute error [%]
87%	-19.48	19.48
93%	3.96	6.19
both	-7.76	12.84

Table 5.5 - values of the errors with the old power law, for the lattice structure (5 mm)

Lat 5 new	mean relative error [%]	mean absolute error [%]
87%	0.15	4.13
93%	0.45	5.55
both	0.75	8.00

Table 5.6 - values of the errors with the new power law, for the lattice structure (5 mm)

Once again, all the limits are respected and the obtained interpolation is fine.

5.2.2 BCC structures

The obtained outcomes are reported also for the BCC structures (87% porosity), taking into account the relative deviation in order to evaluate the fairness of the results, once again from (5.15).
The results will be reported both in graphs and tables, considering the mean of the deviations and the mean of their absolute values. The maximum acceptable value is fixed to 10%. The final power law is:

$$\theta = 0.1118 \cdot \ (Fo \cdot Ste)^{-0.729} \cdot (a_{sv} \cdot h)^{-0.559} \tag{5.23}$$

for the combined data, considering both the geometries (10 mm and 5 mm).

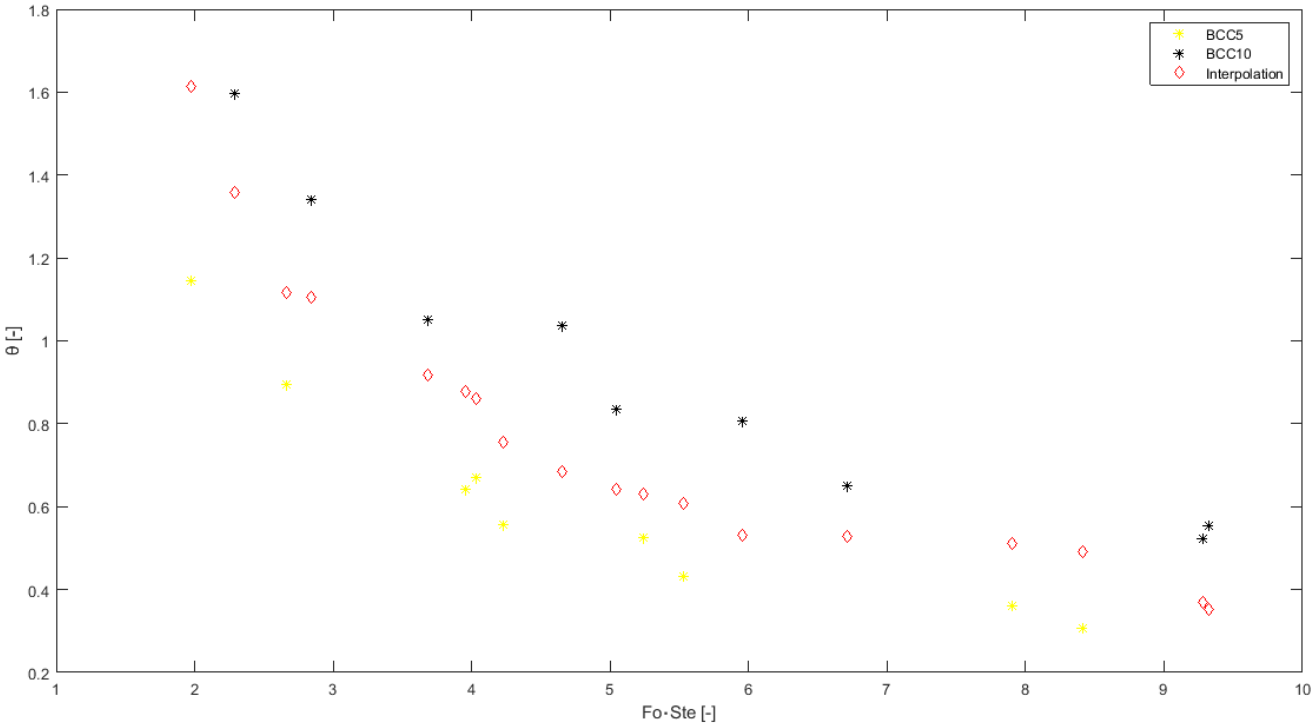

Figure 5.15 – graphical representation of the power law proposed for the BCC structures

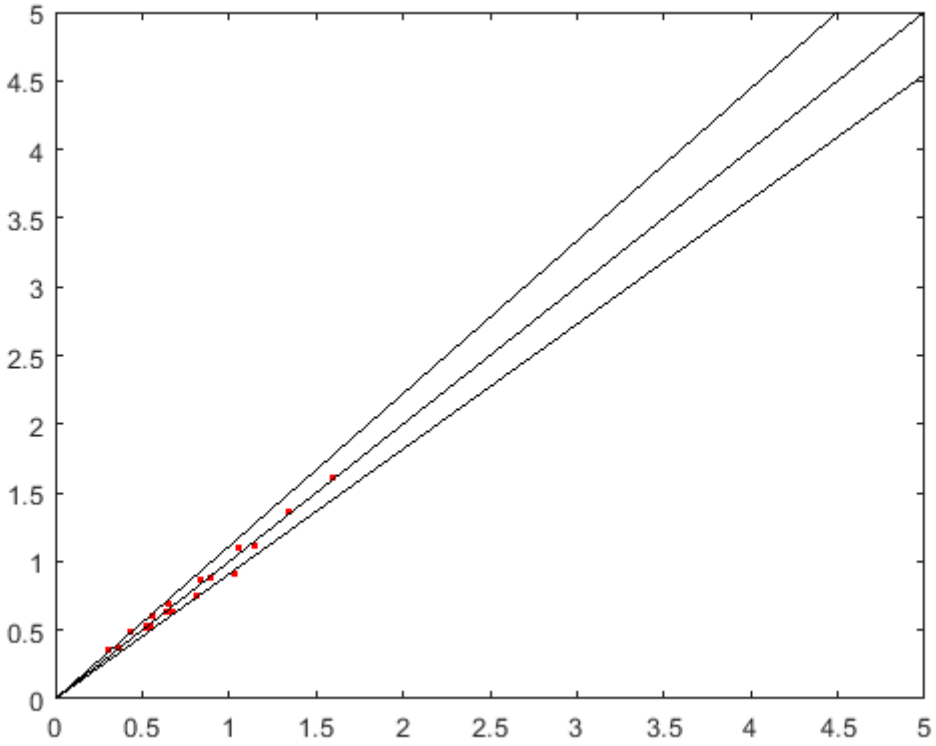

Figure 5.16 - deviations of the obtained values of teta in between -10% and +10% for the BCC structures

BCC old	mean relative error [%]	mean absolute error [%]
	-7.69	23.30

Table 5.7 - values of the errors with the old power law, for the BCC structures

BCC new	mean relative error [%]	mean absolute error [%]
	1.2	5.10

Table 5.8 - values of the errors with the new power law, for the BCC structures

All the consideration done in the previous chapter, related to the lattice geometries, are still valid, and, overall, it is possible to see how the new power law satisfies the listed prerequisites.

5.2.3 Overall power law

The last provided step was the evaluation of the overall power law, considering all the lattice structures (5 mm, 87% and 93% porosity, 10 mm, 87% and 93% porosity) and all the BCC structures (5 mm and 10 mm, 87% porosity). Once again, at the end it was taken into account the relative deviation in order to evaluate the fairness of the results, from (5.15).

The maximum acceptable value is fixed to 10%. The final power law is:

$$\theta = 0.2575 \cdot \ (Fo \cdot Ste)^{-0.465} \cdot (a_{sv} \cdot h)^{-0.380} \tag{5.24}$$

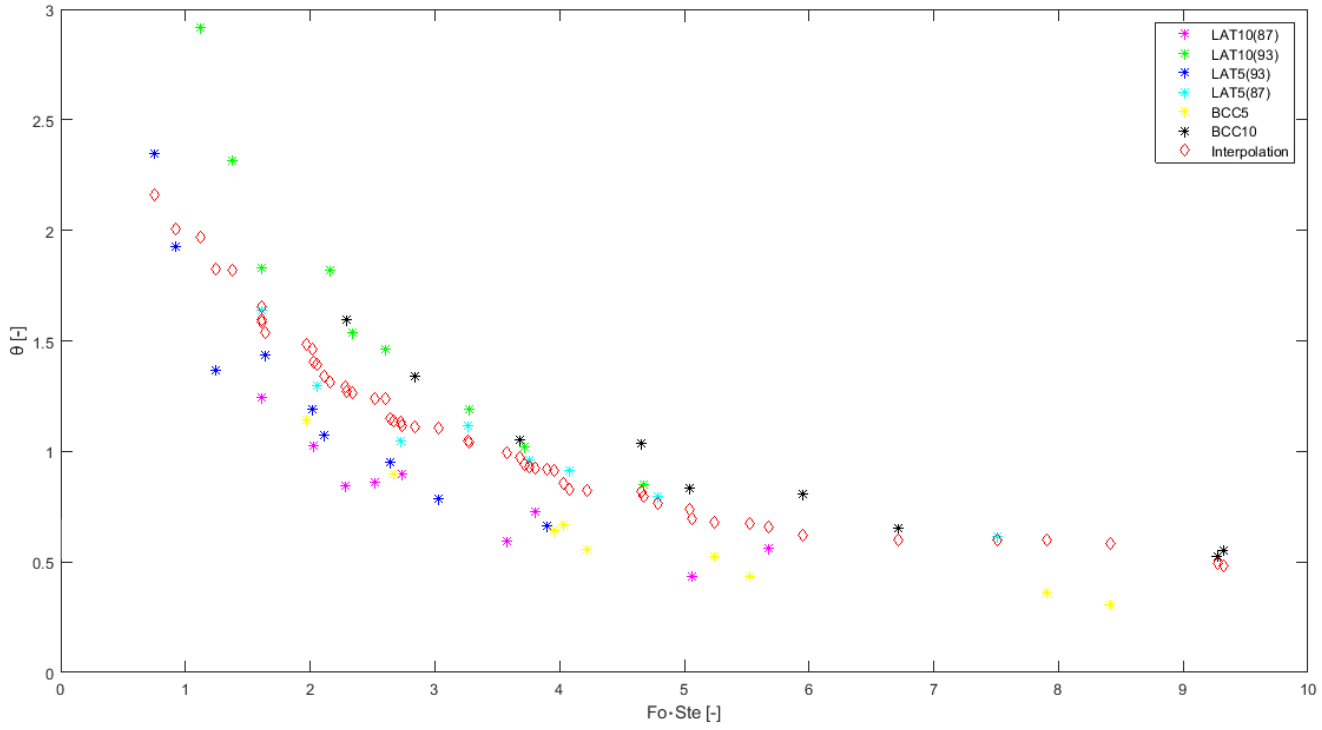

Figure 5.17 – graphical representation of the overall proposed power law

Overall old	mean relative error [%]	mean absolute error [%]
	-7.69	23.30

Table 5.9 - values of the errors with the old power law, for the overall structures

Overall new	mean relative error [%]	mean absolute error [%]
	2.10	10.00

Table 5.10 – values of the errors with the new power law, for the overall structures

This final result concludes the analysis of the new produced power law, showing largely how it was obtained an implemented formulation thanks to the introduction of a further constant c_3 to the previous one, as exponent of the added product between a_{sv}, and the distance of the melting front from the heated plate, which is the height of the PCM perpendicular to the melting front. In this way it was possible to find different solutions, from the most specific and singular case, to the most inclusive one, comprehending also the geometries studied in the past.

5.3 Energy balance evaluation

From the previous paragraph it was shown how it was developed a formulation for the lattice geometries, the BCC ones and finally and overall power law including all the structures. Equation (5.10) is used to predict the time needed to melt the paraffin inserted in the given metallic structure, as well as the temperature of the side in contact with the heater. The coefficients of the power law are the ones reported in (5.18). This equation must be coupled with an energy balance of the entire system, which depends on the specific application. The formulation is reported again below for viewing convenience:

$$\begin{aligned} q \cdot A_{heated} \cdot t_{melt} = \; & m_{PCM} \cdot L_{PCM} + m_{PCM} \cdot c_{p,PCM} \cdot \left(\frac{T_f + T_{melt}}{2} - T_i \right) \\ & + m_{Al,cage} \cdot c_{p,Al} \cdot \left(\frac{T_f + T_{melt}}{2} - T_i \right) \\ & + m_{heater} \cdot c_{p,heater} \left(T_f - T_i \right) \\ & + \sum_i Q_i \end{aligned} \tag{5.11}$$

The term on the left side corresponds to the total thermal energy supplied by the heater, the terms on the right side correspond, respectively, to the latent heat to completely melt the PCM, sensible heat needed to bring the PCM from T_i to its final temperature (average value between the temperature of the heated plate and the melting temperature), heat needed to bring the cage from T_i to its final temperature (average value between the temperature of the heated plate and the melting temperature), heat needed to bring the heater from T_i to T_f. The last term on the right side corresponds to the heat needed to bring all the boundary components from their initial temperature to their final temperature. This term depends on the specific set up: in this case, it corresponds to the left and right aluminum plates, to the Bakelite plates and Teflon housing.

The calculation of the necessary parameters (relative density, porosity and ratio between the surface and the volume of the structure) was already presented in Equations (5.12), (5.13) and (5.14), in *Table 5.11* are reported the values for the analyzed geometry (10 mm and 93% porosity):

l [mm]	t [mm]	ϱ^* [-]	ε [-]	a_{SV} [m^{-1}]
10	0.8	0.0686	0.93	0.161

Table 5.11 – geometrical parameters of the structure

All the other physical parameters are calculated based on the properties of the different materials. *Table 5.12* presents the final values, taking into account once again the relative deviation and the respective mean relative and absolute errors in order to control the fairness of the results. The calculations were done taking into account all the three paraffin and the different values of power provided from the heating plate:

T_i [°C]	q [W]	T_{melt} [°C]	t_{melt_data} [s]	$Tf_{\_data}$ [°C]	t_{melt_calc} [s]	$Tf_{\_calc}$ [°C]	$dev_{abs}(t_{melt})$ [%]	$dev_{abs}(Tf)$ [-]
24,97	100	42	977	74,26	980	78,31	0,307	0,055
23,62	150	42	767	85,65	733	88,55	4,433	0,034
25,04	200	42	621	96,78	571	98,11	8,052	0,014
25,56	100	55	1327	86,15	1400	86,07	5,501	0,001
26,54	150	55	947	98,73	980	96,12	3,485	0,026
24,90	200	55	776	110,3	798	104,05	2,835	0,057
25,56	100	64	1853	98,44	1831	99,97	1,190	0,016
24,15	150	64	1302	112,2	1322	111,07	1,536	0,010
26,61	200	64	985	122,51	1008	121,83	2,335	0,006

Table 5.12 – deviations of the values of T_f and t_{melt} calculated with the power law from the experimental values

As it is possible to see, the overall values of errors are below the 10%, leading to a representation of the conducted experiments that is more than fair. Moreover, apart from four cases out of eighteen, the other deviations are all even below the 5%, showing the close adherence to the real case. The next and last step was to check if the dissipations in the system, starting once again from the energy balance, were below the 10% value. For this reason, a similar Matlab script was created and the final results are reported in *Table 5.13:*

	Power [W]	dissipation [%]
RT42	100	1,52
	150	2,47
	200	1,88
RT55	100	2,03
	150	2,66
	200	3,72
RT64HC	100	2,01
	150	2,26
	200	2,38

Table 5.13 – final results on dissipations of the system

The overall contributes takes into account of the maximum dissipation on the heated side, conduction in aluminum, heater, Teflon and convection with external air, on the unheated side, conduction in aluminum and Teflon and convection with external air, front side, considering the temperature difference between PCM and air, taking into account the term of thermal resistance provided from the glass component and the external air, the back side, conduction in Bakelite and Teflon and convection with external air and finally the top side, taking into account the convection contributes with air, considering the proper temperature difference. All these terms, compared to the energy balance, led to the final definition of the dissipations that are present in the system. As it is possible to see, in the end all the values are below the maximum limit that was presented before.

Chapter 6 – Conclusions

As it was shown during the discussion of this thesis, PCMs have the great advantage to store thermal energy, thanks to their high latent heat, related to the phase change itself, in particular the passage from solid to liquid phase. In this case the PCMs selected were different paraffin, having distinct melting temperatures. The overall advantages were summed up as economical, since they are cheap materials, not harmful to the human health. Their availability at different melting temperatures, their very poor aggressiveness when in contact with other materials, and finally, their low volume variation during the phase change, which allows them to use, as in the case study, a reduced dimensions apparatus. The different applications related to the store of energy were seen in the renewable energy sources field, but also much more others. The main problem that was addressed in this case was the low thermal conductivity, and the applied principle is to support the enhanced heat transfer with a metallic matrix, in order to improve the overall process (the geometry taken into account is the elementary cell 10 mm, porosity 93%, repeated to form the component). The used paraffin have a melting temperature of 42, 55, and 64 °C. The fairness of the simulations done with the software ANSYS, in particular the Fluent component, reproducing the original geometry (simplified in one cell) was then controlled using the experiments conducted in the laboratory. In addition, starting from the work of Diani and Campanale [1], an improved empirical model was developed, including all the geometries analyzed in past studies, in order to have an overall formulation being able to describe the complex behaviour of the systems. The conclusions about this study are:

- The metallic structure solve the problem related to the low thermal conductivity, as it was already seen, and in particular the analyzed geometry presented higher values of final temperature compared to the other geometries, as well as a larger time needed to complete the melting. Some modifications can be done changing the porosity of the metallic structure, leading to even higher times for the melting, but reduced final temperatures.
- The simulations conducted with ANSYS Fluent, even though the representation of the real case is well done, showed important limits on the description of the melting front, leading to fair overall results, but poor adherence in that case to the studied system. The analysis was focused on the curves of temperatures of the aluminum and PCM, always remembering how, once again due to the simplifications, the melting process was be represented in the simulations as an isothermal line.

In particular, this fact is related to the choice of imposing a constant density, and so the absence of expansion during the phase change and of the natural convection, and to the adoption of a fix temperature for the melting process, without a range of it between the solid and liquid phase respectively. In con conclusion, the representation was adherent for the aluminum side, while for the PCMs contribute, the simulations were less accurate.

- The provided new power laws improved the older one, used as an important base to start the study, with much better approximation of the results obtained in the conducted tests. All the constraints about the values of deviations and dissipations were respected, and the overall final model is a crucial step for the future studies.

BIBLIOGRAPHY

[1] A. Diani e M. Campanale, «Transient melting of paraffin waxes embedded in aluminum foams: experimental and modeling,» International Journal of Thermal Sciences, vol. 144, pp. 119-128, 2019.

[2] M. Opolot, C. Zhao, M. Liu, S. Mancin, F. Bruno, K. Hooman, «A review of high temperature (≥ 500 °C) latent heat thermal energy storage», Renewable and Sustainable Energy Reviews, vol. 160, 2022

[3] A. Sharma, V. V. Tyagi, C. R. Chen e D. Buddhi, «Review on thermal energy storage with phase change materials and applications,» Renewable and Sustainable Energy Reviews, vol. 13, pp. 318-345, 2009.

[4] V. N. Stathopoulos e N. C. Elias , «A comprehensive review of recent advances in materials aspects of phase change materials in thermal energy storage», Energy Procedia, vol. 161, pp. 385-394, 2019.

[5] S. R. L. da Cunha e J. L. B. de Aguiar, «Phase change materials and energy efficiency of buildings: A review of knowledge», Journal of Energy Storage, vol. 27, pp. 101083-1-13, 2020.

[6] H. Mehling e L. F. Cabeza, «Heat and cold storage with PCM», Berlino: Springer, 2008.

[7] H. Kimura e J. Kai, «Phase change stability of CaCl2·6H2O,» Solar Energy, vol. 33, pp. 49-55, 1984.

[8] Y. Lin, Y. Jia, G. Alva e G. Fang, «Review on thermal conductivity enhancement, thermal properties and applications of phase change materials in thermal energy storage», Renewable and Sustainable Energy Reviews, vol. 82, pp. 2730-2742, 2018.

[9] S. S. Narayanan, A. Kardam, V. Kumar, N. Bhardwaj, D. Madhwal, P. Shukla, A. Kumar, A. Verma e V. K. Jain, «Development of sunlight-driven eutectic phase change material nanocomposite for applications in solar water heating», Resource-Efficient Technologies, vol. 3, pp. 272-279, 2017.

[10] S. Riahi, M. Liu, R. Jacob, M. Belusko, F. Bruno,« Assessment of exergy delivery of thermal energy storage systems for CSP plants: Cascade PCMs, graphite-PCMs and two-tank sensible heat storage systems», Sustainable Energy Technologies and Assessments, vol. 42, 2020.

[11] A. J. N. Khalifa, K. H. Suffer e M. S. Mahmoud, «A storage domestic solar hot water system with a back layer of phase change material», Experimental Thermal and Fluid Science, vol. 44, pp. 174-181, 2013.

[12] C. Prieto, L. F. Cabeza, «Thermal energy storage (TES) with phase change materials (PCM) in solar power plants (CSP). Concept and plant performance», Applied Energy, vol. 254, 2019.

[13] R. Kandasamy, X. Wang, A. Mujumdar, «Transient cooling of electronics using phase change material (PCM)-based heat sinks», Applied Thermal Engineering, vol. 28, pp. 1047-1057, 2008.

[14] J. Krishna, P. S. Kishore e A. B. Solomon, «Heat pipe with nano enhanced-PCM for electronic cooling application», Experimental Thermal and Fluid Science, vol. 81, pp. 84-92, 2017.

[15] E. Alehosseini, S. M. Jafari, «Micro/nano-encapsulated phase change materials (PCMs) as emerging materials for the food industry», Trends in Food Science & Technology, vol. 91, pp. 116-128, 2019.

[16] K. W. Shah, P. J. Ong, M. H. Chua, S. H. G. Toh, J. J. C. Lee, X. Y. D. Soo, Z. M. Png, R. Ji, J. Xu, Q. Zhu, «Application of phase change materials in building components and the use of nanotechnology for its improvement», Energy and Buildings, vol. 262, 2022.

[17] K. O. Lee, M. A. Medina, E. Raith, X. Sun, «Assessing the integration of a thin phase change material (PCM) layer in a residential building wall for heat transfer reduction and management», Applied Energy, vol. 137, pp. 699-706, 2015.

[18] S. Mondal, «Phase change materials for smart textiles – An overview», Applied Thermal Engineering, vol. 28, pp. 1536-1550, 2008.

[19] M. Itani, N. Ghaddar, K. Ghali, D. Ouahrani e W. Chakroun, «Cooling vest with optimized PCM arrangement targeting torso sensitive areas that trigger comfort when cooled for improving human comfort in hot conditions», Energy and Buildings, vol. 139, pp. 417-425, 2017.

[20] Z. Gu, H. Liu, Y. Li, «Thermal energy recovery of air conditioning system—heat recovery system calculation and phase change materials development», Applied Thermal Engineering, vol. 24, pp. 2511-2526, 2004.

[21] S. F. Hosseinizadeh, F. L. Tan e S. M. Moosania, «Experimental and numerical studies on performance of PCM-based heat sink with different configurations of internal fins,» Applied Thermal Engineering, vol. 31, pp. 3827-3838, 2011.

[22] S. H. Kim, C. S. Heu, J. Y. Mok, S. Kang, D. R. Kim, «Enhanced thermal performance of phase change material-integrated fin-type heat sinks for high power electronics cooling», International Journal of Heat and Mass Transfer, vol. 184, 2022.

[23] K. Lafdi, O. Mesalhy, S. Shaikh, «Experimental study on the influence of foam porosity and pore size on the melting of phase change materials», J. Appl. Phys. 102 (2007) 083549-1-6.

[24] Z. Chen, D. Gao, J. Shi, «Experimental and numerical study on melting of phase change materials in metal foams at pore scale», International Journal of Heat and Mass Transfer, vol. 72, pp. 646-655, 2014.

[25] R. Baby e C. Balaji, «Experimental investigations on thermal performance enhancement and effect of orientation on porous matrix filled PCM based heat sink,» International Communications in Heat and Mass Transfer, vol. 46, pp. 27-30, 2013.

[26] W. G. Alshaer, S. A. Nada, M. A. Rady, E. P. Del Barrio e A. Sommier, « Thermal management of electronic devices using carbon foam and PCM/nano-composite», International Journal of Thermal Science, vol. 89, pp. 79-86, 2015.

[27] A. Mallow, O. Abdelaziz, S. Graham, «Thermal charging performance of enhanced phase change material composites for thermal battery design», International Journal of Thermal Sciences, vol. 127, pp. 19-28, 2018.

[28] F. Tang, D. Su, Y. Tang, G. Fang, «Synthesis and thermal properties of fatty acid eutectics and diatomite composites as shape-stabilized phase change materials with enhanced thermal conductivity», Solar Energy Materials and Solar Cells, vol. 141, pp. 218-224, 2015.

[29] Y. B. Tao e Y.-L. He, «A review of phase change material and performance enhancement methodfor latent heat storage system», Renewable and Sustainable Energy Reviews, vol. 93, pp. 245-259, 2018.

[30] B. Praveen, S. Suresh, «Experimental study on heat transfer performance of neopentyl glycol/CuO composite solid-solid PCM in TES based heat sink», Engineering Science and Technology, an International Journal, vol. 21, pp. 1086-1094, 2018

[31] F. Bahiraei, A. Fartaj e G.-A. Nazri, «Experimental and numerical investigation on the performance of carbon-based nanoenhanced phase change materials for thermal management applications», Energy Conversion and Management, vol. 153, pp. 115-128, 2017.

[32] R. Al Shannaq e M. M. Farid, «Microencapsulation of phase change materials (PCMs) for thermal energy storage systems», in Advances in Thermal Energy Storage Systems, Woodhead Publishing Series in Energy, pp. 247-284, 2015.

[33] S. Krishan, J. Y. Murthy e S. V. Garimella, «Direct Simulation of Transport in Open-Cell Metal Foams», Journal of Heat Transfer, vol. 128, pp. 793-799, 2006.

[34] X. Hu, X Gong, «Pore-scale numerical simulation of the thermal performance for phase change material embedded in metal foam with cubic periodic cell structure», Applied Thermal Engineering, vol. 151, pp. 231-239, 2019.

ACKNOWLEDGEMENTS

It was a rough path, full of sacrifices and, honestly, very poor of satisfactions. Despite that, it is effectively the end and first of all I want to thank me for believing in me, I want to thank me for doing all this hard work, I want to thank me for never quitting.

Huge thanks to Professor Andrea Diani, he was my guide and he followed me all along this thesis, especially in the complicated moments. Thanks to Professor Luisa Rossetto, that allowed me to start this work very early. If I have the possibility to graduate in September is due to the given chance.

Thanks to Professor Anna Stoppato, for being always available, kind, and supportive, for the given chance to become a tutor. Thanks to Professor Angelo Zarrella, for being an inspiration, as a Professor and as a man. Thanks to Professor Andrea Lazzaretto and Professor Sergio Rech, for teaching me the deep meaning of coherence and objectivity.

Thanks to my family, having an engineer at home is never easy. Thanks to my grandmas, the proudest of my results. Thanks to my grandad Dario, he saw the bachelor's degree, now he is seeing the master from wherever he is, and I hope he is proud of me.

Thanks to the "Gang del Boscolo", you all are always inked on my skin and on my heart, I love you all and I am so thankful to have met you along the years. I am sure you will succeed no matter what. In particular thanks to Papo, the most incredible person I met in the last five years, I would like to have half of your strength and consistency. Thanks to Tommi and Romiz, for the nights in Bologna and for the strong bond created. Thanks to Denni, hard like a rock outside, but sweet and soft inside. Thanks to Benni e Borgi, the most loyal and supportive companions in these two years.

Thanks to Bebe and Menaz, my brothers from other mothers, no other words are needed.

Thanks to Steva, there are no words to describe the patience, the kindness, and the humbleness of this man, he saved my life many times, and I am so thankful to have him in my life.

Thanks to Alberto, the most sensible and mature person I know. Also, best driver.

Thanks to Simonetta, she knows better than anyone how it was, and she was always there for me, thanks for the laughs and the swearing.

Thanks to Ilenia, even if recently she is always full of things to do, she was present when the most I needed it, and I will never forget it.

Finally, thanks to Martina, Claudia, Daniela, Linda, Cordiz and Califfo.

Per aspera ad astra.